TÉCNICO LISBOA

The Flying Saucer Concept for Micro Aerial Vehicles: Computational Study

Miguel Malhó Lorga Gomes

Thesis to obtain the Master of Science Degree in

Aerospace Engineering

Supervisor: Prof. João Manuel Melo de Sousa

Examination Committee

Chairperson: Prof. Filipe Szolnoky Ramos Pinto Cunha
Supervisor: Prof. João Manuel Melo de Sousa
Member of the Committee: Prof. Luís Rego da Cunha de Eça

July 2021

Dedicated to all those who placed the stepping stones on which I tread.

Declaration

I declare that this document is an original work of my own authorship and that it fulfills all the requirements of the Code of Conduct and Good Practices of the Universidade de Lisboa.

Acknowledgments

A debt of gratitude is owed to my family, which always pushed me forward and helped me take the right path throughout my entire life.

I would like to thank Prof. João Manuel Melo de Sousa for his undying support. His expertise, readiness to indulge in discussion and disposition to overcome any barrier in our way was what made this work possible.

Last but not least, many thanks to my friends, who offered me companionship, comfort and joy during these times.

Resumo

Esta dissertação apresenta um estudo CFD sobre um disco rotativo em voo a ângulos de ataque 0°, 5° e 10°, procurando investigar a potencial aplicação desta geometria em MAVs. O software comercial FLUENT foi utilizado em simulações com IDDES. A geometria do disco é circular e infinitamente fina, pois não possui espessura. O número de Reynolds baseado no escoamento não perturbado e no diâmetro do disco foi fixado em 150,000. O $AdvR$ varia entre 0 e 8, no qual $AdvR$ é o quociente entre a velocidade da extremidade do disco devido a rotação e do escoamento.

Para incidência nula, os momentos de rolamento e picada, medidos numa superfície do disco, sofrem uma mudança de sinal entre $AdvR$ = 1 e 2, e 2 e 4, respetivamente. Um comportamento periódico foi observado para $AdvR$ = 2, bem como uma linha de separação, que se movimenta para montante com aumento de rotação. A α = 5°, C_L permanece aproximadamente constante até $AdvR$ = 2, pois uma bolha de separação está presente na superfície superior e magnitudes de rotação são baixas. A supressão da bolha e regiões intensas de baixa pressão, causadas pela rotação, ocorrem a $AdvR$ = 4 e 8, levando a um aumento de C_L. O L/D diminui com rotação. Rotação diferencial (8,0) leva a um aumento de C_L enquanto que o caso (8,-8) reduz o momento de rolamento. Os resultados para α = 10° mostram que a rotação diferencial (8,0) elimina também a bolha de separação e aumenta a sustentação.

Palavras-chave: Disco Rotativo; Aerodinâmica; Micro-veículo Áereo; Mecânica dos Fluidos Computacional; IDDES.

Abstract

This dissertation presents a CFD study regarding a rotating disc in flight at angles of attack 0°, 5° and 10°, seeking to investigate the potential application of such geometry in MAVs. The commercial software FLUENT was used for the simulations with IDDES. The disc geometry is circular and infinitely thin, since it has no thickness. The free stream Reynolds number was fixed at 150,000, based on the disc's diameter. The $AdvR$ was varied between 0 and 8, where $AdvR$ is the ratio between disc edge speed due to rotation and flow speed.

For zero incidence, rolling and pitching moments, measured for one surface of the disc, undergo a change of signals from $AdvR$ = 1 to 2, and 2 to 4, respectively. Periodic behaviour was obtained for $AdvR$ = 2, as was a salient separation line, which moves upstream with increasing rotation. At α = 5°, C_L remains roughly constant until $AdvR$ = 2, since a laminar separation bubble is present on the top surface and rotation magnitudes are low. Suppression of the bubble and intense low pressure regions, caused by rotation, occur at $AdvR$ = 4 and 8 and both lead to an increase in lift production. The L/D diminished with rotation. Differential rotation $AdvR$ = (8,0) leads to an increase in C_L, while case (8,-8) decreases rolling moment. The results for α = 10° show that differential rotation (8,0) still suppresses the separation bubble and leads to an increase in lift.

Keywords: Rotating Disc; Aerodynamics; Micro Aerial Vehicle; Computational Fluid Dynamics; IDDES.

Contents

List of Tables

List of Figures

Nomenclature

Acronyms

CFD Computational Fluid Dynamics

COM Center of Mass

COP Center of Pressure

DES Detached Eddy Simulation

DNS Direct Numerical Simulation

IDDES Improved Delayed Detached Eddy Simulation

LAR Low Aspect Ratio

LES Large Eddy Simulation

LSB Laminar Separation Bubble

MAV Micro Aerial Vehicle

NSE Navier-Stokes Equations

QUICK Quadratic Upwind Interpolation for Convective Kinetics

RANS Reynolds-averaged Navier-Stokes

RMSD Root Mean Square Deviation

SIMPLE Semi-Implicit Method for Pressure Linked Equations

SST Shear-Stress Transport

UAV Unmanned Aerial Vehicle

UFO Unidentified Flying Object

VTOL Vertical Take-off and Landing

Greek Symbols

α Angle of attack [$\circ$]

δ Boundary layer thickness [m]

ν Kinematic viscosity [m^2/s]

Ω Angular velocity [rad/s]

ω Vorticity [$1/s$]

ψ Precession [$\circ$]

ρ Density [kg/m^3]

τ_w Wall shear stress [Pa]

ξ Characteristic length

Roman Symbols

$AdvR$ Advance Ratio

AR Aspect Ratio

C_D Drag coefficient

C_f Skin friction coefficient

C_L Lift coefficient

C_M Moment coefficient

C_p Pressure coefficient

D_d Disc diameter [m]

F Non-dimensional radial velocity component

f Frequency [Hz]

G Non-dimensional tangential velocity component

H Non-dimensional axial velocity component

I Moment of inertia

k Turbulence kinetic energy [m^2/s^2]

L Angular momentum [$kg\ m^2/s$]

L/D Lift to Drag Ratio

p Pressure [Pa]

R_d Disc radius [m]

Re Free stream Reynolds number

Re_Ω Rotational Reynolds number

Re_{edge} Rotational Reynolds number on the edge of the disc

S_t Strouhal number

t Time [s]

t_c Time step size [s]

U Velocity [m/s]

w Specific dissipation rate [$1/s$]

X,Y,Z Cartesian coordinate axes

Superscripts

‘ Adimensional

Subscripts

∞ Free stream condition

i, j, k Computational indexes

r, θ, z Cylindrical components

w, e Cell face indexes

WW, W, P, E, EE Cell indexes

x, y, z Cartesian components

Chapter 1

Introduction

1.1 Motivation

The Second World War brought forth an immense interest in aviation as military aircraft played a crucial role in just about any battle throughout this global conflict. Naturally, every parameter and possible shape of fighter jets was scrutinized and profoundly investigated, so that an edge over the opposing force could be gained. One experimental design that emerged amidst this research was that of an airplane with circular planform wing, which theoretically was more resistant and allowed for easier take-off and landing, when compared to a conventional wing design. Both German and American forces toyed with this concept, producing the Sack AS-6 V1 and the Vought V-173 (Figure 1.1), respectively.

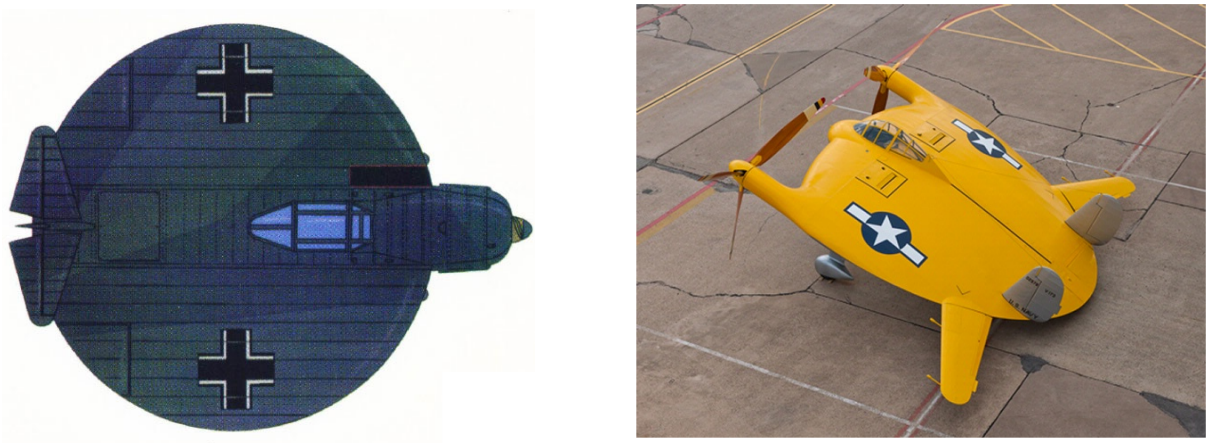

Figure 1.1: Sack AS-6 V1 [1] (left) and Vought V-173 [2] (right).

While the Sack AS-6 V1 was plagued by technical problems, the American made ”Flying Pancake” showed great promise, effectively proving that such designs are indeed worth looking into [2].

Some time later, during the second half of the twentieth century, the UFO (Unidentified Flying Object) craze that took the world by storm and the increasing popularity of the science-fiction genre further propelled the interest in circular-winged vehicles, or the so-called ”Flying Saucers”. The main idea then was to design such a disc-shaped aircraft, with VTOL capabilities and able to cruise at high velocities.

Several endeavours to design such vehicles in a functional yet efficient manner produced a colourful set of concepts. The Avro Canada VZ-9 Avrocar (Figure 1.2) stands tall as perhaps the most recognizable and the most practical, since it successfully hovered nearly 1 meter above ground, laying the foundations for future VTOL technologies.

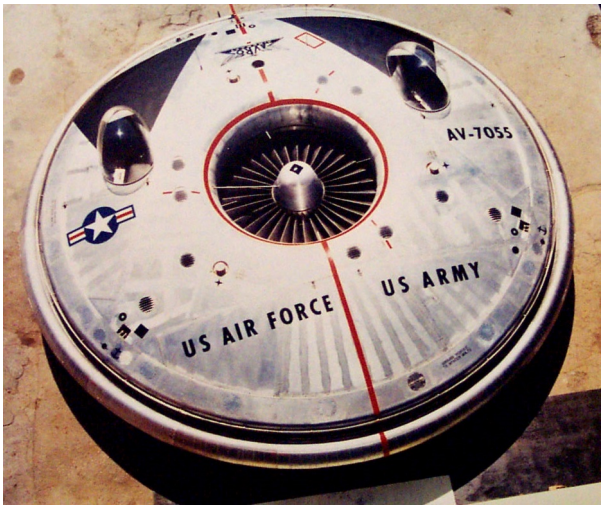

Figure 1.2: Avro Canada VZ-9 Avrocar [3].

However, since it was inherently unstable and proved much too hard to control, the project was cancelled in 1961 [4].

Recently, Unmanned Aerial Vehicles (UAVs) have been the primary focus of several military branches. The ability to use highly controllable vehicles to deploy and pick-up troops, perform surveillance and reconnaissance, and engage in confrontations all without endangering human life is certainly appealing. Disc-shape drones seem perfectly apt to perform these tasks, since they are highly maneuverable and fairly stealthy: the circular shape scatters potential radar waves in many directions, making it harder to detect.

Two exciting UAVs that have a circular shape are the Sikorsky Cypher, created in 1988, and the ADIFO in 2019. Both can be seen in Figure 1.3.

Figure 1.3: Sikorsky Cypher [5] (left) and ADIFO [6] (right).

The former was capable of carrying loads up to 23 kilograms and performing a multitude of tactical operations [7]. The much more recent ADIFO is reported to achieve a smooth transition between subsonic and supersonic regimes, boasts a high L/D ratio and spectacular maneuverability [8].

The Micro Aerial Vehicles (MAVs) are a subclass of UAVs. As the name implies, MAVs are distinguished by their small size, allowing for added stealth and versatility. Precise figures vary, but MAVs do not generally exceed 1 meter in wingspan and weigh more than 0.5 kilograms. Interest in such vehicles has grown immensely, due not only to their low production cost, but also to the wide range of complicated missions that these futuristic drones could theoretically perform: detection of radioactivity and chemical compounds, search for survivors, improved communications in both urban and military scenarios, and infiltration in confined, closely guarded areas [9, 10]. MAVs are meant to be carried by hand, therefore highly practical, and easily, if not immediately, deployed and controlled.

Generally, fixed-wing MAVs operate at $Re <$ 200,000 [11]. At such low Re, laminar separation bubbles are expected to make an appearance and negatively influence aerodynamic performance. Also, due to size restrictions, Low Aspect Ratio (LAR) lifting surfaces are utilized in fixed-wing MAVs. As such, a small, saucer-shaped drone, relying purely on a rotating surface for both lift and stability seems ideal for this class of vehicles, since not only fragile rotors and complicated moving parts are absent, but also because rotation might be able to control and suppress separation bubbles.

As of yet, the resulting flow structures and aerodynamic performance at such viscous Reynolds numbers around a small, spinning surface are still largely unknown. Not to mention that the effects that high degrees of rotation impart on the flow at various angles of attack are also mainly unreported on a spinning disc-wing.

1.2 Topic Overview

Several CFD simulations were performed on a rotating disc with zero thickness as to better ascertain the effect of rotation on aerodynamic performance and stability. Several degrees of rotation were tested and the corresponding flow structures, pressure mapping and aerodynamic parameters duly compared.

1.3 Objectives

This thesis was envisioned with three main goals in mind:

- Test the viability of a flying, rotating disc design as a possible MAV application;
- Better understand the complicated interaction between disc rotation and incoming flow at low angles of attack;
- Investigate the effects that high magnitudes of disc rotation have on aerodynamic performance.

1.4 Thesis Outline

This thesis begins by introducing the motivation and main objectives of this work on chapter 1.

Chapter 2 presents the nomenclature and physics governing the flight of a rotating disc. Aerodynamic forces and gyroscopic precession are briefly explained. The chapter ends with an overview of previous studies regarding disc wings, with and without rotation.

Chapter 3 introduces the von Kármán problem and its similarity solution. It was then simulated through CFD, as to assess the choice of mesh resolution and discretization schemes to handle rotational flow problems.

Chapter 4 sets up the parameters and definitions of the main problem.

Chapters 5, 6 and 7 showcase the results for angles of attack 0°, 5° and 10°, respectively. Results regarding turbulence kinetic energy distributions, vortical structures, aerodynamic data, limiting streamlines and differential rotation cases were all displayed and analyzed.

Finally, chapter 8 contains the conclusion and future work ideas, finalizing the thesis.

Chapter 2

Physics of a Flying Disc

2.1 Description

A flying disc can be regarded as wing with low AR, producing considerable lift at low angle of attack. For a typical wing, AR is defined by the following formula:

$$AR = \frac{(Wing\ Span)^2}{Wing\ Area}, \tag{2.1}$$

which, for a circular disc with radius R_d and diameter D_d, results in:

$$AR = \frac{D_d^2}{(D_d/2)^2\pi} = \frac{4}{\pi} \approx 1.273.$$

There are two key parameters governing the flight of a rotating disc: the lift force, and the spin of the disc, which has a stabilizing effect. Both are vital but it is only the inherent interplay between the two that allows the disc to stay airborne, as a disc without rotation would immediately topple over, and one without lift would not even get off the ground. What is so remarkable about this simple configuration is that one rotating surface can provide both lift and flight stability, thus avoiding the need for extra control surfaces.

2.1.1 Disc Nomenclature

For sign convention, the axes of the disc and respective rolling, yawing and pitching moments (R, S and P) around the body are defined in Figure 2.1. The variable Ω represents the angular velocity of the disc. Positive rotation implies anti-clockwise motion.

The center of mass (COM) is the point at which the force of gravity acts on the body, and the center of pressure (COP) where the aerodynamic forces take action. As Figure 2.1 illustrates, the COP is usually ahead of the COM, for typical disc flight.

Other important terms are the leading edge and trailing edge of the disc. These definitions are analogous to those of an airfoil, with the former referring to the front edge of the disc, that is, the part that comes into direct contact with the incoming flow, and the latter is the rear side. Once again regarding Figure 2.1, the leading edge is present at negative values of X, while the trailing edge at positive values. Since the disc is rotating, it is useful to distinguish retreating and advancing side. The former refers to the side of the disc at which rotational speed and free stream velocity have the same sign and add up. This occurs at positive Z values in Figure 2.1. On the other hand, the latter is where these two velocities oppose each other, happening at negative Z values. The variable $AdvR$ is the ratio of edge speed to flow speed. If $AdvR$ = 0, the disc is not rotating, and for $AdvR$ = 1, the edges of the disc are moving at the same speed as the free flow. Its formula is:

$$AdvR = \frac{\Omega R_d}{U_\infty}, \tag{2.2}$$

where U_∞ is the free stream velocity.

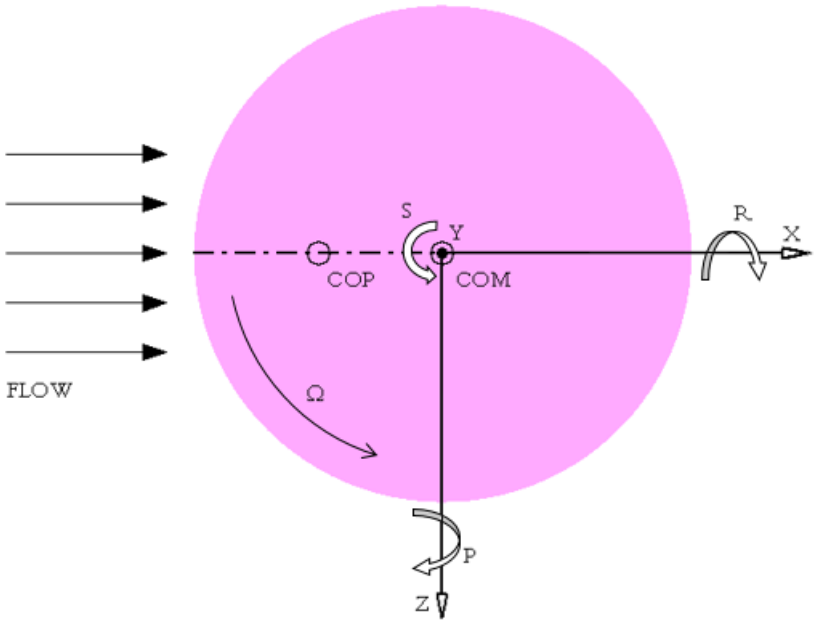

Figure 2.1: Orientation of the disc and sign convention.

2.1.2 Aerodynamics

Two of the most important aerodynamic contributions are the lift and drag forces. Simply put, lift force is generated due to the shape of the disc, which promotes a pressure difference between the upper and lower surface of the disc. This generates a force perpendicular to the incoming flow, which increases with α, until a certain critical angle is reached. From then on, lift descends abruptly. This is the pillar of all flight. Drag on the other hand, acts parallel to the flow but opposes it.

These forces act on the COP, causing the disc to experience moments around its center of mass. And since the COP regularly changes in flight, the prediction of these moments and their directions becomes increasingly difficult. The coefficients of lift, drag and moment are calculated by:

$$C_L = \frac{F_L}{\frac{1}{2}\rho A U_\infty^2}, \tag{2.3}$$

$$C_D = \frac{F_D}{\frac{1}{2}\rho A U_\infty^2}, \tag{2.4}$$

$$C_M = \frac{M}{\frac{1}{2}\rho A U_\infty^2 L}, \tag{2.5}$$

where F_L, F_D, M, ρ, A, and L are the lift force, drag force, moment, free stream density, surface area of the disc (πR_d^2) and reference length (D_d), respectively. A typical force scheme is shown in Figure 2.2.

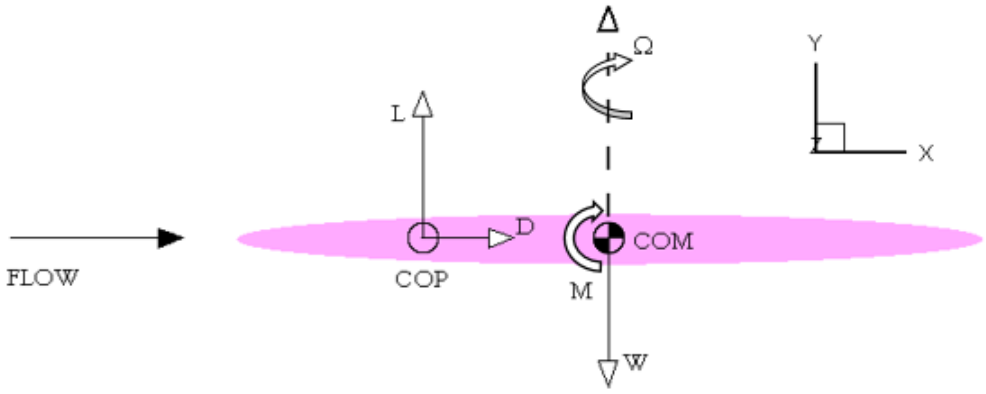

Figure 2.2: Forces acting on a flying rotating disc.

The resulting lift acts on the front of the disc, ahead of the center of mass. This causes an acute, unstable pitching moment, leading to a radical nose-up motion. This is where rotation comes into play.

2.1.3 Gyroscopic Precession

Firstly, a few definitions are in order. The angular momentum $\overrightarrow{L}$ is a rotational property, representing the rotational equivalent of linear momentum. For a rigid body, it is calculated by the Formula 2.6:

$$\overrightarrow{L} = I\overrightarrow{\Omega}, \tag{2.6}$$

where I is the moment of inertia. Angular momentum has the same direction as the spin rate. Obeying conservation laws, the angular momentum remains constant when there are no torques present. For the case of the flying disc, it was shown that aerodynamic moments act upon it, which cause a rate of change in $\overrightarrow{L}$, equal to the sum of all moments.

$$\frac{d\vec{L}}{dt} = \vec{M}. \tag{2.7}$$

Referring to Figure 2.2, the lift produces a negative, nose-up pitching moment around the COM. This moment is perpendicular to the angular momentum, causing it to preserve its magnitude, but not its direction. This change of direction is named precession ($\vec{\psi}$). Equation 2.7 can now be rewritten.

$$\frac{d\vec{\psi}}{dt} L = \vec{M}. \tag{2.8}$$

Simply put, the axis of rotation will move towards the direction of the torque. Therefore, the unstable pitching moment is now translated into a rolling moment. That is gyroscopic precession. While the immediate pitch instability is avoided, the disc swerves to left or to right, depending on which direction the disc is spinning. Also interesting to note is that the rate of precession can be lowered by increasing the spin rate. The faster the disc spins, the less susceptible it is to precession, becoming more stable. One might be tempted to fully eliminate this phenomenon, but while plenty of precession is detrimental, a small amount is indispensable for flight. The unstable pitching moment must be transformed into a rolling moment for the disc to attain altitude. This is of course a simplification, as the moments will seldom act exactly on a defined axis, thus also causing rolling motion. Nonetheless, they will usually act perpendicular to the direction of rotation, making the situation described above representative of the overall stability granted by disc rotation.

2.1.4 Robins-Magnus Effect

Rotation causes yet another well-known effect. Since the advancing and retreating side experience lower and higher relative speed, respectively, a velocity gradient will be created across the disc surface. This generates a pressure difference, according to Bernoulli, resulting in a force perpendicular to the flow and on the same plane as the disc. This is the Robins-Magnus effect, represented in Figure 2.3. Consequently, roll is induced.

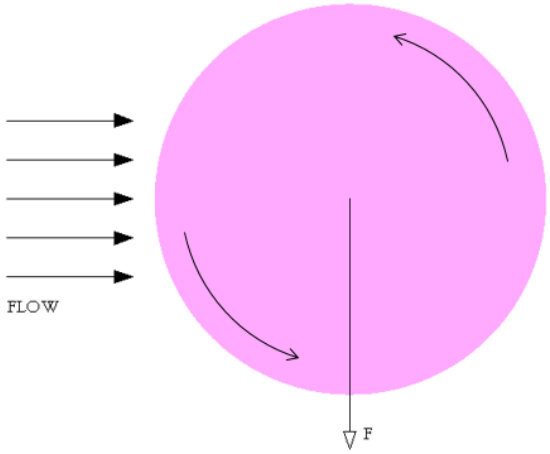

Figure 2.3: Robins-Magnus effect visualized.

2.2 Flow Separation

2.2.1 Laminar Separation Bubble

As was previously stated, fixed-wing MAVs fly at $Re < 200{,}000$. At this low Reynolds number, a phenomenon known as laminar separation bubble (LSB) is bound to appear.

Lacking the momentum transfer due to turbulent mixing, the laminar boundary layer is highly susceptible to separation under adverse pressure gradients. When the boundary layer does separate from the surface, the flow reattachs itself downstream, encompassing a region of recirculating motion, as well as transitional and turbulent flow. This typically happens near the leading edge for all aircraft models flying at low Reynolds. The aerodynamic performance is severely worsened, since drag increases and stability is reduced.

A typical profile of a LSB is represented in Figure 2.4.

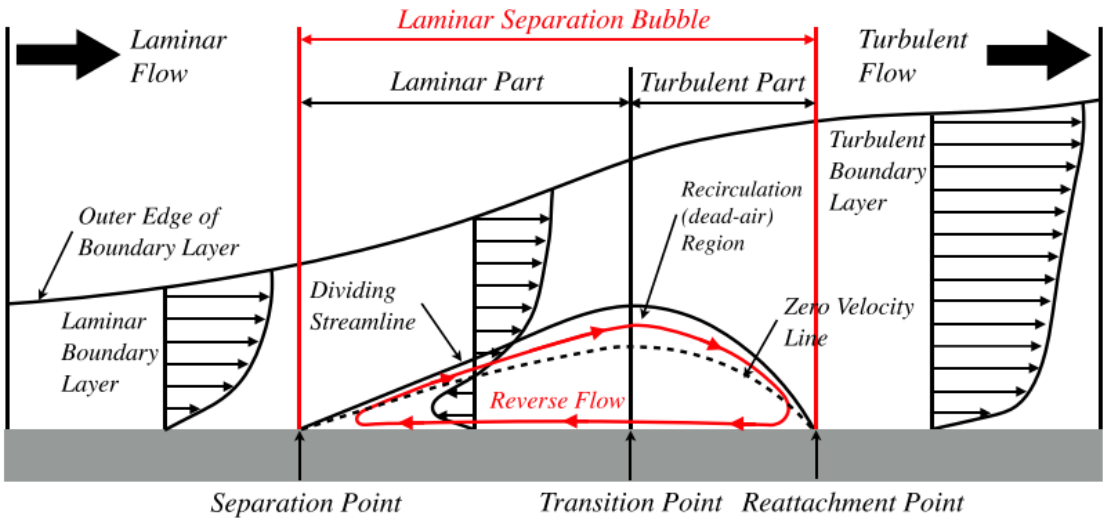

Figure 2.4: Description of a laminar separation bubble from Lee et al. [12].

When the laminar boundary layer encounters an adverse pressure gradient strong enough to cause separation, it abandons the surface and forms a laminar and highly unstable free shear layer. Transition soon ensues and, due to the high mixing and momentum transport, characteristic of the turbulent state, the flow normally manages to reattach itself to the surface, in a process known as reattachment. Downstream of this reattachment point exists a fully turbulent boundary layer.

A zone with recirculating flow, constituting the so called LSB, is evident between the separation and the reattachment point, near the surface, having both a laminar and turbulent part. On the laminar part, just after separation and before transition, a plateau of pressure is created. On the turbulent part however, the pressure rapidly recovers, as seen in Figure 2.5.

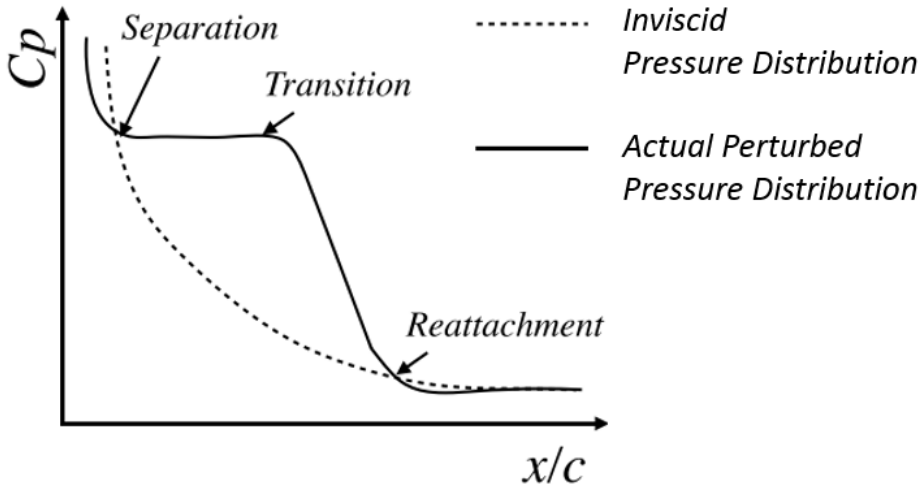

Figure 2.5: The C_p distribution across a typical LSB on an unspecified airfoil from Roberts [13].

The size and shape of the bubble vary greatly and it can be classified as either a short or long bubble. A short bubble typically occurs at high Reynolds numbers and has a small effect on the pressure distribution, barely impacting the flow outside of the bubble. Its size is roughly 1% chord and its biggest impact is inducing transition. On the other hand, a long bubble interacts vividly with the exterior flow, gravely influencing the pressure profile and thus the aerodynamic performance. A long bubble usually covers most of the airfoil's surface [13, 14].

The two key parameters that govern the bubble's physical shape and behaviour on a typical airfoil are Reynolds number Re and angle of attack α.

With a decrease in Reynolds number, the laminar shear layer becomes dominant and long. So long in fact, that the short bubble is only capable of reattaching itself progressively downstream, bursting into a long bubble. With even lower values of Re, the bubble has attained such a length over the surface that it is unable to reattach itself, which translates to complete separation. Regarding α, the separation point moves upstream with increasing angles of incidence, as the adverse pressure gradient becomes more intense. This causes a reduction in bubble size, as transition and reattachment occur progressively close to separation, thus contracting. For very high angles of incidence, near stall, the bubble bursts, leading to a drastic loss of aerodynamic performance [13, 14].

2.2.2 3D Flow Separation

In two-dimensional flows, boundary layer separation is identified when the value of the skin friction coefficient C_f is zero. That translates to:

$$C_f = \frac{\tau_w}{\frac{1}{2}\rho U_\infty^2} = 0, \tag{2.9}$$

where τ_w is the local wall shear stress.

For three dimensional flows however, this simple criterion can no longer be utilized, since the flow structures are much more complex and $C_f = 0$ is seldom associated with separation [14]. A typical 3D flow separation is not synonymous with flow reversal, as in two dimensional cases, since here separation translates to the flow leaving the near surface when confronted with adverse conditions.

The indicator of separation for 3D concerns the behaviour of limiting streamlines. These are defined as streamlines when the distance normal to the surface tends to zero, and are coincident with the skin friction lines, that are streamlines derived from the vector field of wall shear stress. Maskell [15] postulates that separation occurs when two distinct limiting streamlines converge onto a particular limiting streamline. This is a necessary condition. Additionally, when approaching a separation line, τ_w drops to a minimum. On the other hand, if limiting streamlines are seen diverging from a particular line, then a reattachment process is identified, where the flow dives towards the surface and attaches.

Tobak and Peake [16] explained succinctly this criterion.

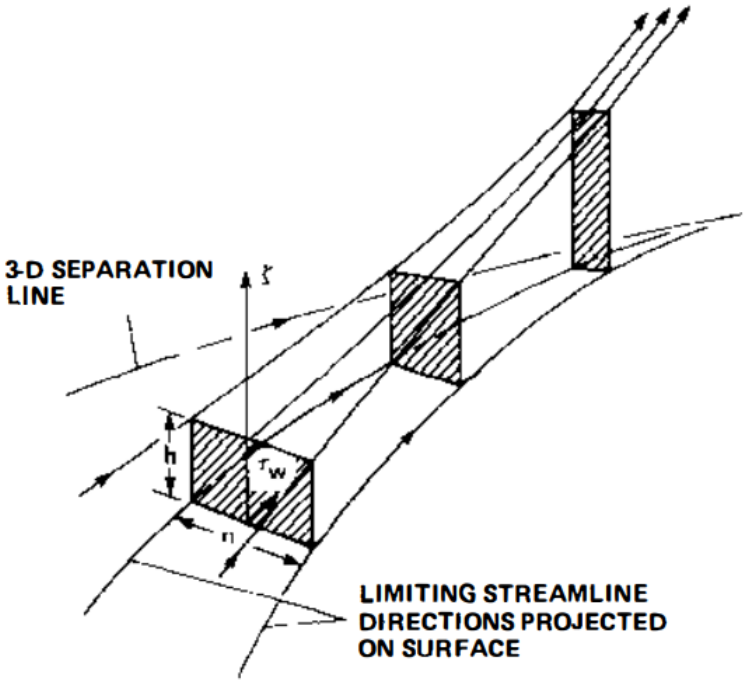

Figure 2.6: Scheme of limiting streamlines from Tobak and Peake [16].

With reference to Figure 2.6, n is the distance between two limiting streamlines and h the height of a rectangular streamtube. Taking a mass flux balance across this rectangular area hn, and after some substitutions and algebra, results in:

$$h = C \left(\frac{\nu}{n\tau_w} \right)^{\frac{1}{2}}. \tag{2.10}$$

The height h of the streamlines increases as n or τ_w decreases, or when the separation line is approached. Meaning that in the vicinity of a separation line, limiting streamlines must leave the surface. The opposite is true for reattachment lines.

This criterion will be utilized to evaluate possible separations and reattachments.

2.3 Literature Review

The disc-wing geometry has been the focus of much fewer studies than the conventional wing. Especially so, for rotating discs. As such, the intricacies of a flying disc rotating at high $AdvR$ are as of yet largely unknown. This next section is divided into results obtained through experimental measurements and computational simulations. In turn, each is further divided on whether the tested geometry rotated ($AdvR \neq 0$) or not ($AdvR = 0$).

2.3.1 Experimental Studies

Numerous wind-tunnel tests have been conducted on a still and rotating disc. Through these techniques, direct observations can be made and physical phenomenons accurately reported.

$AdvR = 0$

Torres and Mueller [17], [18] laid the foundation of aerodynamic studies of LAR wings (one much like the focus geometry of this work) at the typical MAV operational range (Re from 50,000 to 140,000). The main characteristic of these types of wings is that the tip vortices might be present over most of area of the wing, thus drastically altering their aerodynamic behaviour, such as energizing the flow and delaying separation bubbles, thus generating more lift than a standard wing. In fact, it was found that as the AR of the wing diminishes, the C_L curves become progressively non-linear, and the stall angle increases.

Kamaruddin [19] extensively studied the impact that different configurations of flying discs have on aerodynamic performance at Re = 378,000. Several parameters, such as camber shape, thickness-to-diameter ratio, cavity and edge geometry were altered and their effects on L/D ratio, pitching moment coefficient and flight trajectory duly compared.

$AdvR \neq 0$

Firstly, Nakamura and Fukamachi [20] visualized the effects that a disc with and without rotation had on a planar flow field, with eventual $AdvR$ of roughly 2.26 at Re = 16,000. From the disc at rest, a pair of longitudinal vortices was noticed, which produced added lift, when compared to the case without rotation. These structures were enhanced by rotation, which induced considerate downwash downstream of the disc. Flow asymmetry was also noted.

Most notably Potts and Crowther [21] tested a restrict range of Advance Ratios (between 0 and 1.04) at free stream Reynols numbers between 113,000 to 378,000. It was seen that, for pre-stall conditions, rotation has little effect on aerodynamic loads. Lift and drag curves were unchanged, but pitching and rolling moments differ only slightly for the highest values of $AdvR$. The evolution of the aerodynamic coefficients can be seen in Figure 2.7. It was also remarked that, with increasing α, several changes happen on the upper surface of the disc, like the separation line present on the front travels further upstream, the one present on the trailing edge moves towards the center and the detachment point of the trailing vortices migrates to the sides.

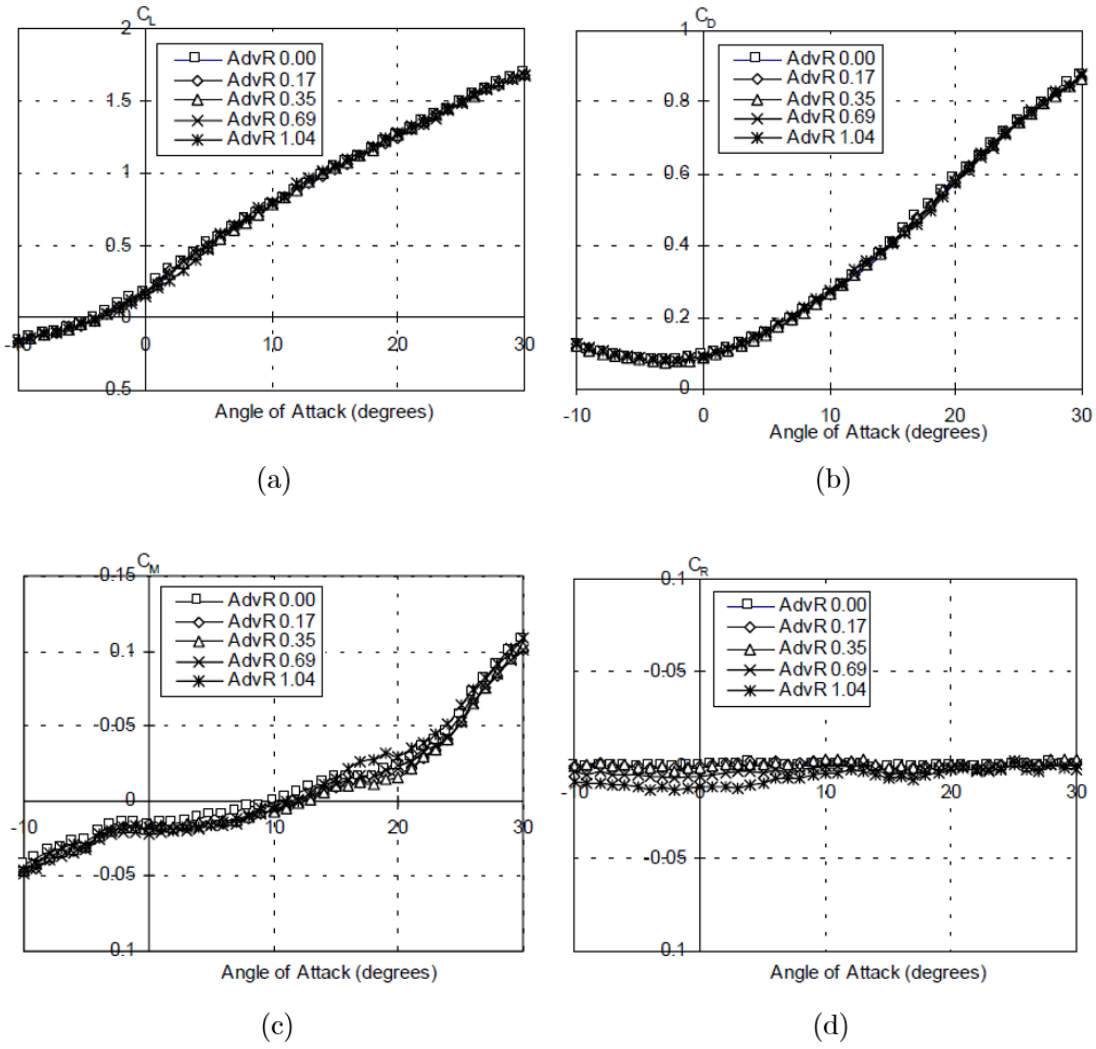

Figure 2.7: Evolution of (a) C_L, (b) C_D, (c) C_M $pitch$ and (d) C_M $roll$ with $AdvR$ at Re = 378,000 from Potts and Crowther [21].

Some time after, the same authors remarked through smoke-wire flow visualization that the main shape of the separation bubble on top of the disc is mainly unaffected by rotation, even though it slightly shifts to the advancing side [22], as in Figure 2.8 (advancing side on the left).

A similar study regarding the effects of disc rotation on a cambered disc was conducted by Higuchi et al. [23]. They remarked through flow visualization of a rotating disc at Re = 110,000 that added rotation of the disc $AdvR$ = 0.8 at high α (15° to 30°) causes the separation bubble protruding from the leading edge to slightly increase in size, but it has little to no effect on the trailing vortices. At low α (0° to 5°) however, the rotation helps to suppress separation at the trailing edge, by promoting transition. Also, delayed and accelerated separation is seen to occur at the retreating and advancing side, respectively.

Seo et al. [24] obtained lift, drag and pitching moment coefficients for a spinning and non-spinning commercially available discus. Oil and smoke visualizations of $AdvR$ = 0 and 0.2 were also conducted. When rotation was added, a pair of longitudinal vortices appear, rather similar to wing-tip vortices, and would delay separation on the top surface of the disc.

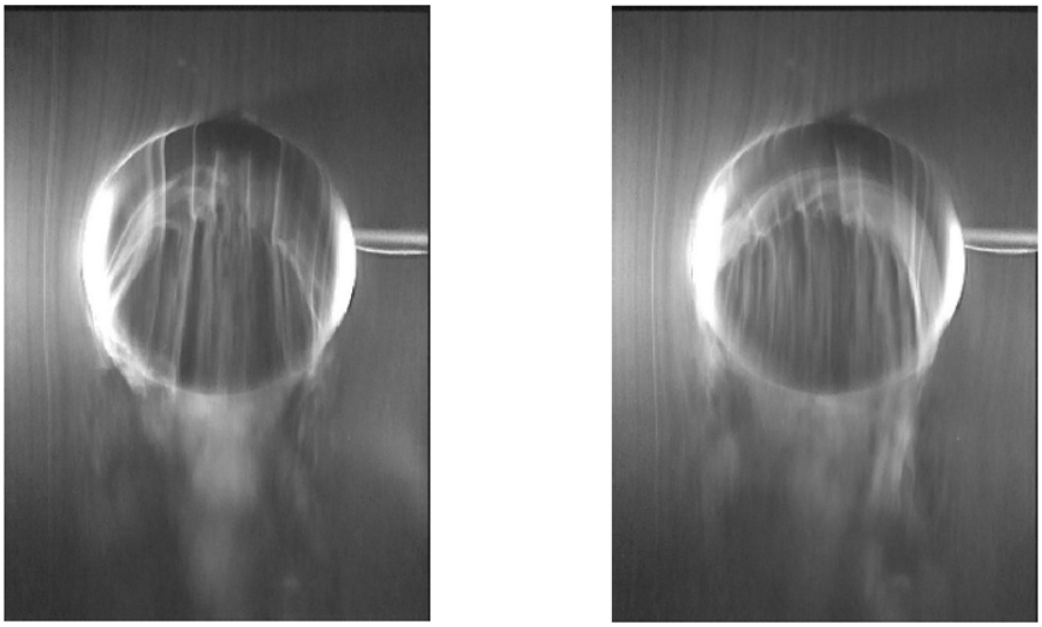

(a) (b)

Figure 2.8: Flow visualization on the upper surface of the disc at α = 0° for $AdvR$ = (a) 0 and (b) 0.9, taken from Potts and Crowther [22].

2.3.2 Computational Studies

Despite not being able to replace wind-tunnel experiments, Computational Fluid Dynamics (CFD) has proven to be an effective tool to obtain information about flow variables and structures of interest, mainly because it circumvents the need to build and accurately recreate the intended problem in experimental conditions.

$AdvR = 0$

An optimization study by means of a genetic algorithm was carried out by Seo et al. [25], with the purpose of finding the ideal launch conditions and geometry of a disc. The longest flight distance was achieved by maximizing the yaw rate.

Lukes et al. [26] analysed the flow around a non-rotating Floater disc at a wide range of α (0° to 15°) at Re = 375,000, employing several turbulence models, in order to find the most reliable for this type of flow situation. He accurately replicated wind-tunnel measurements, mainly the separation downstream of the leading edge, through the turbulent standard $k-\epsilon$ model, which he hailed as the most appropriate model for this problem.

Potts and Masters [27] obtained an excellent agreement between available experimental data and computational values, using the $k-\omega$ SST turbulence model, when dealing with a wide range of non-rotating disc geometries at low α. At high angles of attack however, the CFD had trouble identifying the problematic stall regime.

A wide range of high angles of incidence (30° to 90°) was then tested by Tian et al. [28] over a disc using DNS at Re = 500, which sought to analyze the inherent unsteady phenomenons. He started by directing the flow perpendicular to the disc (90°) and progressively decreasing the angle of attack. Four types of flow patterns were identified: chaotic pattern, quasi-periodic pattern, periodic pattern associated with a low frequency modulation and periodic pattern, which means that a periodic pattern emerges behind the disc with diminished angle of incidence. Here, periodic pattern translates to the vortex shedding ceasing to be random, but determined. This change happened around 55° of angle incidence. This shedding however was not aligned with the stream-wise direction.

A year later Gao et al. [29], broaden the study to a wider range of α (20° to 90°) and the following range for Re: (50 to 300). A fifth pattern, the steady state was identified and the consequent thresholds between all five regimes were mapped out in a Reynolds vs α graph. Furthermore, each regime was exhaustively described and characterised.

$AdvR \neq 0$

A CFD study was conducted by Rohde [30] on an ellipsoid with $AdvR$ ranging from 0 to 1.5 at Mach number 0.5. The flow was deemed compressible to accelerate the convergence process, on the basis that the low Mach number of the simulations would have a minimal impact on boundary layer growth and aerodynamic coefficients. The angle of attack was fixed at 5°. It was discovered that without rotation, a separation line appears at the top surface of the disc at roughly 70% chord and on the lower surface, a much smaller separation region is present. When $AdvR$ = 1 was applied, this last region completely disappears, while on the top surface, the separation line wrapps around the left receding edge. It was also discovered that rotation has a minimal effect on surface pressure distribution. He further confirmed the results obtained from Potts and Crowther [21], by observing that rotation does not affect lift and drag values, and that the rolling moment increases with rotation.

Wiesche [31] performed LES calculations on a rotating disc in an air crossflow at Re = 13,700, in order to observe the heat transfer and wake changes that are brought by the spinning. With an $AdvR$ of 2, a periodic vortex shedding was reported and when the $AdvR$ was increased to 10, a fully turbulent wake was evident. Later, the same author analysed the consequent wakes of $AdvR$ = 0, 1, 2.5 and 12.5 at Re = 8,000, and remarked that a turbulent wake was generated starting from $AdvR$ = 2.5 [32].

A study of a flying coin-shaped disc was conducted by Khalid Moukhtar [33], in order to document the aerodynamic parameters and overall behaviour of the flow. The tested range of $AdvR$ was between 0 and 1. It was seen that only the rolling moment coefficient was affected by the spin of the disc, mainly due to the Magnus force, and the results from Rohde [30] were corroborated.

With the intent to understand how the stabilizing effect of rotation on a disc would impact its throwing distance, Rouboa et al. [34] regarded that rotation results in larger distances covered by the disc, with the vertical distance remaining unchanged.

In addition, Dumitrache et al. [35] performed studies at Re = 690,000 on both rotating and non-rotating discs, with URANS and SST $k - w$ as the turbulence model. The variable $AdvR$ assumed values of 0.3 and 0.5. The typical asymmetry on pressure contours and flow structures was observed.

Chapter 3

The von Kármán Problem

3.1 Description

The von Kármán swirling flow is merely composed by an infinitely long rotating planar disc immersed in still flow and, as simple as it may sound, rotation is the only factor that drives the flow. A thin boundary layer on the surface of the disc is created, due to the no-slip condition. The flow is pushed outwards, expected due to the centrifugal force, and drawn axially to satisfy mass conservation. To properly illustrate this flow problem, the typical velocity profiles are represented in Figure 3.1.

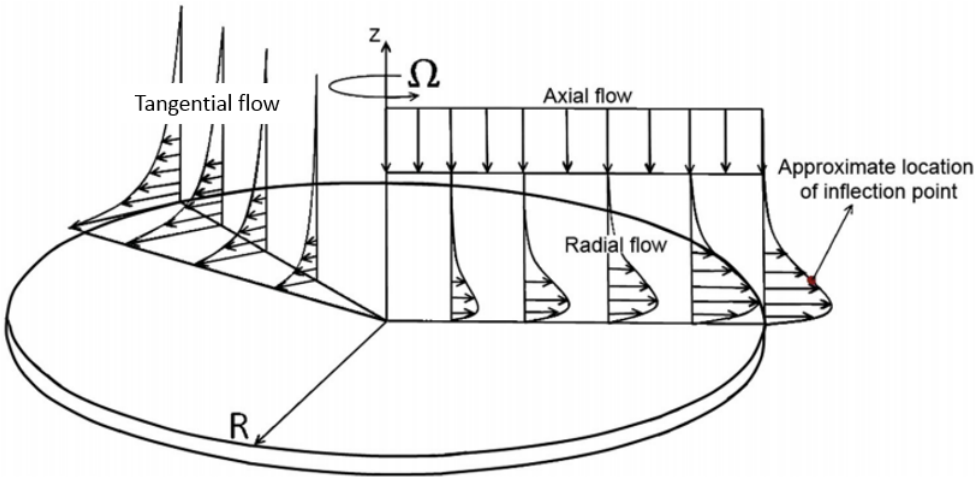

Figure 3.1: Visual representation of the velocity profiles from the rotating disc configuration from Özkan et al. [36].

As can be observed, the radial velocity profile possess an inflection point, which satisfies Rayleigh's inflection-point criterion. This means that the flow is inviscidly unstable, that is, it remains unstable at infinite Reynolds number. This inviscid instability is also referred to as a crossflow instability, which three-dimensional boundary layers, produced by the flow on a swept wing, habitually display. Due to this similarity, extensive investigation of the rotating disc flow problem undoubtedly leads to a deeper understanding of transition in 3D boundary layers and evolution of propagating instabilities.

The additional appeal of this problem stems from two key aspects: it is rather easy to replicate in experimental conditions and an exact similarity solution exists for laminar flow, derived by von Kármán in 1921. This is quite remarkable, since the complex set of Navier-Stokes equations are boiled down to a simple pair of ordinary differential equations, allowing the full description of the flow.

3.2 Governing Equations

The rotating disc is considered in a cylindrical coordinate system as an infinite planar surface, with constant rotation rate Ω, spinning about an axis perpendicular to the disc.

The steady continuity and Navier-Stokes equations (NSE) in cylindrical coordinates, for a incompressible fluid with constant viscosity are as follow, with r, θ and x as the radial, tangential and axial components, respectively.

Continuity Equation

$$\frac{1}{r}\frac{\partial}{\partial r}(rU_r) + \frac{1}{r}\frac{\partial U_\theta}{\partial \theta} + \frac{\partial U_x}{\partial x} = 0, \tag{3.1a}$$

Radial component of NSE

$$U_r\frac{\partial U_r}{\partial r} + \frac{U_\theta}{r}\frac{\partial U_r}{\partial \theta} - \frac{U_\theta^2}{r} + U_x\frac{\partial U_r}{\partial x} = -\frac{1}{\rho}\frac{\partial p}{\partial r} + \nu\left[\frac{\partial}{\partial r}\left(\frac{1}{r}\frac{\partial}{\partial r}(rU_r)\right) + \frac{1}{r^2}\frac{\partial^2 U_r}{\partial \theta^2} - \frac{2}{r^2}\frac{\partial U_\theta}{\partial \theta} + \frac{\partial^2 U_r}{\partial x^2}\right], \tag{3.1b}$$

Tangential component of NSE

$$U_r\frac{\partial U_\theta}{\partial r} + \frac{U_\theta}{r}\frac{\partial U_\theta}{\partial \theta} + \frac{U_r U_\theta}{r} + U_x\frac{\partial U_\theta}{\partial x} = -\frac{1}{\rho}\frac{1}{r}\frac{\partial p}{\partial \theta} + \nu\left[\frac{\partial}{\partial r}\left(\frac{1}{r}\frac{\partial}{\partial r}(rU_\theta)\right) + \frac{1}{r^2}\frac{\partial^2 U_\theta}{\partial \theta^2} + \frac{2}{r^2}\frac{\partial U_r}{\partial \theta} + \frac{\partial^2 U_\theta}{\partial x^2}\right], \tag{3.1c}$$

Axial component of NSE

$$U_r\frac{\partial U_x}{\partial r} + \frac{U_\theta}{r}\frac{\partial U_x}{\partial \theta} + U_x\frac{\partial U_x}{\partial x} = -\frac{1}{\rho}\frac{\partial p}{\partial x} + \nu\left[\frac{1}{r}\frac{\partial}{\partial r}\left(r\frac{\partial U_x}{\partial r}\right) + \frac{1}{r^2}\frac{\partial^2 U_x}{\partial \theta^2} + \frac{\partial^2 U_x}{\partial x^2}\right], \tag{3.1d}$$

where p, ρ and ν are the static pressure, density and kinematic viscosity, respectively.

This problem has axial symmetry ($\frac{\partial}{\partial \theta} = 0$) and since the gradients normal to the wall (axial direction) are much larger that those in the radial and tangential directions, the diffusive terms but the one normal to the surface can be neglected. Accordingly, Equations 3.1a - 3.1d boil down to:

$$\frac{\partial U_r}{\partial r} + \frac{U_r}{r} + \frac{\partial U_x}{\partial x} = 0, \tag{3.2a}$$

$$U_r\frac{\partial U_r}{\partial r} - \frac{U_\theta^2}{r} + U_x\frac{\partial U_r}{\partial x} = -\frac{1}{\rho}\frac{\partial p}{\partial r} + \nu\frac{\partial^2 U_r}{\partial x^2}, \tag{3.2b}$$

$$U_r \frac{\partial U_\theta}{\partial r} + \frac{U_\theta U_r}{r} + U_x \frac{\partial U_\theta}{\partial x} = \nu \frac{\partial^2 U_\theta}{\partial x^2}, \tag{3.2c}$$

$$U_r \frac{\partial U_x}{\partial r} + U_x \frac{\partial U_x}{\partial x} = -\frac{1}{\rho}\frac{\partial p}{\partial x} + \nu \left[\frac{1}{r}\frac{\partial}{\partial r}\left(r \frac{\partial U_x}{\partial r} \right) + \frac{\partial^2 U_x}{\partial x^2} \right]. \tag{3.2d}$$

To handle this problem on laminar regime, von Kármán introduced a characteristic length ξ and the following assumptions for the various velocities and pressure:

$$\xi = x \left(\frac{\Omega}{\nu} \right)^{\frac{1}{2}}, \tag{3.3}$$

$$U_r = \Omega r F(\xi), \qquad U_\theta = \Omega r G(\xi), \qquad U_x = (\Omega\nu)^{\frac{1}{2}} H(\xi), \qquad p = -\rho\Omega\nu P(\xi). \tag{3.4}$$

This exchange of variables enables the derivation of an exact similarity solution of the steady Navier-Stokes equations. The substitution of the definitions presented in 3.3 and 3.4 in the Equations 3.2a - 3.2d yields the following non linear ordinary differential equations, with $'$ symbolizing derivation:

$$H' = -2F, \tag{3.5a}$$

$$F'' = F^2 - G^2 + F'H, \tag{3.5b}$$

$$G'' = 2FG + G'H, \tag{3.5c}$$

$$P' = HH' - H''. \tag{3.5d}$$

Now, only a set of boundary conditions are needed to solve the system of equations. Considering the context of the problem, the following are easily deduced:

$$x = 0: \qquad U_r = 0; \quad U_\theta = \Omega r; \quad U_x = 0,$$

$$x \to \infty: \qquad U_r \to 0; \quad U_\theta \to 0.$$

which translate to:

$$x = 0: \qquad F = 0; \quad G = 1; \quad H = 0,$$

$$x \to \infty: \qquad F \to 0; \quad G \to 0,$$

This set of equations now becomes solvable. With the aid of $MATLAB$, the evolution of the variables F, G, H and $P - P(0)$ with regards to ξ was obtained and plotted in Figure 3.2. The obtained solution, achieved by solving the system of differential equations, serves as a comparison term for the upcoming CFD results.

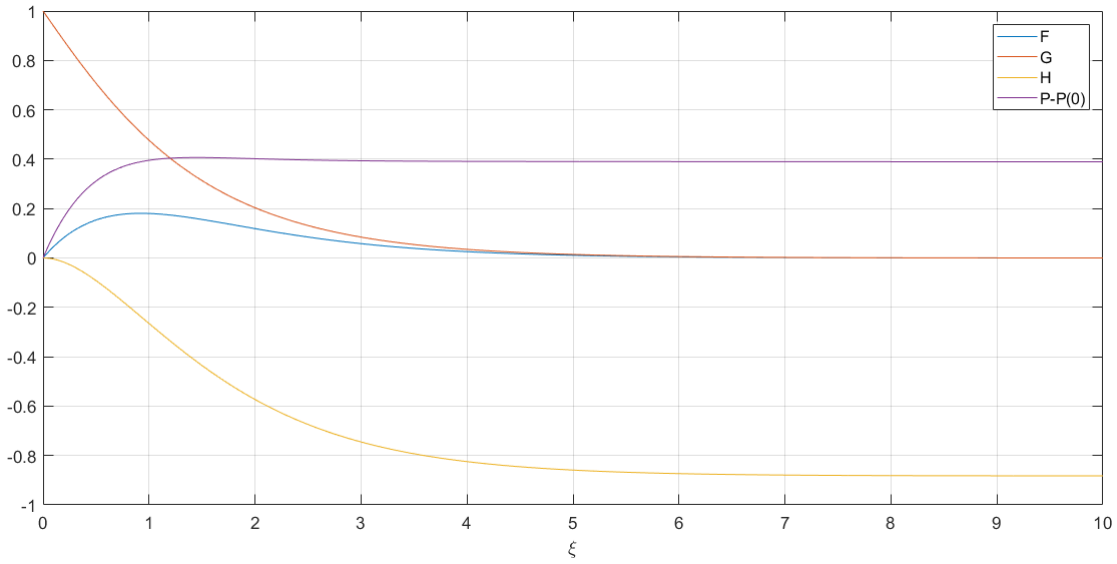

Figure 3.2: Solution of the ordinary differential Equations 3.5a - 3.5d.

The inflection point in the radial profile is well evident. The tangential variable G diminishes from its maximum value at the disc (Ωr) to zero with increasing height, and the axial profile starts from 0 on the surface and asymptotically tends to H = -0.8845. At last, the difference $P(\xi) - P(0)$ follows a similar behaviour as that of F, tending to 0.3911. According to the last term of Equation 3.4, a low region of pressure is created close to the disc's surface.

It is also stipulated that the thickness of the boundary layer for this case δ is given by the location at which the tangential velocity is 1% of the one given on the surface of the disc.

$$\delta = 5.5 \left(\frac{\nu}{\Omega}\right)^{\frac{1}{2}}. \tag{3.6}$$

Furthermore, the Reynolds number definition for rotational flows is:

$$Re_{\Omega} = r \left(\frac{\Omega}{\nu}\right)^{\frac{1}{2}}, \tag{3.7}$$

which represents the ratio between inertial to viscous forces, and is widely utilized to outline the laminar, transition and turbulent regimes.

For a finite disc, the Re_{Ω} at the edges of the disc, or Re_{edge}, is given by:

$$Re_{edge} = R_d \left(\frac{\Omega}{\nu}\right)^{\frac{1}{2}}. \tag{3.8}$$

3.3 Transition on a Rotating Disc

Lingwood [37] remarked that at Re_{Ω} = 510, an absolute instability was found to take place, which could potentially trigger the onset of transition to turbulent flow. The flow is said to be absolutely unstable when the response to a transient disturbance grows with time at the source. She also showed that Coriolis and streamline curvature effects do not play an important role in the transition mechanism.

The transitional Reynolds numbers experimentally discovered by several authors were neatly summarized by Healy [38], as shown in Figure 3.3. Several different criteria were employed but the indicator for detection of this value was always the same: the Reynolds number at which serious nonlinear distortion of waves first arose.

Authors	R_t	Method
Theodorsen & Regier (1944)	557	Hot-wire
Gregory, Stuart & Walker (1955)	533	Visual, China-clay
Cobb & Saunders (1956)	490	Heat transfer
Gregory & Walker (1960)	524	Pressure probe
Chin & Litt (1972)	510	Mass transfer
Fedorov *et al.* (1976)	515	Visual, napthalene
Clarkson, Chin & Shacter (1980)	562	Visual, dye
Kobayashi, Kohama & Takamadate (1980)	566	Hot-wire
Malik, Wilkinson & Orszag (1981)	520	Hot-wire
Wilkinson & Malik (1985)	550	Hot-wire
Lingwood (1996)	508	Hot-wire
Othman & Corke (2006)	539	Hot-wire

Figure 3.3: Experimental transitional Reynolds R_t previously remarked.

Imayama [39] offered an extensive review of the boundary layer resultant from the von Kármán problem. Additionally, he sought to investigate experimentally the processes that control the transition from laminar to turbulent regime, and to further asses the role of the various instabilities on this transitional phase of the flow. He remarked that, for $Re_\Omega > 430$, a broad peak centered around $2\pi f/\Omega = 30$ appears. This defined peak was discovered to be linked with the formation of steady vortices, initially studied by Gregory et al. [40]. These vortices can be seen in Figure 3.4. Fully turbulent regime was observed starting from $Re_\Omega = 650$.

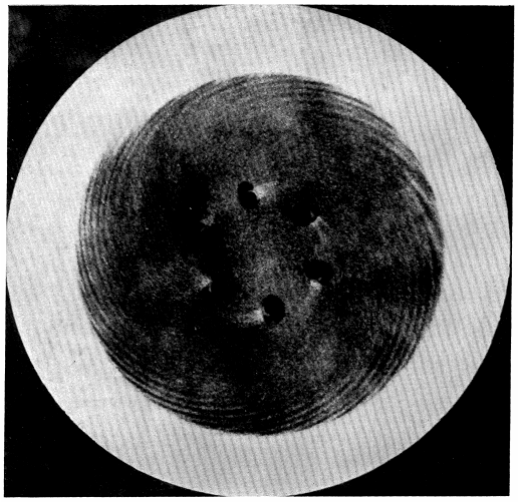

Figure 3.4: Instabilities on a rotating disc from Gregory et al. [40].

3.4 Numerical Model

By simulating the von Kármán problem through CFD and further confirming its results, trust is gained in the mesh resolution and chosen discretization methods, and confirmation that these are adequate for the main problem is attained.

3.4.1 Mesh

The computational meshes used for the present and future cases were all produced through the software $ANSYS$ Meshing.

The mesh comprises a cylindrical domain with radius and height of 6 D_d. In its basis, a separate circular region was defined, to serve as the rotating disc. At the center of the disc, the origin of the Cartesian coordinate system (X,Y,Z) was defined. Since here an infinite disc is not possible, a finite disc with radius R_d = 0.1 meters was used. The mesh is represented in Figures 3.5, 3.6 and 3.7.

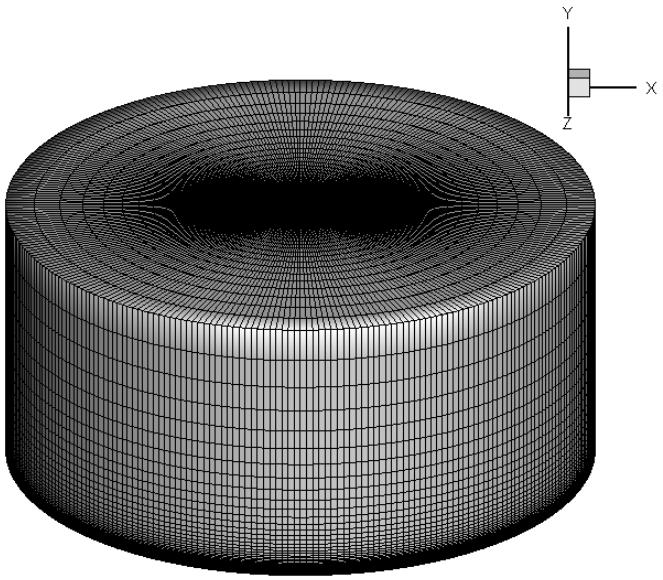

Figure 3.5: Cylindrical mesh.

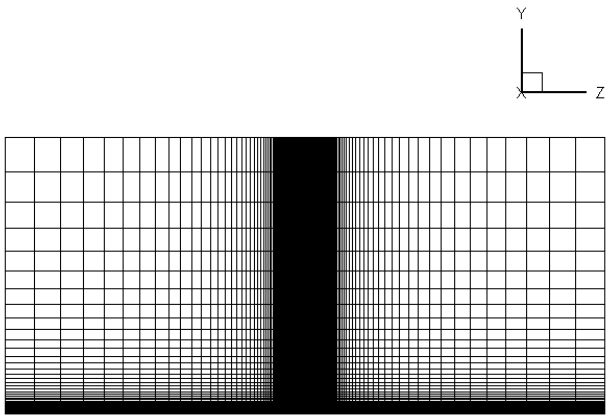

Figure 3.6: Slice by a X = 0 plane.

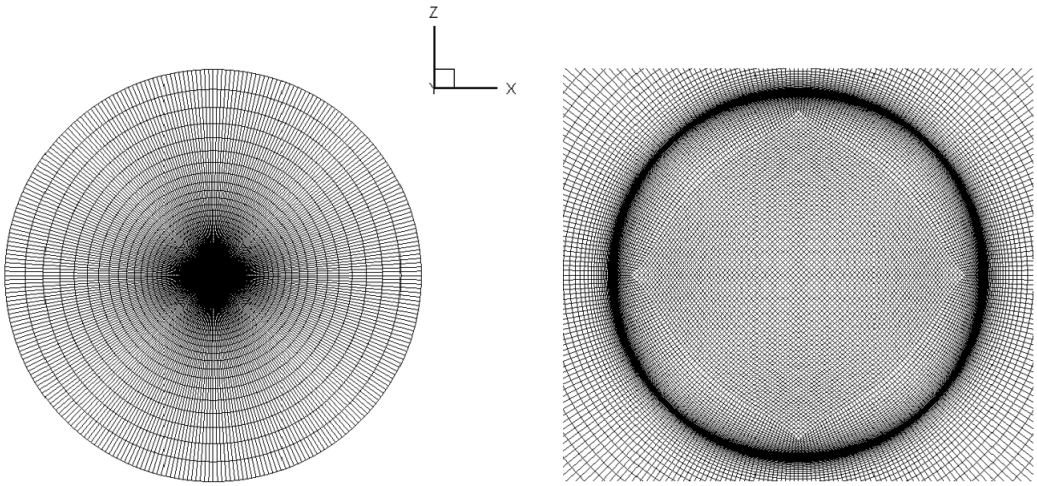

Figure 3.7: Top view of the mesh: (a) outer domain and (b) disc region.

Far-field boundaries were set at a distance of roughly 6 D_d from the disc, in both vertical and horizontal directions. These boundaries were required to be far away as to consider the effects of the boundaries as negligible. Otherwise, the results obtained would be akin to those of an interior flow problem.

The uppermost boundary of the domain was selected as a pressure inlet and the sides of the domain as pressure outlets. This combination resulted in an adequate representation of far-field boundaries in this naturally subsonic case. The bottom of the cylinder was considered as a symmetry plane and the rotating disc itself as a rotating wall. No slip-conditions were applied along the disc wall, meaning zero velocity and impermeability. The selected boundary conditions are illustrated in Figure 3.8.

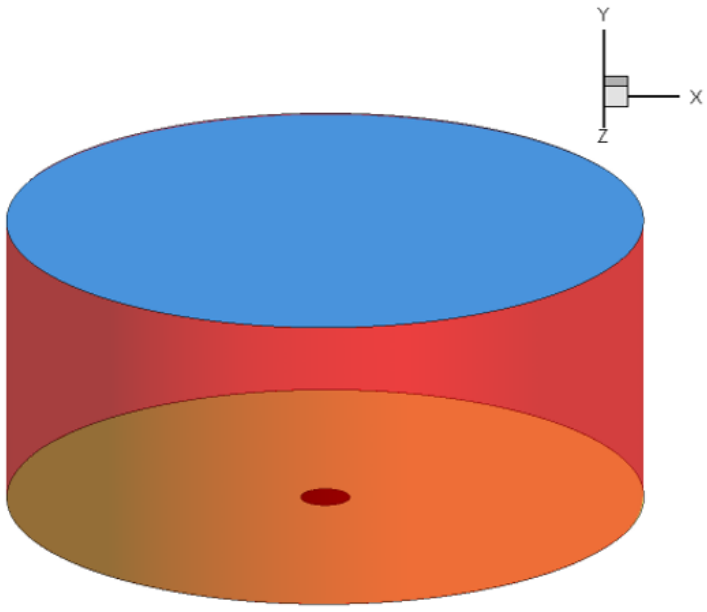

Figure 3.8: Scheme of the boundary conditions prescribed for the cylindrical mesh. Pressure inlet (blue), pressure outlet (red), symmetry (yellow) and no-slip wall (black).

A structured mesh was preferred over an unstructured mesh. Despite a much more arduous generation, a structured mesh is rather apt at solving boundary layers near walls. Also, it enables an organized, and thus simpler, storage process, granting easier access to each and every cell, making the calculation of fluxes and gradients considerably easier.

The domain was divided into two parts: a cylinder encompassing the disc at its basis; and an outer cylinder (the remainder of the domain). In order to obtain a structured, approximately uniform mesh on the surface of the disc, this separation had to be carried out. However, since refinement near the edge of the disc had to be included (namely, inflation layers), some skewed cells were unavoidable. One can alleviate this issue by considering the physics of the problem. Since a strong perturbation of the flow will nonetheless appear on the edges of the disc, due to the discontinuity present there, the results obtained at that region will not be adequate for validation. With this in mind, the rather skewed cells were placed at an agreeable distance from the edge, while the remainder of the disc was designed as uniform in the radial direction. This will enable an accurate solution in the disc surface far from the edges.

Two inflation layers were generated to properly capture phenomenons close to the disc. The first, and perhaps the most essential, was in the axial direction. By keeping in mind that the boundary layer thickness decreases as Re_Ω number increases (Formula 3.6), the inflation layers were built around the boundary layer characteristics of a rotational Reynolds close to transition, since only the laminar domain is of interest. By following Equations 3.6 and 3.7, and considering data from a case in imminent transition (Re_Ω = 500), a boundary layer thickness of $\delta = 1.1e^{-3}$ meters is obtained. This axial distance was covered with around 40 cell layers, resulting in first cell height h_1 of approximately $5.8e^{-6}$ meters. The other refinement was created at the interface between the disc and the outer region, in order to accurately capture the discontinuity present there. This double inflation lead to cells with enormous aspect ratios. However, these were present at the periphery of the domain, outside of the disc, where the velocity gradients are expected to be quite small, thus not posing a serious concern. The aspect ratio of cells in the disc region was nevertheless controlled as to avoid unnecessary uneven cells and hindering the solver performance.

The resulting mesh contained around 3.8 million nodes, which assured a satisfactory compromise between computational effort and solution accuracy.

3.4.2 Discretization Schemes

The commercial package $FLUENT$ was used for all simulations.

This problem is steady, laminar and incompressible. Naturally, a pressure-based approach was selected as it was purposefully designed for low velocity flows. Additionally, the SIMPLE algorithm was chosen to solve the coupling between pressure and velocity. For pressure, a second-order scheme was utilized and for momentum equations, the QUICK scheme.

3.5 Problem Parameters

To broaden this CFD study, three distinct cases with different Re_Ω were studied. To change this parameter, only the angular velocity of the disc Ω was altered. Initially, the radius at which data was gathered was fixed at 30% R_d. A measuring radius far from the edges was preferred mainly for two reasons. Firstly, as was previously discussed, there is a discontinuity between the edge of the disc and the outer region, therefore collecting data far from this region was preferable. Secondly, non-linear behaviour is expected near the edge of the disc for the case with the highest Re_Ω, which might corrupt the accuracy of the data collected.

The Re_Ω and the Reynolds number on the edge of the disc Re_{edge} can be seen in the Table 3.1.

Case	Ω [rad/s]	Re_Ω	Re_{edge}
1	0.04	1.65	5.5
2	4.38	16.50	55
3	365.18	150	500

Table 3.1: Values for each case.

The range of Re_Ω was chosen as to study the behaviour of the classic von Kármán problem when the flow was either highly viscous (Case 1 - Low Re_Ω), on the verge of transition on the border of the disc (Case 3 - High Re_Ω) or in between the previous cases (Case 2 - Intermediate Re_Ω).

3.6 Results

To assess the precision of the CFD results, values of G, F and H at different ξ were gathered at different heights from the disc and compared to their theoretical predictions. Figure 3.9 illustrates this comparison. Cases 2 and 3 produced excellent results, with the latter showcasing a slightly better agreement with the theoretical predictions. On the other hand, obtained data from case 1 break away from the expected trend. Especially so for the axial profile, where the curve actually rises to higher values of H instead of having an asymptotic behaviour towards H = -0.8845.

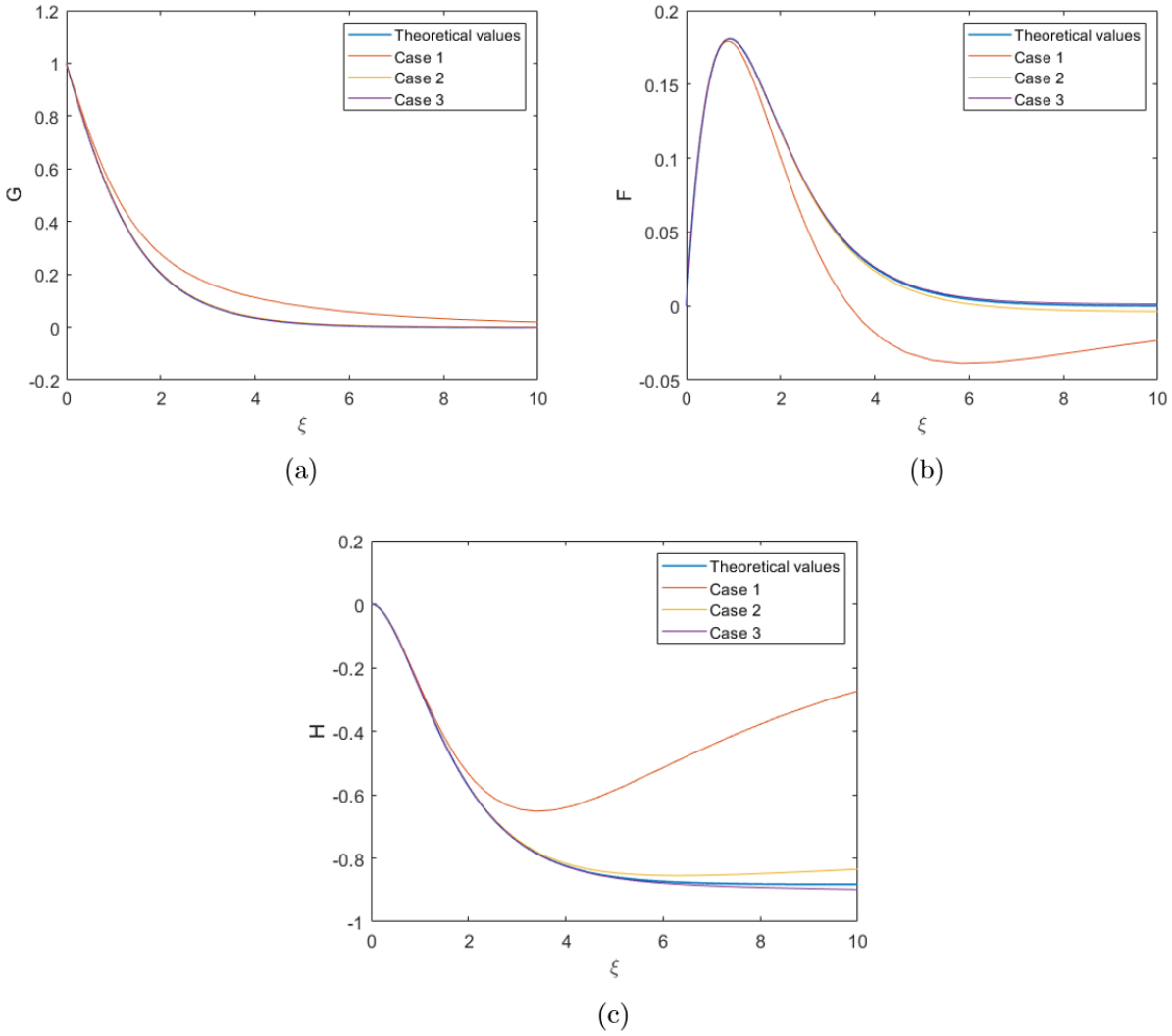

Figure 3.9: Comparison of (a) G, (b) F and (c) H values between theoretical and CFD results.

3.6.1 Discussion

The disparities between case 1 results and the theoretical curves can be explained by visualising the velocity profiles. Here, the velocity vectors were projected onto a ZY plane. The velocity values were made adimensional by $1/\Omega R_d$. Only half of the domain was represented, since the problem is symmetric with respect to the Y axis. Figures 3.10, 3.11 and 3.12 represent these projected profiles. Far from the edge of the disc, the velocity profile for cases 2 and 3 are as expected, with the flow being drawn axially towards the disc, and then being subject to a centrifugal motion. This causes radial expulsion of the flow. Immediately noticeable is the erratic profile on the tip of the disc in Figure 3.12. This behaviour was anticipated, since, near the edge, Re_Ω increases to the vicinity of expected transitional values. For case 1, a recirculation can be observed slightly above the edges of the disc in Figure 3.10, no doubt due to the intense viscous effects, justified by the low rotational Reynolds number. As seen in Figures 3.11 and 3.12, this anomaly is not present in both cases 2 and 3, which ultimately translates to much better agreement between practical and theoretical values.

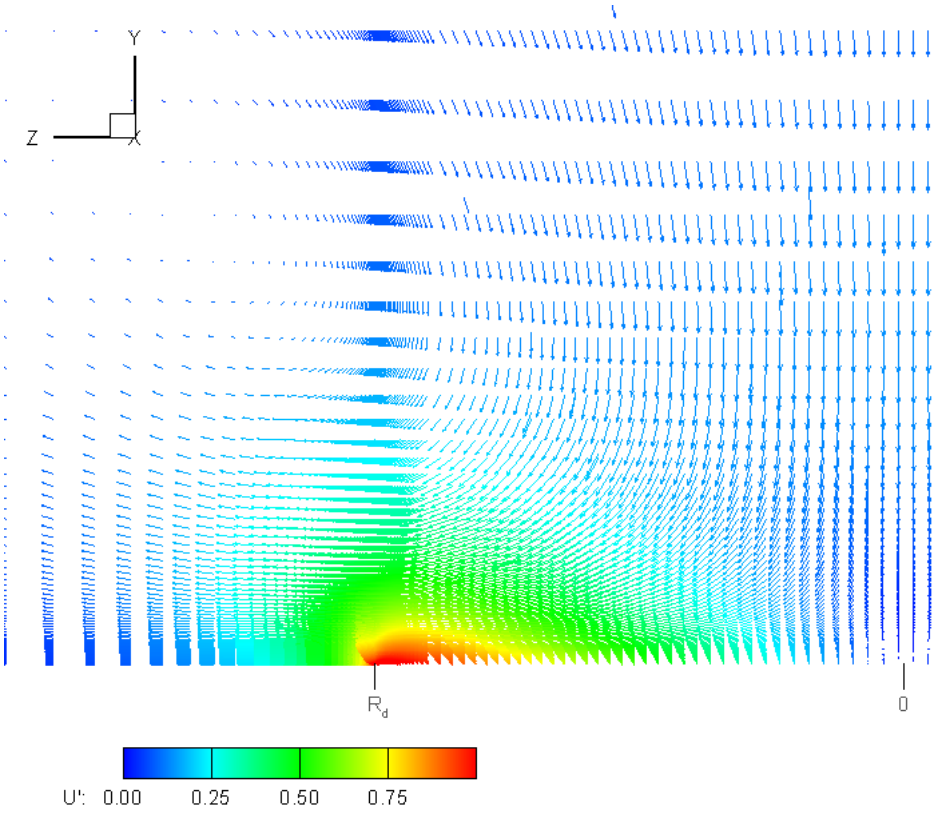

Figure 3.10: Projected velocity profile of case 1.

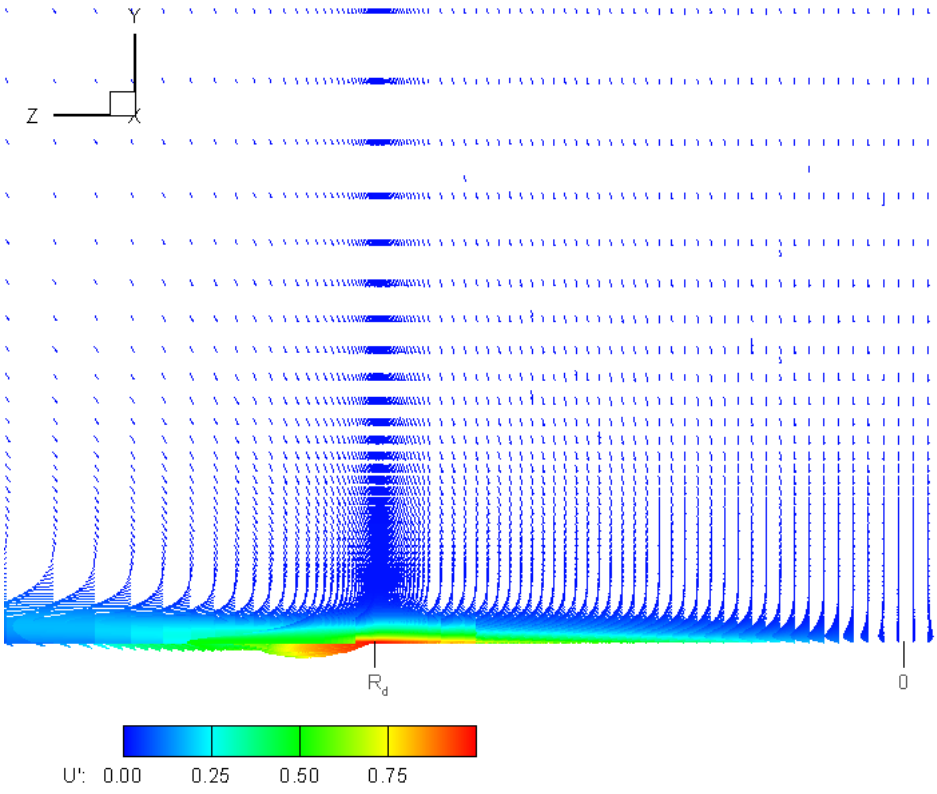

Figure 3.11: Projected velocity profile of case 2.

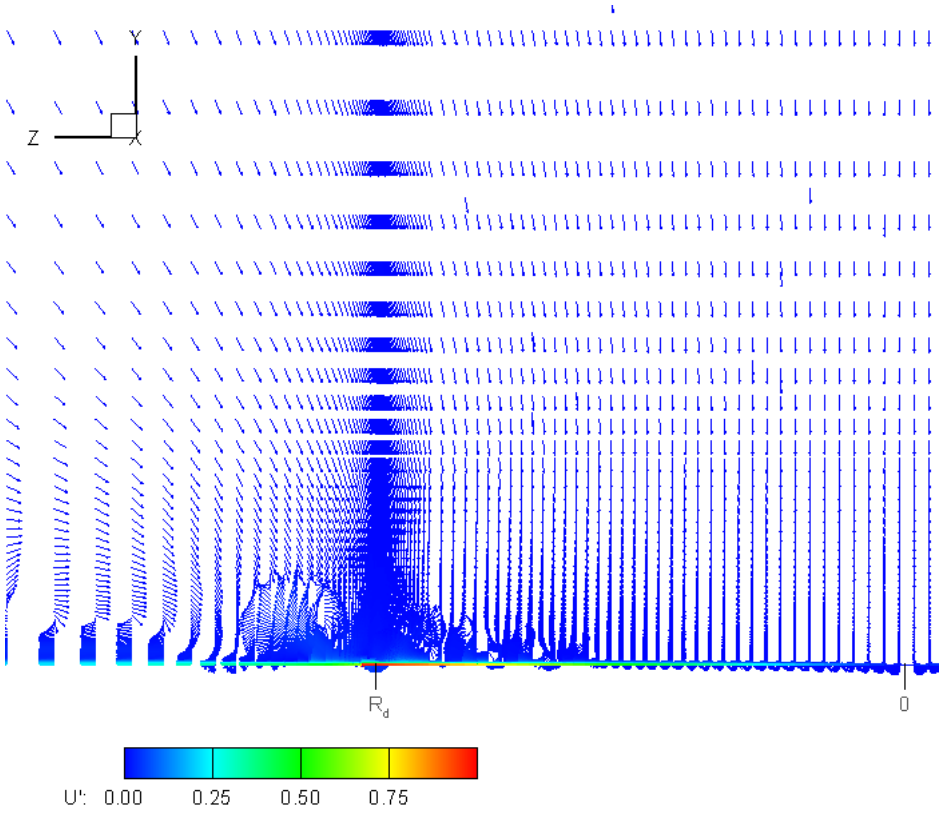

Figure 3.12: Projected velocity profile of case 3.

To explore how this recirculation corrupts the accuracy of the data collected, new data was obtained at different positions of the disc. Instead of just gathering values from 30% of the radius of the disc, other measurements were made at increasing distance from the center of the disc. This was done to both cases 1 and 2. For case 3 however, this was not carried out due to the transitional instabilities present near the edge of the disc (evident in Figure 3.12). Data of tangential, radial and axial velocity far from the center of the disc would undoubtedly be affected by these instabilities, which, for this laminar flow problem, are unforeseen.

Figure 3.13 reflects this change of measurement radius for case 1 and Figure 3.14 for case 2. It can be seen that, for case 1, the results change drastically with measuring radius. For case 2 however, despite a slight change in values of G and F at 5% radius, the results remain practically the same.

At the center of the disc, r = 0 leads to a singularity in both formulas of G and F (Formula 3.4). Therefore, data of these values in the immediate vicinity of the origin are expected to be erroneous. A selected distance of 5% radius, on which data is obtained, is apparently close enough to produce a small discrepancy, but not in values of H. This was expected, as this variable does not depend on the radius. This leads to the conclusion that for obtaining future values of tangential and radial velocity, a high enough distance has to be selected (10% radius should suffice).

There are additional problems concerning case 1. As was previously stated, the length of the inflation layers of the mesh in the axial direction was based on adequate values for case 3. Therefore, the created mesh is much more apt at capturing the phenomenons in the boundary layer for Re_Ω = 500, while having a weaker performance for much lower Reynolds (case 1), leading to erroneous results. Also, the thin boundary layer approximations can only be considered for a high enough Reynolds number. This, coupled with the fact that this problem was deduced for infinite radius, and thus infinite Re_Ω, explain the poor G, F and H results for Re_Ω = 5.5, since several of the simplifications to the Navier-Stokes equations that were previously applied are not valid.

Overall, the simulations successfully replicated the von Kármán problem with the intended accuracy. The mesh resolution and used methods were deemed applicable to this kind of rotational flow.

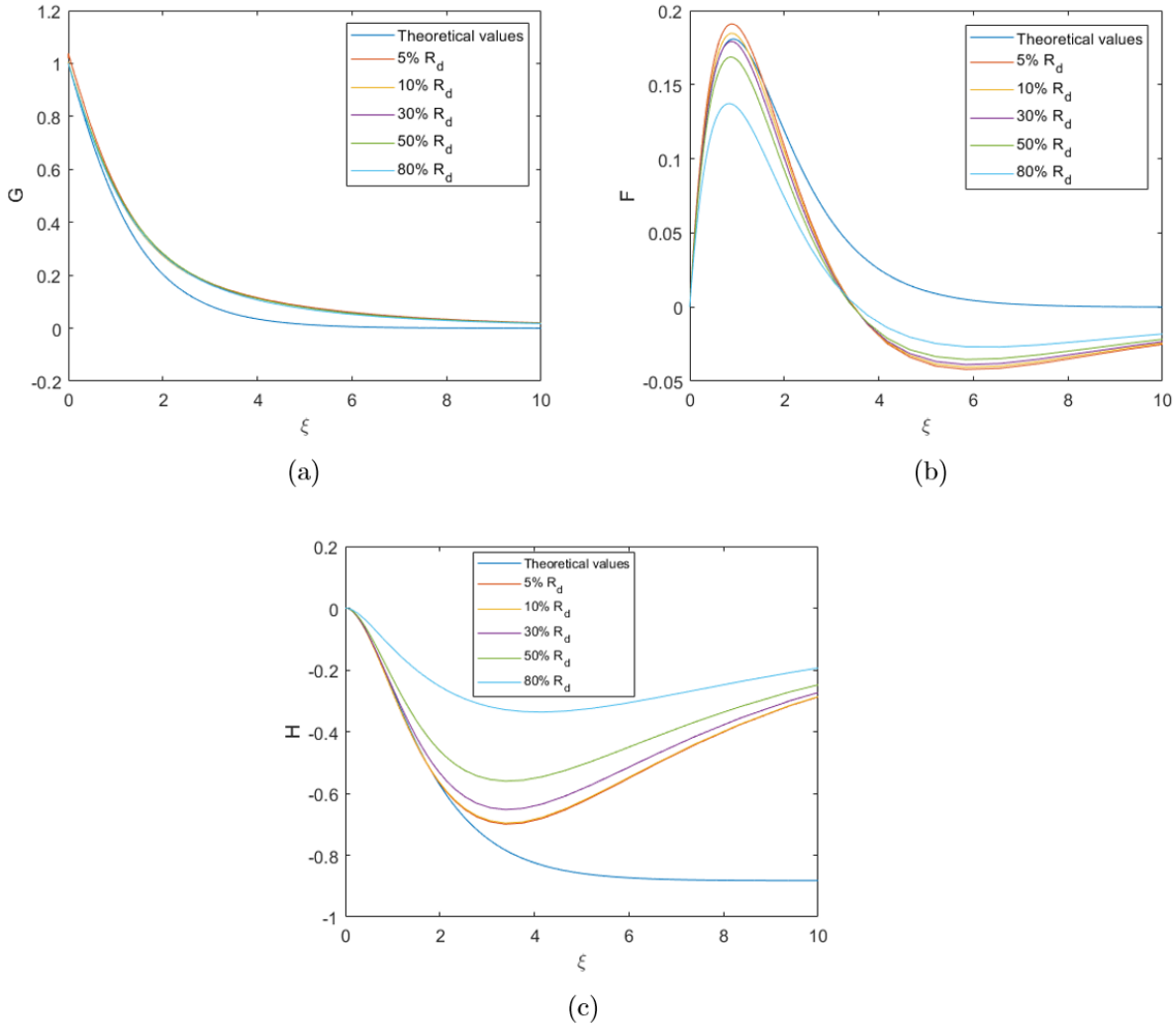

Figure 3.13: Evolution of (a) G, (b) F and (c) H from case 1 for several measuring radii.

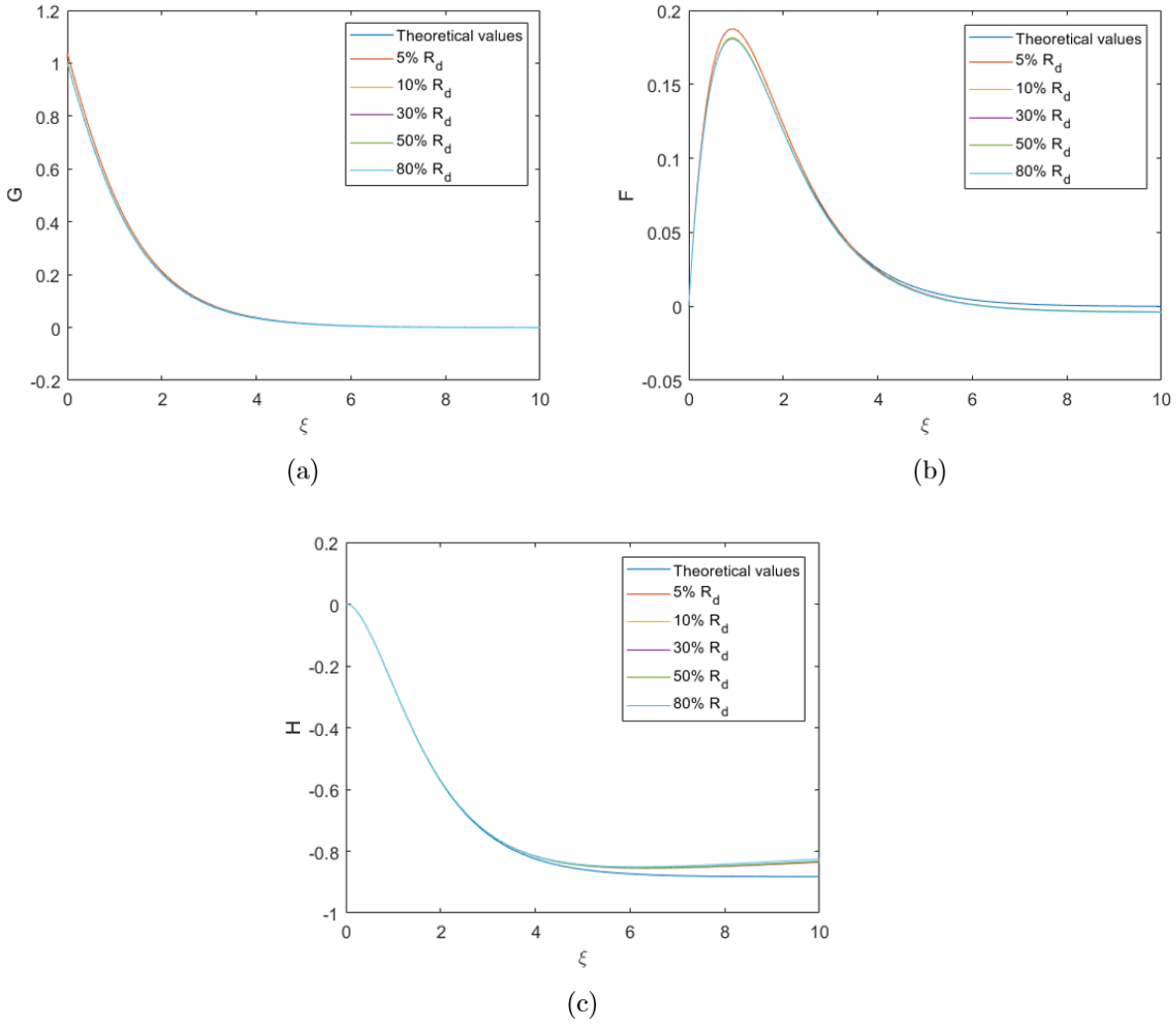

Figure 3.14: Evolution of (a) G, (b) F and (c) H from case 2 for several measuring radii.

Chapter 4

Problem Formulation

4.1 Definitions

As opposed to the previous problem, a rotating disc will now be evaluated in flight condition at several angles of attack. As such, some new definitions are in order. The Reynolds number based on the free stream velocity is given by:

$$Re = \frac{D_d U_\infty}{\nu}. \tag{4.1}$$

The Reynolds number based purely on disc rotation is once again given by Formula 3.7, repeated here for convenience.

$$Re_\Omega = r\left(\frac{\Omega}{\nu}\right)^{\frac{1}{2}}, \tag{3.7}$$

and Re_{edge} is obtained through Formula 3.8:

$$Re_{edge} = R_d\left(\frac{\Omega}{\nu}\right)^{\frac{1}{2}}. \tag{3.8}$$

To facilitate a direct comparison between previous and eventual future studies, all relevant flow variables were adimensionalized as such:

$$\frac{U}{U_\infty}, \qquad \frac{p - p_\infty}{\frac{1}{2}\rho U_\infty^2} = C_p, \qquad \frac{tU_\infty}{D_d} = t', \qquad \frac{\tau_w}{\frac{1}{2}\rho U_\infty^2} = C_f, \qquad \frac{k}{U_\infty^2} = k'.$$

where t and k are time and turbulence kinetic energy, respectively.

The angle of attack, or α, is defined as the inclination between the longitudinal axis of the disc and the incoming airflow. This variable was adjusted by varying the components of the incoming flow.

4.2 Numerical Model

4.2.1 New Mesh

From the conclusions of chapter 3, confirmation that the used mesh was suitable to capture and portray near-wall phenomenons of the von Kármán problem was obtained. The next logical step was to mirror the mesh with regards to a XZ plane in order to account for the expected asymmetry. The full mesh is represented in Figures 4.1 and 4.2.

The disc has zero thickness as this study intends to assess aerodynamic forces and performance, while neglecting gyroscopic precession.

Some small alterations were made to the original mesh however. The cells on the surface of the disc were aligned with the incoming flow (X direction) and the radius of the disc was doubled to 0.2 meters. This last change was made as to facilitate comparison with the experimental study of the current problem, that was being carried out at the time of writing.

Moreover, since free stream velocity is now present and the disc is now bigger in radius, the far field boundaries had to be pushed back. Seeing as the present case is similar to one with flow over an airfoil, the outer boundaries were placed at a distance of 10 chords from the disc, as this distance has previously produced agreeable results [41]. Here, chord is taken to be D_d and thus the distance of 10 D_d was used.

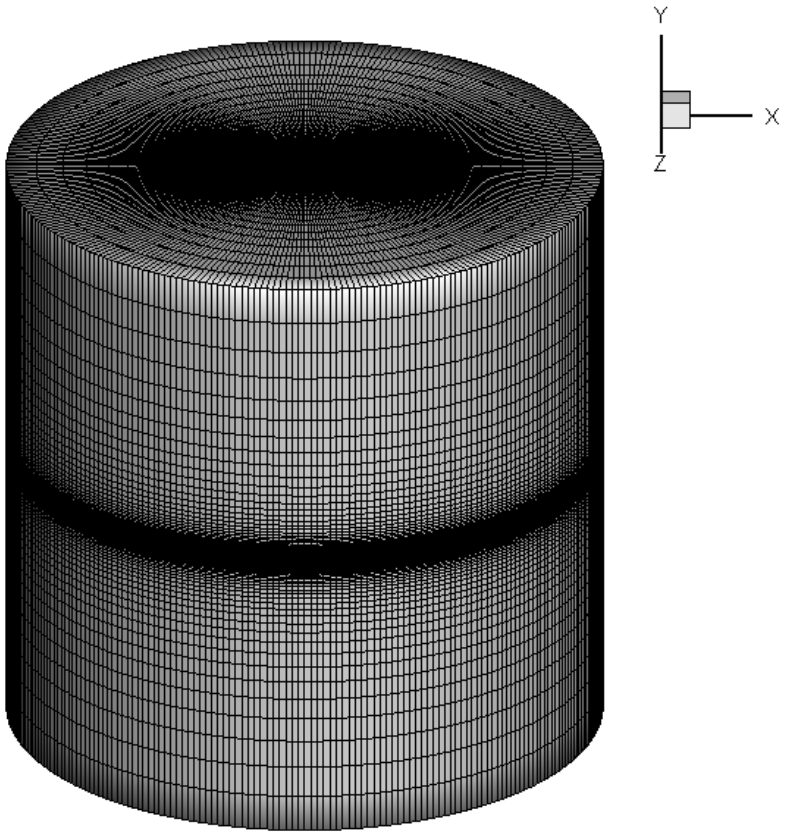

Figure 4.1: Final mesh.

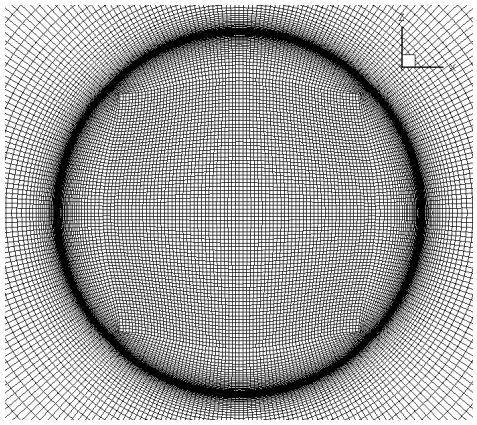

Figure 4.2: Top view of the final mesh zoomed in.

Also, to ease the computational effort, the axial refinement around the disc was made coarser. The first cell height closest to the disc was altered from $5.8e^{-6}$ to $1.9e^{-5}$ meters. This placement assured satisfactory y^+ values, as will be seen in section 4.2.3.

The top and bottom faces of the domain were deemed as periodic interfaces. The side face was divided in half by a YZ plane, as to consider the portion at negative X values as a velocity inlet, and the one at positive X values as a pressure outlet. At the center of domain, the disc was once again chosen as a rotating, no-slip wall. The choice of boundary conditions is represented in Figure 4.3.

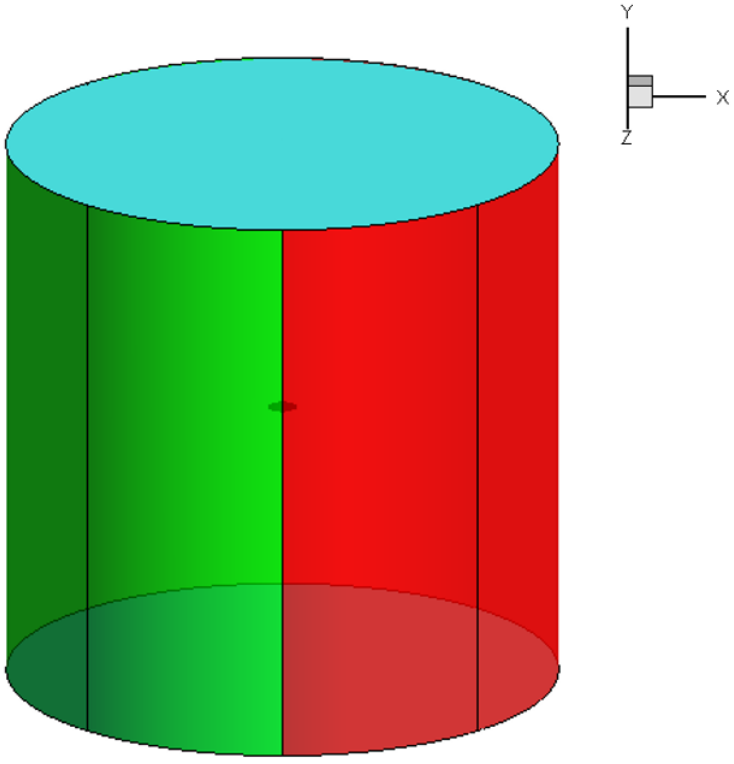

Figure 4.3: Scheme of the prescribed boundary conditions for the final mesh. Periodic (teal), velocity inlet (green), pressure outlet (red) and no-slip wall (black).

The end result was a mesh with 7.6 million nodes.

Several attempts at devising a better mesh configuration were made. These alternative meshes are showcased in Appendix A.

Von Kármán Problem Rerun

To ensure that this new mesh was not detrimental to the overall accuracy of the data gathered (since it is coarser on the axial direction near the disc), the von Kármán problem was again tackled. Case 2, which translates to Re_{edge} = 55, was chosen. To account for the increase in radius of the disc, the rotational velocity had to be properly scaled. The measurement radius was once again 30% R_d. The results obtained from this new mesh can be seen in Figure 4.4.

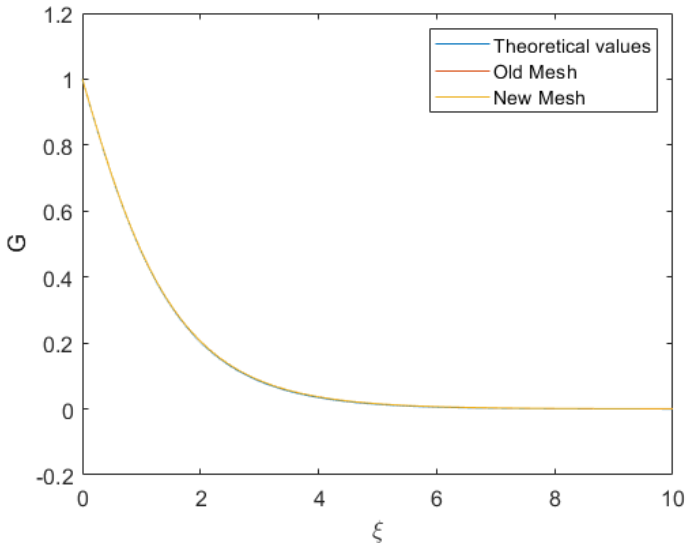

Figure 4.4: Evolution of G values from case 2 of the old and new mesh.

As was the case with radial and axial velocities values, the difference in the results between the old and new mesh is almost imperceptible. To avoid redundancies, only the tangential profile was represented.

Overall, it is evident that the new mesh is as suitable as the old one at solving laminar rotational flow problems.

4.2.2 Discretization Schemes

Since this remains an incompressible problem, a pressure-based solver was once again chosen. SIMPLE was selected for the pressure-velocity coupling. To finalize the choice of schemes, second-order for pressure, QUICK for momentum and turbulent equations were selected once more. However, a temporal method is now required due to the unsteady nature of this problem. The implicit second-order scheme was used due to its unconditional stability. For the time step size, guidelines were found by taking into account the time an element of fluid takes to travel the length of the disc and the entirety of the computational domain. After a careful investigation, regarding time-step independence, convergence, computational resources and resolution, t_c = 0.005 s yielded the most satisfactory agreement.

4.2.3 Turbulence Model

For the purpose of the present numerical simulations, the model IDDES was chosen. Its formulation is explained in Appendix B. The complicated flow separations and vortical phenomenons, naturally present for such a problem with high degree of rotation at $\alpha \neq 0°$, should be adequately resolved in order to register accurate aerodynamic data. As such, and because enough computational resources were available, this improved version of DES was selected. Values of y^+ were controlled as to ensure that the viscous sub-layer was always properly resolved. These were in the order of unity. Turbulence intensity at boundaries was prescribed as 1%.

4.3 Problem Parameters

A Reynolds number given by the Formula 4.1 of 150,000 was chosen, typical for a fixed-wing MAV operation. So by Formula 4.1, and fixing the kinematic viscosity at 1.46 x $10^{-5} m^2/s$, follows that U_∞ = 5.478 m/s. The flow direction is (1,0,0).

The disc is rotating at a fixed angular velocity Ω with both the top (+Y) and bottom surface (-Y) initially rotating in the same direction. Later, differential rotation was applied, meaning that each surface has its own $AdvR$. The rational behind the choice of $AdvR$ was to start from a disc flying without rotation ($AdvR$ = 0) and sequentially increase the spinning until turbulence is expected on the majority of the disc ($AdvR$ = 8), according to Lingwood [37]. All cases are summarized on Table 4.1.

$AdvR$	Ω $[rad/s]$	Re_{edge}
0	0	0
0.5	13.67	193
1	27.39	274
2	54.78	387
4	109.56	548
8	219.12	775

Table 4.1: Values for each case.

Aerodynamic coefficients of lift and drag were calculated with regards to the free stream velocity axes, and the moment coefficients relative to the body axes. The moments were taken about the center of the disc.

Finally, the circular disc has no thickness, with R_d = 0.2 m. The angle of attack assumed values of 0°, 5° and 10°, as these are typical values for fixed-wing MAV operations. For the first two angles of attack, the full range of $AdvR$ was tested. However, only $AdvR$ = 0 and differential rotation were simulated for α = 10°.

Chapter 5

Results for α = 0°

5.1 Turbulence Kinetic Energy

To better asses the effect of disc rotation on turbulence production and the wake, Figure 5.1 represents the evolution of turbulence kinetic energy contours on the plane longitudinal to the disc.

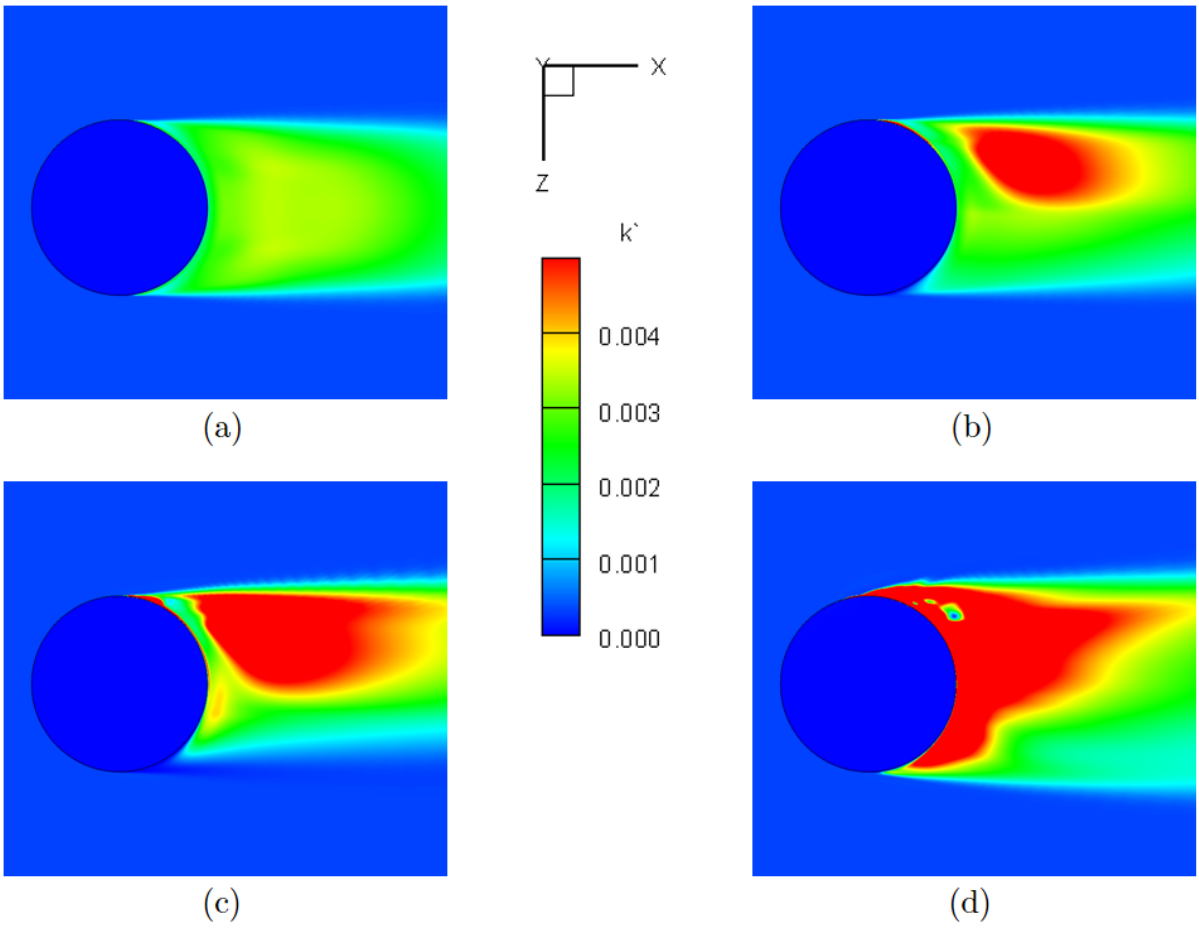

Figure 5.1: Turbulence kinetic energy distributions for $AdvR$ = (a) 0, (b) 0.5, (c) 1 and (d) 2.

As expected, when rotation is increased, the turbulence intensity in the wake grows stronger.

Without rotation, the k distribution is symmetric to the longitudinal axis. When the disc is spinning however, turbulence is seen to be more intense at the advancing side of the disc and weaker at the retreating side, which indicates early and delayed transition, respectively. These remarks are supported by observations from Higuchi et al. [23]. In fact, k is steeply reduced at the retreating side for $AdvR$ = 1, and while high values cover most of the trailing edge for $AdvR$ = 2, this delay is also evident. Additionally, the wake is seen to become asymmetric and not aligned with the direction of the flow, characteristic of the asymmetry caused by disc rotation, previously remarked by Nakamura and Fukamachi [20].

5.2 Vortical Structures

5.2.1 Comparison of Methods for Vortex Identification

To determine which technique for representation of vortical structures should be utilized henceforth, a direct comparison of four vortex methods was carried out for a generic case ($AdvR$ = 2 was chosen). These are introduced in Appendix C. According to the equivalent thresholds presented by Chen et al. [42], isosurfaces of Q, λ_2 and swirl strength were built around values of 0.45, -0.45 and 1.5, respectively. For the isosurface of vorticity, ω = 25 s^{-1} was chosen because by selecting this value, the resulting flow structures were the most similar to the ones produced by the other methods, thus being apt for direct comparison. The four resulting isosurfaces, filled with velocity contours, are observed in Figure 5.2.

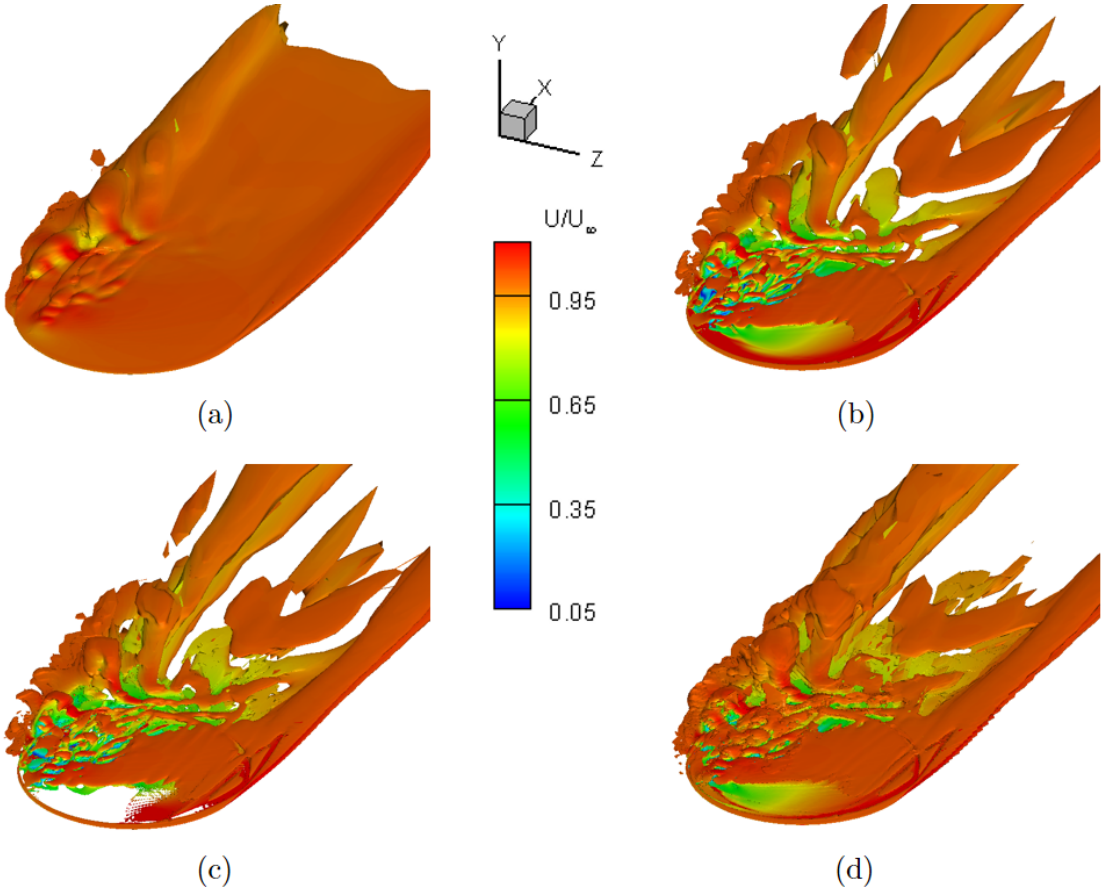

Figure 5.2: Isosurfaces of (a) vorticity, (b) Q, (c) λ_2 and (d) swirl strength for $AdvR$ = 2.

Vorticity offered a highly superficial version of the events, lacking detail in just about every portion on the disc and wake. This was caused by the high degree of vorticity within the boundary and shear layers, which are unfiltered by this method, effectively hiding the relevant flow structures, even though the high degree of vortical structures on the advancing side was correctly identified. Also, no guidelines for the value of the isosurface were available, suggesting that this method pales in comparison to the remaining 3.

The other methods drew exceedingly detailed and globally similar vortical structures, with a few mismatches however. The λ_2 method seems to lack resolution near the leading edge and swirl strength produces lower quality structures, particularly so on the advancing side. The Q criterion is free of these complications and offers better resolution, thus being the preferred method for vortex visualization.

5.2.2 Isosurfaces of Q

The effects of increasing disc rotation can be further studied by comparing Q = 0.45 isosurfaces. In addition to the instantaneous visualizations, surfaces of averaged Q of 55 t' are represented in Figure 5.3 for all unsteady cases. These surfaces were obtained by considering the tensor of time-averaged velocities to calculate Q and are useful to determine the structures that persist the averaging process.

Immediately noticeable is the rising complexity and number of vortices identified by the Q criterion as rotation is escalated. These structures are unlike the stationary vortices observed by Gregory et al. [40] for a typical rotating disc, as in Figure 3.4. This disparity highlights the impact that adding free stream velocity to a typical von Kármán problem truly has.

Starting from $AdvR$ = 0.5 and 1, long structures that detach from the surface are only visible on the rear portion of the disc, while the surface is relatively free of any significant vortical motion. Next, for $AdvR$ = 2, instabilities arise and the problem ceases to be stationary, with small eddies occupying most of the advancing side and the wake region. These eventually migrate upstream, to the leading edge, for $AdvR$ = 4. When maximum rotation is applied to the disc ($AdvR$ = 8), the entirety of the surface is covered by disturbances. The growing importance of turbulent structures with $AdvR$ is consistent with the evolution reported by Wiesche [32]. The retreating side always showcases less vortical motion, consistent with the observations from k contours in Figure 5.1.

Also noteworthy is the appearance and eventual growth of hairpin-like vortices on the surface of the disc, visible in Figures 5.3 (e) and (f). These are presumably associated with flow separation.

Figures 5.3 (h) and (i) both highlight a long, well defined coherent structure on the retreating side. Apparently, this large scale tip vortex does not come into contact with the wake's structures. Additionally, stretched longitudinal vortices that reach the trailing edge are present on the middle section of the disc. Comparing the full range of mean isosurfaces (Figures 5.3 (g), (h) and (i)), the middle section of the wake is initially free of any significant vortical motion, but as rotation increases, this region becomes more and more affected by the fluctuations happening upstream. Moreover, the well defined coherent structures on the aft portion move sequentially towards the leading edge, by the sides, hinting that added rotation promotes the earlier appearance of vortical motion and thus turbulence production on both sides.

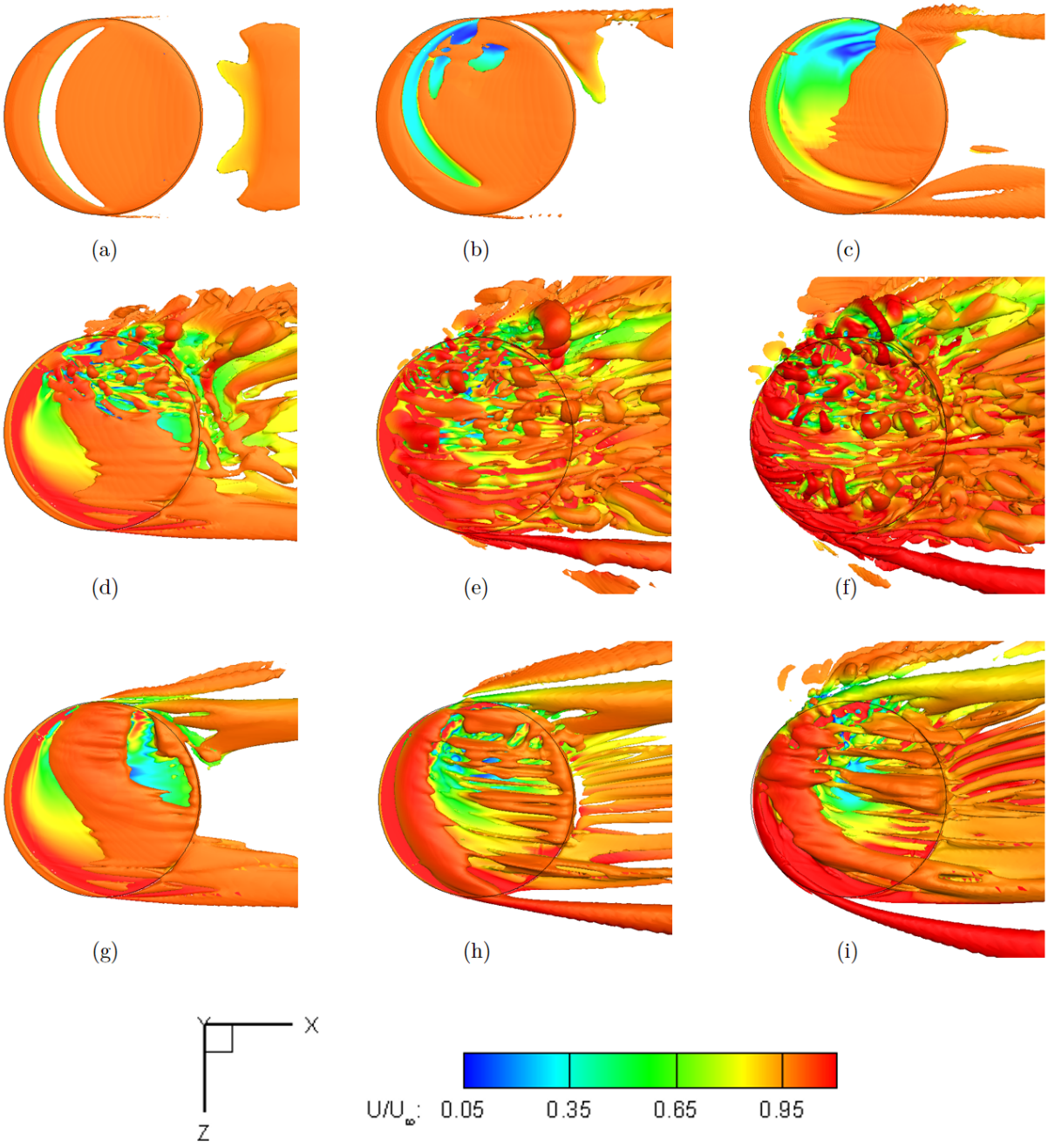

Figure 5.3: Top view of Q isosurfaces for $AdvR$ = (a) 0, (b) 0.5, (c) 1, (d) 2, (e) 4, (f) 8 and mean Q isosurfaces for $AdvR$ = (g) 2, (h) 4 and (i) 8.

5.3 Aerodynamic Coefficients

5.3.1 Full Disc

In order to better understand the aerodynamic impact that increasing rotation causes, coefficients of lift, drag and moments were calculated. Results for the full disc are summarized in Table 5.1. Here, low orders of magnitude (10^{-5} or lower) were approximated as zero.

$AdvR$	C_L	C_D	$C_M\ roll$	$C_M\ pitch$	$C_M\ yaw$
0	0	1.22 e^{-2}	0	0	0
0.5	0	1.27 e^{-2}	0	0	-2.19 e^{-3}
1	0	1.36 e^{-2}	0	0	-4.42 e^{-3}
2	0	1.43 e^{-2}	0	0	-1.02 e^{-2}
4	0	1.99 e^{-2}	0	0	-3.08 e^{-2}
8	0	2.45 e^{-2}	0	0	-0.104

Table 5.1: Mean aerodynamic coefficients of the full disc for α = 0°.

Unsurprisingly, drag increases with $AdvR$, as rotation is sure to generate intense pressure gradients and high degree of turbulence. Yaw follows the same trend, because with added rotation, higher moments relative to the Y axis will surely appear. Lift, rolling and pitching moments were expected to be approximately zero, since the symmetric geometry of the disc at α = 0° produces a symmetric flow situation, causing the effects on the top and bottom surfaces to counteract each other.

Up to $AdvR$ = 1, the coefficients reached a steady value. For higher values of $AdvR$ however, unsteady behaviour was observed, justified by the generated vortical and turbulent structures. Values of aerodynamic coefficients were obtained through time averages of at least 55 t', after ensuring that a statistically steady state was reached.

In order to quantify the unsteadiness associated with each averaged measurement, the Root Mean Square Deviation (RMSD), given by Equation 5.1, was calculated through the sampled measurements.

$$RMSD = \sqrt{\frac{\sum_{i=1}^{n}(x_i - \bar{x})^2}{n}}. \tag{5.1}$$

The variables x_i, $\bar{x}$ and n are the measured value, averaged value and number of samples, respectively. RMSD can be understood as simply squaring each residual, averaging and then taking the root mean square of the result. This way, a deeper understanding of the deviation inevitably present from the averaged value in each unsteady case can be found. The results are summarized in Table 5.2.

$AdvR$	C_L	C_D	$C_M\ roll$	$C_M\ pitch$	$C_M\ yaw$
0	0	0	0	0	0
0.5	0	0	0	0	0
1	0	0	0	0	0
2	1.25 e^{-3}	1.54 e^{-4}	3.33 e^{-4}	3.97 e^{-4}	7.09 e^{-5}
4	1.97 e^{-3}	4.37 e^{-4}	5.48 e^{-4}	5.27 e^{-4}	1.36 e^{-4}
8	6.15 e^{-3}	7.39 e^{-4}	1.99 e^{-3}	1.91 e^{-3}	3.28 e^{-4}

Table 5.2: RMSD of the measurements from Table 5.1.

Since the first 3 cases reached a steady state, no deviation was present and thus RMSD = 0.

The calculated RMSD values are shown to increase with $AdvR$, although even at $AdvR$ = 8, their relative weight is fairly weak, adding trust to the time-averaged values.

5.3.2 Half Disc

Since at zero incidence the problem is symmetric by nature, no insight into the evolution of lift, roll and pitch was gained by analyzing the aerodynamic coefficients for the whole geometry. To solve this issue, only the upper surface of the disc (+Y) was considered here. The results are summarized in Tables 5.3 and 5.4.

$AdvR$	C_L	C_D	$C_M\ roll$	$C_M\ pitch$	$C_M\ yaw$
0	4.62 e^{-3}	6.13 e^{-3}	0	0	0
0.5	4.98 e^{-3}	6.36 e^{-3}	-1.58 e^{-4}	1.01 e^{-3}	-1.09 e^{-3}
1	6.71 e^{-3}	6.78 e^{-3}	-1.12 e^{-4}	1.71 e^{-3}	-2.21 e^{-3}
2	1.58 e^{-2}	7.16 e^{-3}	1.14 e^{-3}	1.69 e^{-3}	-5.12 e^{-3}
4	3.73 e^{-2}	9.88 e^{-3}	4.39 e^{-4}	-3.91 e^{-3}	-1.54 e^{-2}
8	9.13 e^{-2}	1.22 e^{-2}	7.33 e^{-4}	-1.99 e^{-2}	-5.17 e^{-2}

Table 5.3: Mean aerodynamic coefficients for the upper surface of the disc for α = 0°.

$AdvR$	C_L	C_D	$C_M\ roll$	$C_M\ pitch$	$C_M\ yaw$
0	0	0	0	0	0
0.5	0	0	0	0	0
1	0	0	0	0	0
2	6.15 e^{-4}	1.77 e^{-4}	1.87 e^{-4}	2.17 e^{-4}	7.43 e^{-5}
4	1.29 e^{-3}	2.81 e^{-4}	3.72 e^{-4}	4.35 e^{-4}	9.52 e^{-5}
8	4.46 e^{-3}	4.54 e^{-4}	1.31 e^{-3}	1.52 e^{-3}	1.96 e^{-4}

Table 5.4: RMSD of the measurements of Table 5.3.

The increase of lift with $AdvR$ can be reasoned by Figure 3.2 and Formula 3.4. A low pressure region is created above the disc and since it grows stronger with Ω, lift consequently increases with $AdvR$. Because p increases linearly with Ω one would expect also a linear increase of C_L. This is not verified here due to the addition of free stream velocity (which was not present in the von Kármán problem) that dominates over rotation at low $AdvR$.

Values of C_D and $C_M\ yaw$ are half of their counterparts for the full disc, confirming the symmetric contribution of each surface.

Immediately noticeable is the change of signs for both roll and pitch coefficients, occurring at the transitions from $AdvR$ = 1 to 2, and 2 to 4, respectively. This evolution is represented in Figure 5.4, with the RMSD present as error bars.

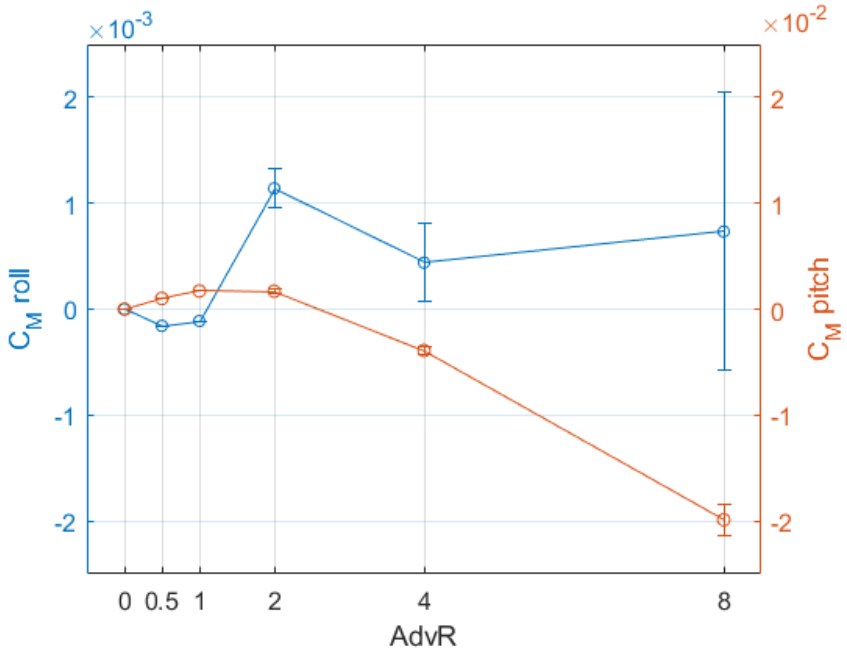

Figure 5.4: Evolution of $C_M\ roll$ and $C_M\ pitch$ for one side of the disc.

Pressure contours on the surface of the disc, represented in Figure 5.5, shed some light on this atypical behaviour.

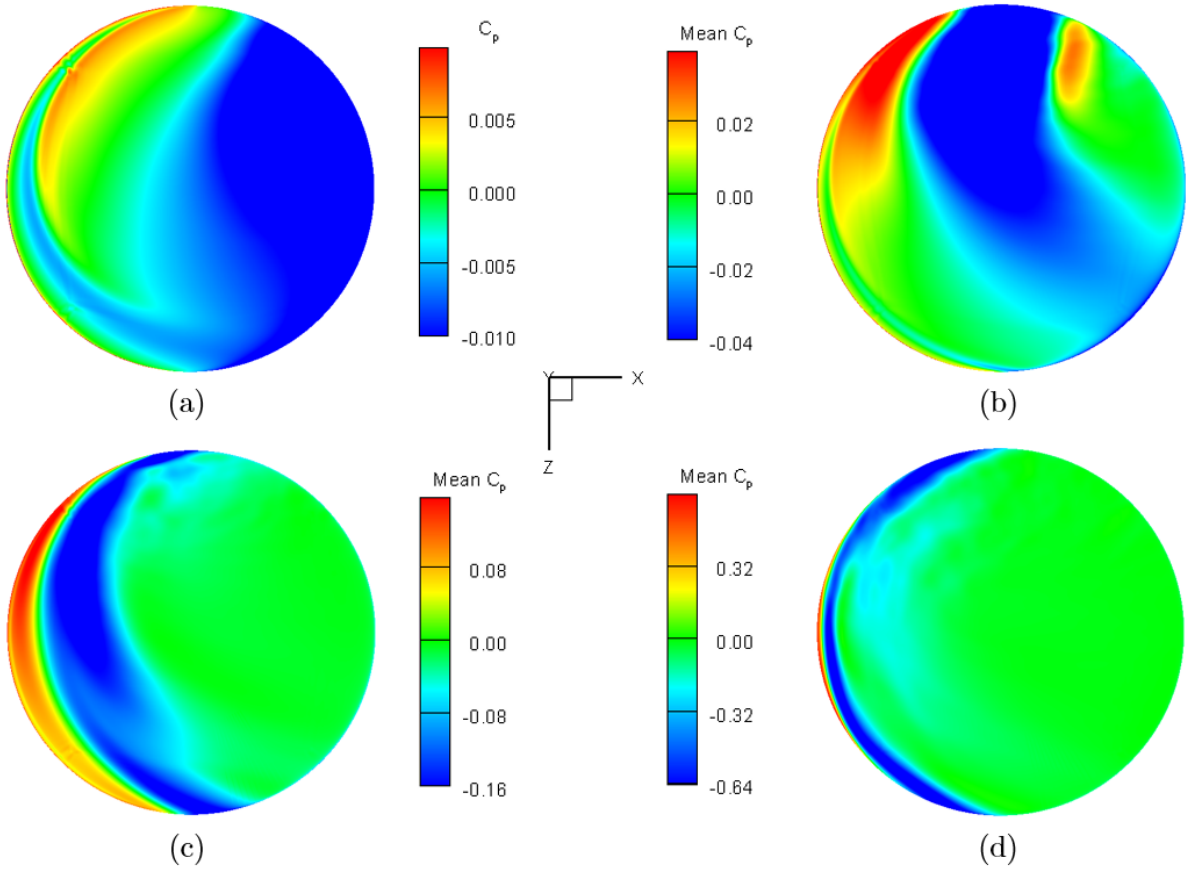

Figure 5.5: Pressure coefficient distribution for $AdvR$ = (a) 1, (b) 2, (c) 4 and (d) 8.

Rolling moment is created by differences in pressure between the left (retreating side) and right side (advancing side) of the disc since X is the roll axis. Starting from $AdvR$ = 1, the biggest low pressure region, located on the aft portion, offers an approximately equal contribution to the left and right side. The two high and low pressure areas on the front of the disc act together to produce a negative rolling moment, even though its value is fairly low. The most asymmetric pressure distribution map around the X axis, is clearly that of $AdvR$ = 2. Regions of both high and low pressure are located mainly on the advancing side. However, the lower pressure region is far bigger and more intense, causing a positive rolling motion, larger in magnitude that any other case. Cases $AdvR$ = 4 and 8 share between them a similar topology, being roughly symmetric around the X axis, which explains the sudden drop in magnitude of rolling moment, but its signal remains positive.

On the other hand, pitching moment is taken about the Z axis. It is generated when pressure imbalances arise between the front and back of the disc. For $AdvR$ = 1, two thin areas of high and low pressure are seen on the front. These seem to be of comparable magnitude, but the presence of another low pressure region, large and intense, covering most of the aft portion, bestows a nose-down, positive pitching moment. Regarding the next case, $AdvR$ = 2, both high and low pressure region have grown in strength and moved upstream. These regions work together to again produce a positive pitching moment. Its value does not change by much however, as the rise in pressure near the leading edge seems to be evened out by the migration of the low pressure area towards the front. $AdvR$ = 4 brings forth a radical change. Both regions are now located on front of the disc and the overwhelming low pressure is evident. Consequently, a nose-up, negative pitching moment is now generated, with similar magnitude as of the previous case. Finally, the same trend is noticeable for $AdvR$ = 8 but now the high pressure region is drastically reduced, as is its resistance to a nose-up motion. Therefore, a record negative pitching moment was obtained.

Since the measured coefficients are especially low, a high degree of uncertainty was noticeable in obtaining averaged values. The relatively high RMSD values from Table 5.4 corroborate this issue. However, the notorious shift in signals for rolling and pitching moments is confirmed, because for these $AdvR$, the RMSD are simply not high enough to cause erroneous signal changes.

5.4 Periodic Behaviour

A flow cycle was observed for $AdvR$ = 2, made evident by the regular, oscillatory variation of all aerodynamic coefficients. Drag, pitching and yawing moments showcased clearer cyclic characteristics however, and their behaviour can be observed in Figure 5.6.

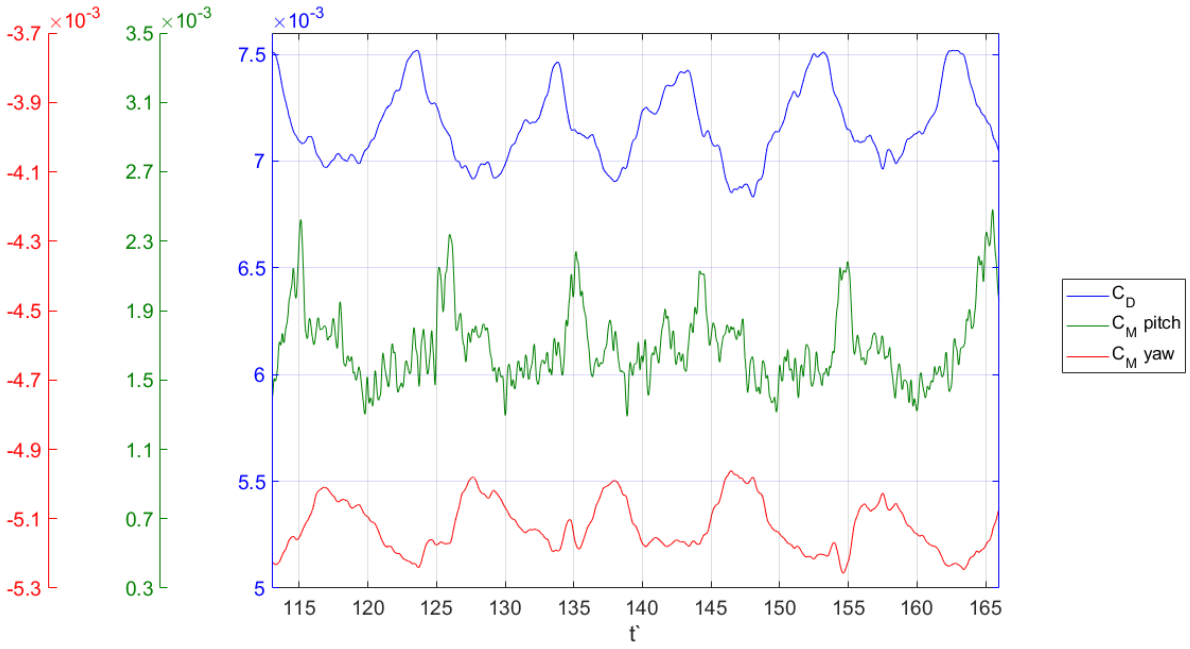

Figure 5.6: Evolution of C_D, $C_M\ pitch$ and $C_M\ yaw$ with t'.

The frequency of this established cycle f can be expressed in adimensional form as the Strouhal Number S_t given by:

$$S_t = \frac{f D_d}{U_\infty}. \tag{5.2}$$

Based on the average distance between peaks, the cycle takes about 10 t', or S_t = 0.1. This value is small enough compared to the Strouhal number linked to the disc rotation (S_t = 0.64) to confirm that this periodic phenomenon is in fact physical and not a result of spurious computational artifacts.

Comparing the Re_Ω for the onset of absolute instability from Lingwood [37] for pure rotation (510) and Re_{edge} for this case (387), the disparity is obvious. The inclusion of incoming flow seems to accelerate the appearance of instabilities, promoting early transition. Furthermore, the peak in frequency spectrum occurs at much lower frequencies ($2\pi f/\Omega$ = 0.16) than the one found by Imayama [39] ($2\pi f/\Omega$ = 30).

A periodic vortex shedding at $AdvR$ = 2 for zero incidence was also reported by Wiesche [31], for a disc with small thickness. However, a very different Re was used, and the reported S_t was higher than the one found in this study.

For $AdvR$ = 4 and 8, this cyclic behaviour disappears.

Figure 5.7 shows the power spectra of C_D, $C_M\ pitch$ and $C_M\ yaw$ for $AdvR$ = 2 and 4. These plots map out the distribution of relative power over frequency range and are a useful indicator of dominating frequencies.

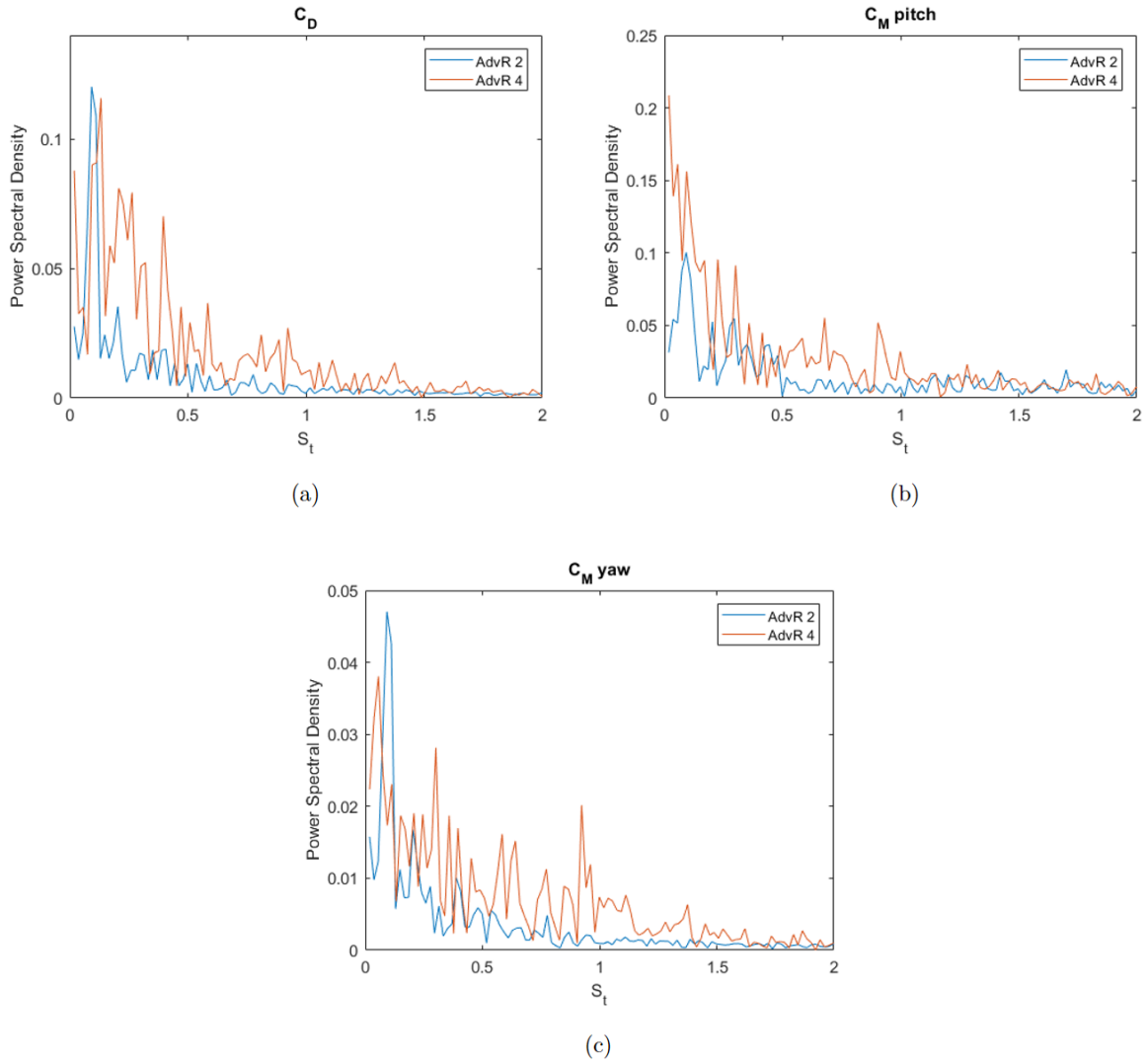

Figure 5.7: Power spectra of (a) C_D, (b) $C_M\ pitch$ and (c) $C_M\ yaw$.

For $AdvR$ = 2, the low frequency peak at S_t = 0.1 clearly towers over all others in the frequency range, thus ascertaining the periodic nature of this behaviour. This is noticeable for all 3 represented aerodynamic coefficients in Figure 5.7.

This signature is still visible for $AdvR$ = 4, particularly so for C_D. But now a plethora of other, energetically comparable components appear, partially hiding the once dominant peak. Meaning that the low frequency, periodic behaviour of $AdvR$ = 2 ceases to be noticeable.

This cycle can also be appreciated by visualizing isosurfaces of Q, colored with C_p contours. Evident in Figure 5.8 is the migration of the high pressure region to the center front of the disc and subsequent return. The shape of the low pressure area remains fairly constant however.

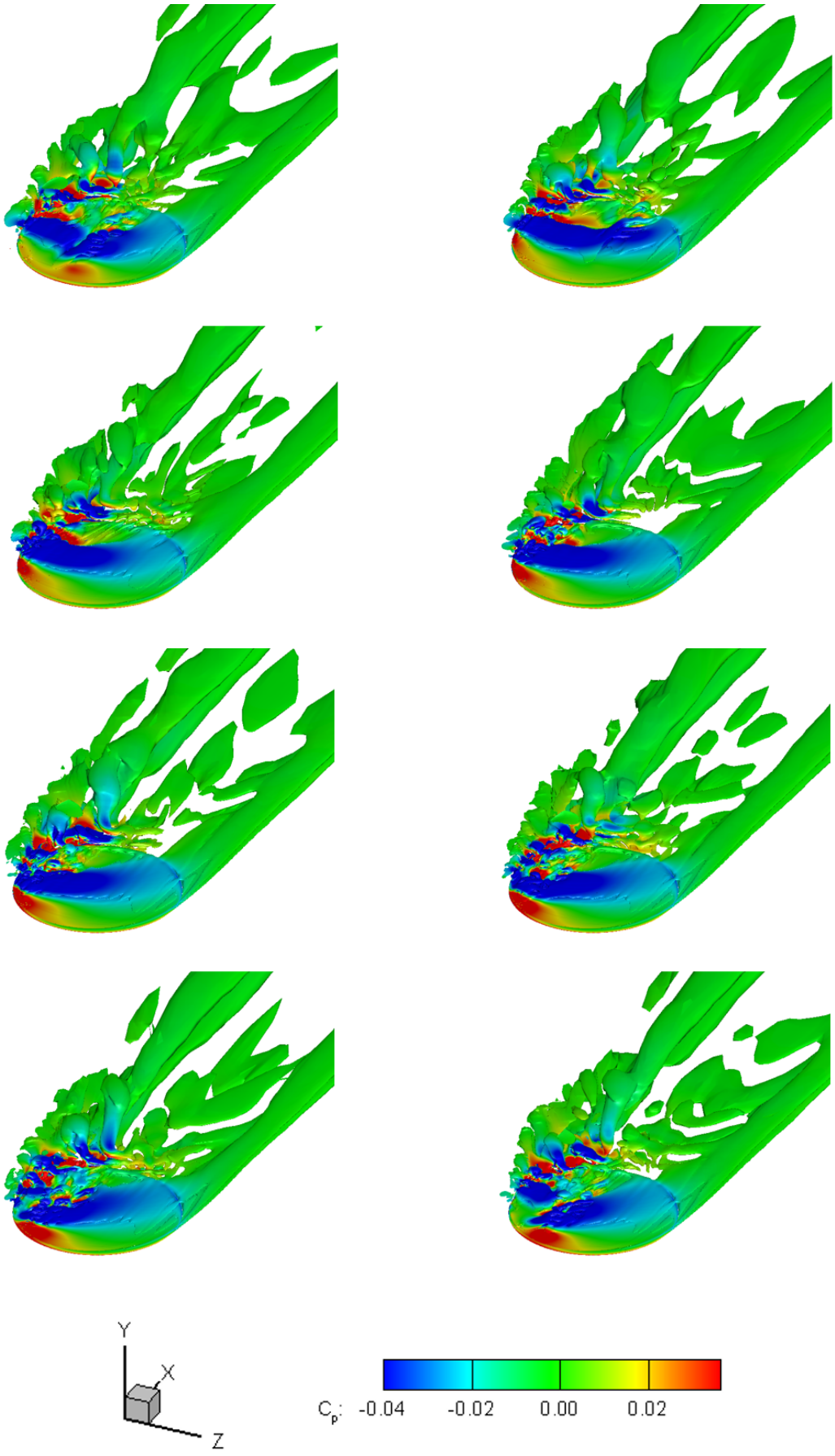

Figure 5.8: Periodic behaviour during a time interval of t‘= 10.

5.5 Limiting Streamlines

The topology of the flow close to the disc can be visualized by drawing limiting streamlines as well as skin friction lines on the surface of the disc.

Firstly, mean limiting streamlines, along with C_p contours were obtained, as in Figure 5.9.

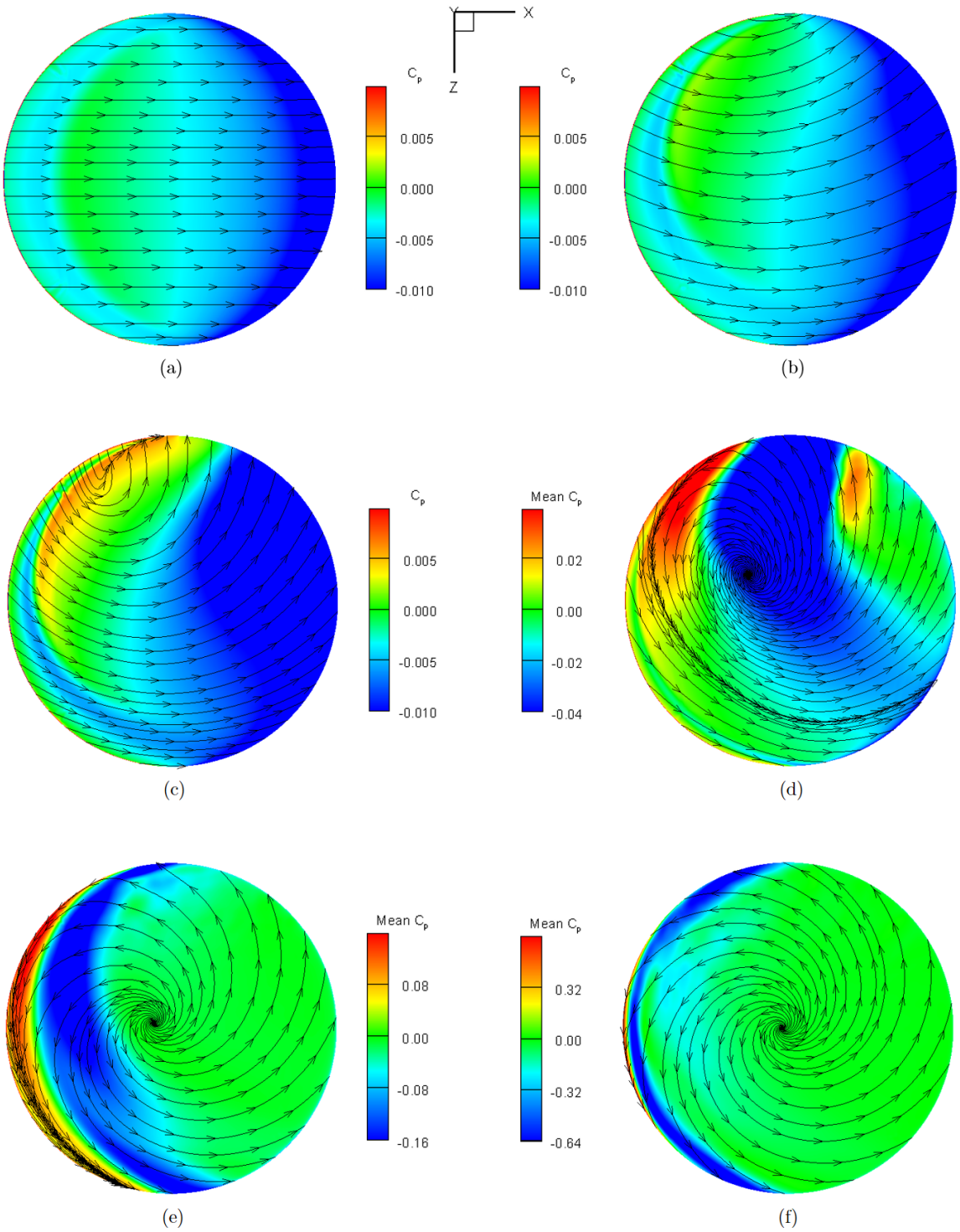

Figure 5.9: Mean limiting streamlines with contours of C_p for $AdvR$ = (a) 0, (b) 0.5, (c) 1, (d) 2, (e) 4 and (f) 8.

For zero rotation ($AdvR$ = 0) the streamlines are perfectly straight, as one would expect. With the absence of disc rotation, the particles directly on the surface showcase a horizontal trajectory, parallel to the free stream flow. As rotation is increased to $AdvR$ = 0.5, asymmetry is evident between both sides of the disc. The retreating side showcases streamlines parallel with the outer flow, while the ones on the advancing side become increasingly curved and deformed. Pressure maintains an almost equal in distribution to $AdvR$ = 0 for this low degree of rotation. For $AdvR$ = 1, the slight adverse pressure gradient causes a small separation line, made clear by the convergence of limiting streamlines. The overall lack of long and predominant separation lines in these 3 cases is consistent with the observations of few vortical structures in Figures 5.3 (a), (b) and (c).

When $AdvR$ = 2 is reached, the configuration of the limiting streamlines changes drastically. Now a focus of reattachment is visible, representing the suction of the flow due to rotation. After being drawn to the disc, the fluid particles are then expelled radially due to rotation. The overall dynamics for this $AdvR$ start to act much like the characteristic centrifugal pump of the pure rotation von Kármán problem. Additionally, the separation line migrated upstream, coincident with the adverse pressure gradient. This is logical, since rotation now exerts higher resistance against the flow on the advancing side, and thus the fluid particles separate from the surface sooner, when compared to previous cases with lower $AdvR$. The separation line remains local and small in size however, effectively dividing regions where rotation and convection by the outer flow dominate. The location of this separation line matches the appearance of vortical structures on the advancing side, in Figures 5.3 (d) and (g). Rohde [30] reported a similar separation line for $AdvR$ = 1 but on the retreating side. The fact that the tested geometry had thickness and a much higher free stream velocity was utilized (Mach = 0.5) might explain this disparity. Ultimately, $AdvR$ = 2 acts as a critical value, on which the impact brought by rotation is comparable to the convective effects of the outer flow.

Further increasing the magnitude of rotation to $AdvR$ = 4 moves the separation line to the leading edge and approximates the topology of the streamlines to that of a pure rotation problem, as the focus migrates to the center of the disc. Such a degree of rotation dominates over the effects of the free stream velocity and so much so for $AdvR$ = 8, where the flow immediately separates when confronted with rotation. This is coherent with the presence of turbulent motion on the entire surface of the disc, as Figures 5.3 (e), (f), (h) and (i) demonstrate.

Overall, after a critical $AdvR$ is reached, the effect of rotation on the periphery of the disc becomes intense enough to oppose the convective transport of the outer flow.

5.6 Skin Friction Lines

While all other flow quantities are measured relative to the inertial reference frame, the wall shear stress vector $\overrightarrow{\tau_w}$ and consequently C_f are calculated with respect to the frame rotating along with the disc, which creates an apparent disparity between limiting streamlines and skin friction lines.

This change of reference point is better understood in Figure 5.10.

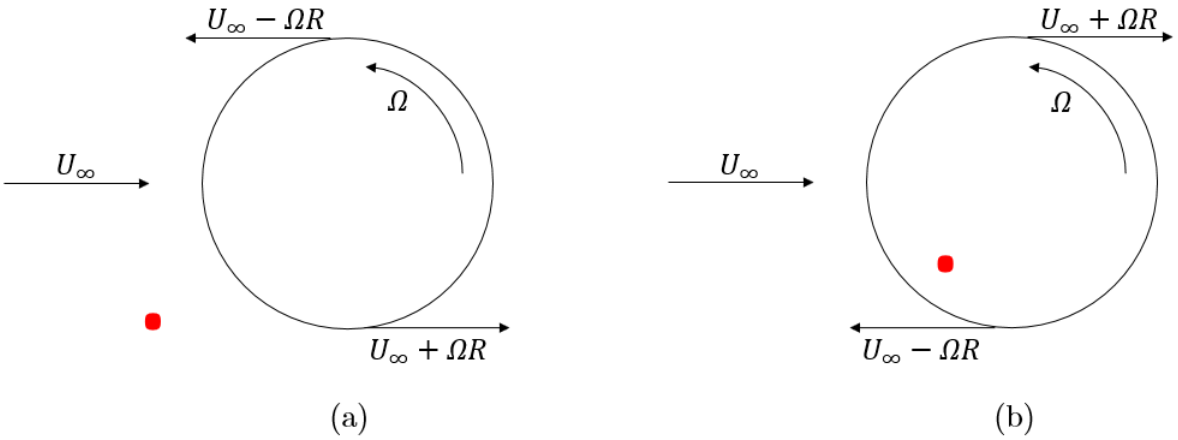

Figure 5.10: Relative velocities for a (a) fixed and (b) moving observer, represented by the red dot.

For a fixed reference frame, the incoming flow adds up with the disc rotation at the retreating side and opposes it at the advancing side, as expected. When changing to a reference frame that rotates with the disc however, the direction of rotation seems inverted. This is caused by the perception of relative velocities on the rotating frame. For an observer on the surface of the disc, the former retreating side seems to collide with the flow, and the advancing side appears to travel alongside it, effectively sensing a clockwise motion, even though the disc is rotating anti clockwise.

Since they are defined in different frames, the limiting streamlines do not tend to the skin friction lines as the distance to the wall approaches 0, like in typical flow situations without a rotating surface. Therefore, the skin friction lines representing the $\overrightarrow{\tau_w}$ components showcase a mirrored topology of the limiting streamlines previously represented. Figure 5.11 shows such skin friction lines with contours of C_f.

With added rotation, the magnitude of C_f increases due to more intense velocity gradients present at the edges of the disc. As is the case with C_p, contours of skin friction coefficient become increasingly asymmetric until $AdvR$ = 1. Beyond, the low C_f region migrates from the lower edge to the center, where, at $AdvR$ = 8, the distribution is what could be expected from a pure rotation problem. Aside from a region of high C_f near the leading edge, C_f grows from the center to the edges, attaining a radially symmetric configuration. Also, C_f is at its lowest value on the focus region for $AdvR$ = 2, 4 and 8 and shows a local minimum near the separation lines.

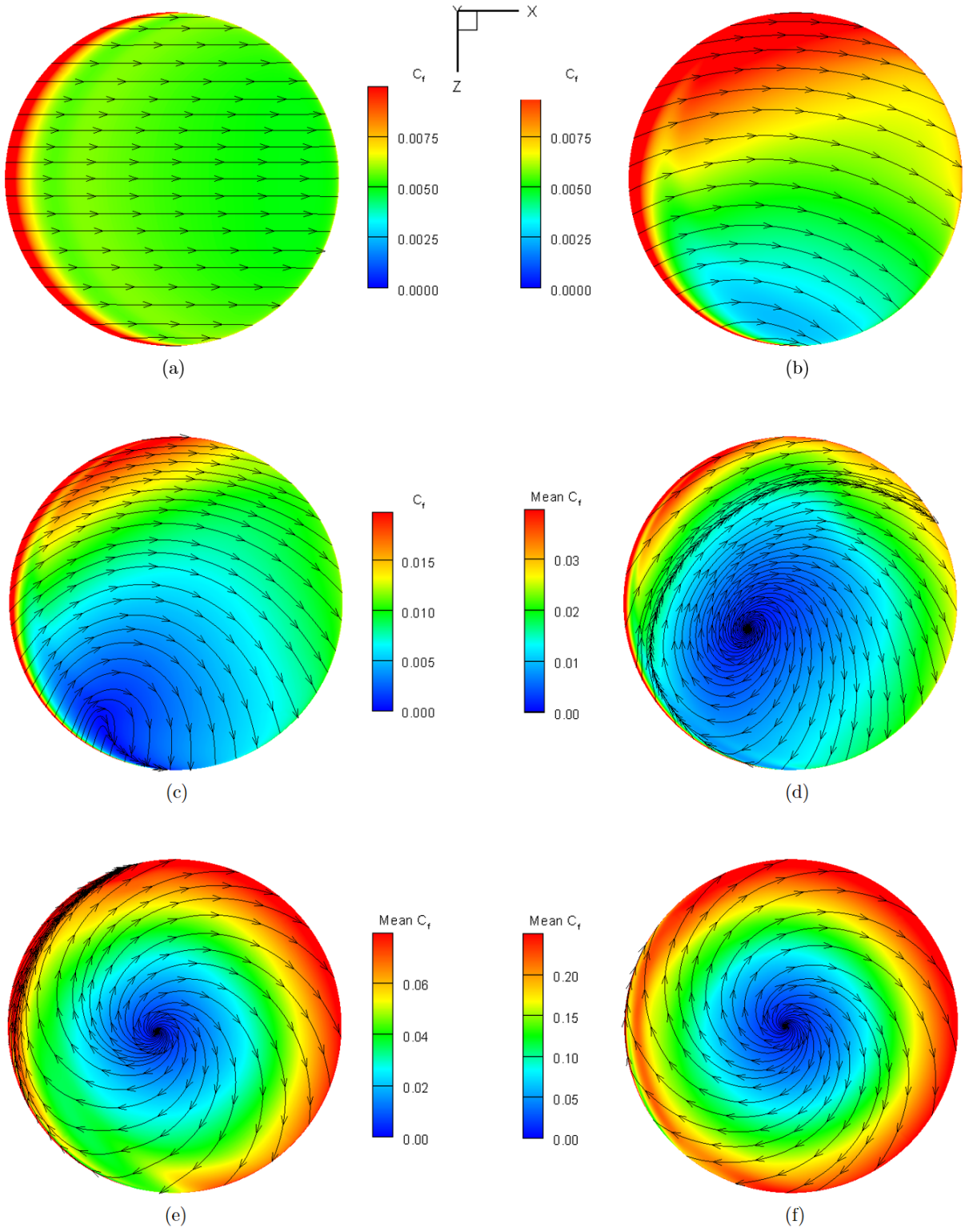

Figure 5.11: Mean skin friction lines with contours of C_f for $AdvR$ = (a) 0, (b) 0.5, (c) 1, (d) 2, (e) 4 and (f) 8.

Chapter 6

Results for α = 5°

6.1 Turbulence Kinetic Energy

Contours of adimensional turbulence kinetic energy were once again obtained on the plane Y=0. These are projected in Figure 6.1.

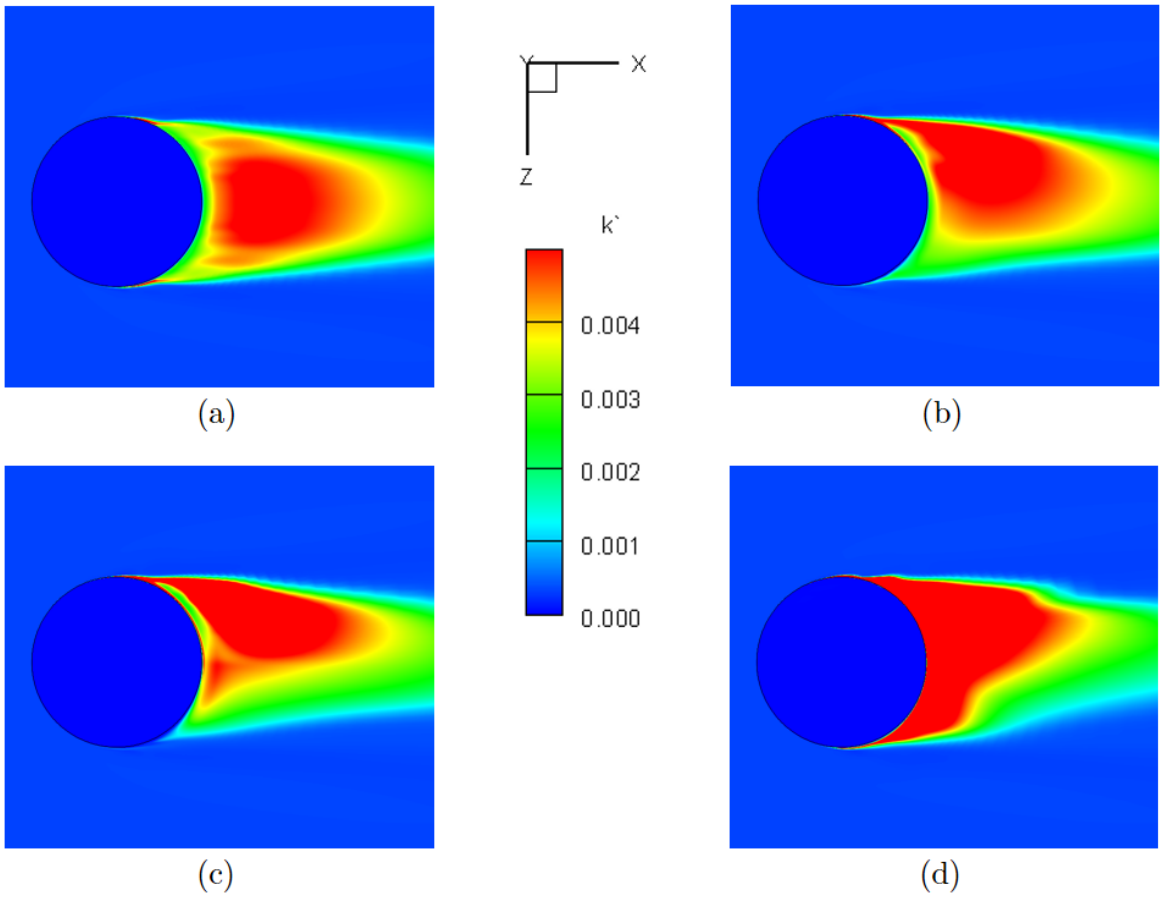

Figure 6.1: Turbulence kinetic energy distributions for $AdvR$ = (a) 0, (b) 0.5, (c) 1 and (d) 2.

When compared to Figure 5.1, $AdvR$ = 0 showcases here regions of higher turbulence intensity, justified by the presence of tip vortices, noticeable at the edges of the disc.

Overall the patterns are fairly similar, once again with accelerated transition on the advancing side and delayed on the retreating side, though this delay is not as pronounced at this angle of attack, especially so for $AdvR$ = 1 and 2. Additionally, the wake becomes thinner and more compact.

6.2 Vortical Structures

6.2.1 Top Surface

Figures 6.2 and 6.3 show instantaneous and mean isosurfaces of Q = 0.45 for the upper surface of the disc. Starting from $AdvR$ = 0, a pair of tip vortices is immediately noticeable, a typical characteristic of increasing incidence, and their presence is observed for every $AdvR$. These were confirmed by the k contours of Figure 6.1 and initially start out symmetric at $AdvR$ = 0. Until $AdvR$ = 2, the vortices preserve their size and shape, although a slight shift is noticeable, again consistent with observations from Potts and Crowther [22] and Higuchi et al. [23]. The vortex on the advancing side migrates upstream and on the retreating side, it grows in intensity. After $AdvR$ = 4, both increase in size, becoming more intense and deformed.

When compared to zero incidence in Figure 5.3, a higher density of vortical structures at low $AdvR$ (0 to 1) is evident, as the flow is now much more complex and prone to separations.

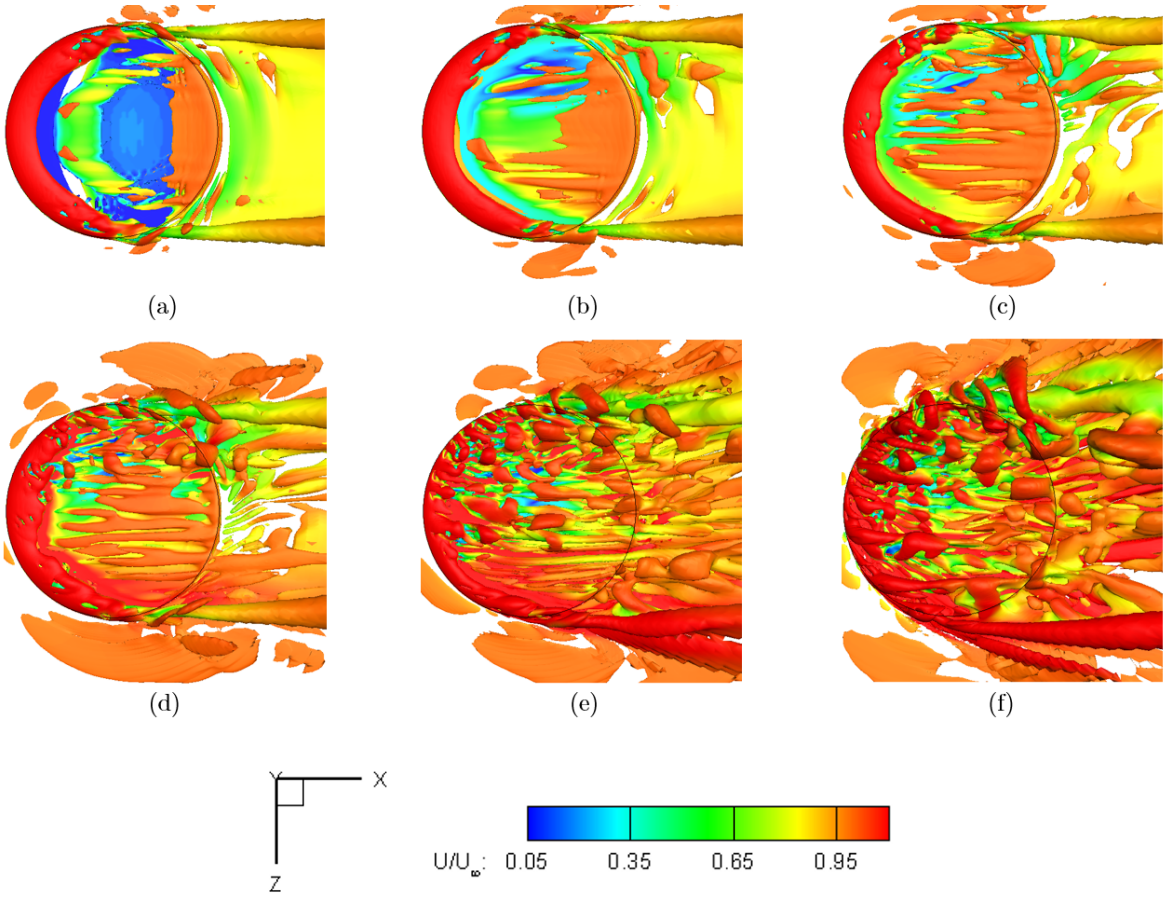

Figure 6.2: Top view of Q isosurfaces for $AdvR$ = (a) 0, (b) 0.5, (c) 1, (d) 2, (e) 4 and (f) 8.

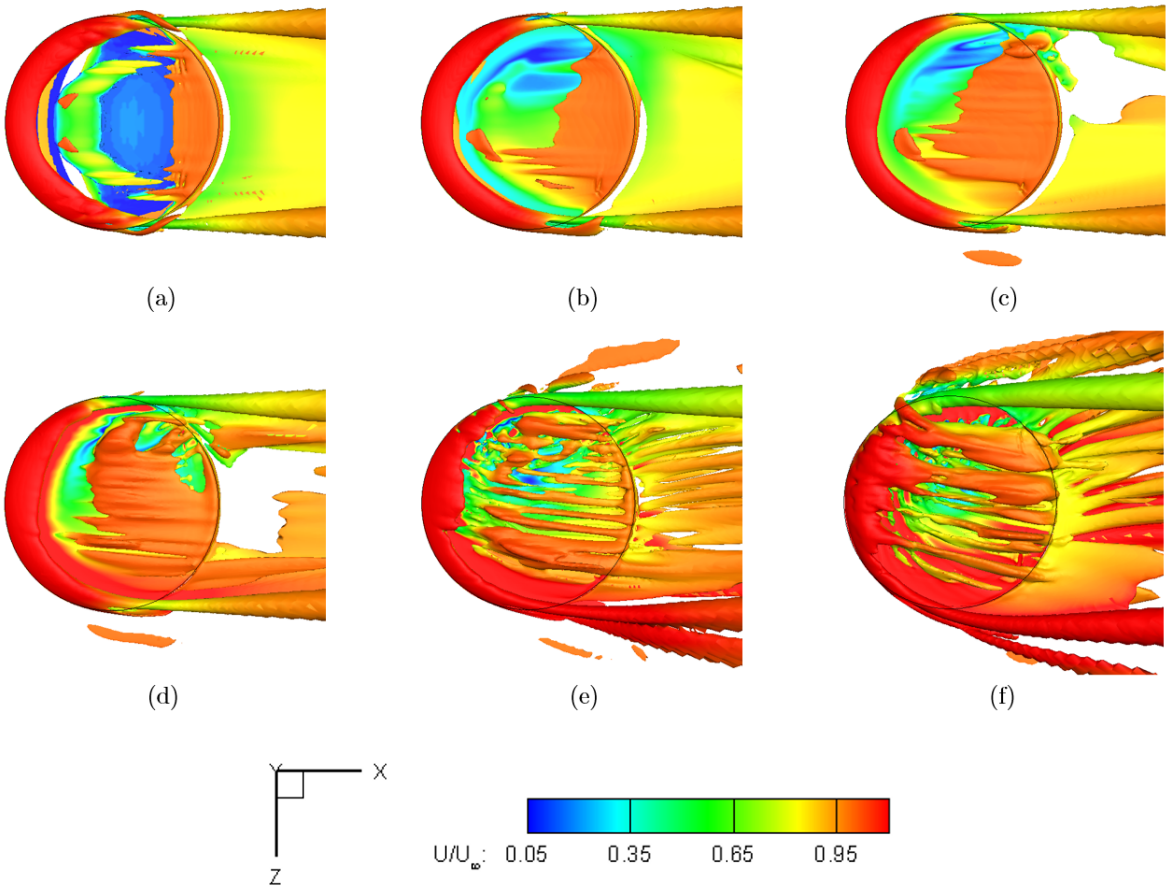

Figure 6.3: Top view of mean Q isosurfaces for $AdvR$ = (a) 0, (b) 0.5, (c) 1, (d) 2, (e) 4 and (f) 8.

Both instantaneous and mean surfaces for $AdvR$ = 4 and 8 are fairly similar to their counterparts for α = 0°, indicating that at this degree of spin, rotation dominates over the effects of increasing incidence. Aside from the tip vortices, the main differences from previous cases are the vorticity region present on the leading edge of the disc for low rotation cases and the well-defined tip vortex on the advancing side. The former is a result of laminar separation, otherwise missing for zero incidence, which will be analyzed in future sections.

6.2.2 Bottom Surface

Now analyzing the structures seen on the bottom surface in Figures 6.4 and 6.5, the decrease of turbulent structures occurring for $AdvR$ = 0, 0.5 and 1 is evident. The incoming flow comes into direct contact with this surface, delaying any separations and instabilities, thus leading to a far less complicated flow representation. There are some similarities between the present and previous cases however. Most notably, the mean isosurface for $AdvR$ = 2 (Figure 6.5 (d)) is strikingly similar to its counterpart for zero incidence (Figure 5.3 (g)). Also, the instantaneous surfaces of $AdvR$ = 8 for both α = 5° surfaces (Figures 6.2 (f) and 6.4 (f)) are rather alike. The most interesting novelties present here are the thin, much longer than previously seen structures on the retreating side for $AdvR$ = 4 and 8 (Figures 6.4 (e) and (f)), and the sharp, coherent structures, covering half of the disc, present in Figures 6.5 (e) and (f) exhibit.

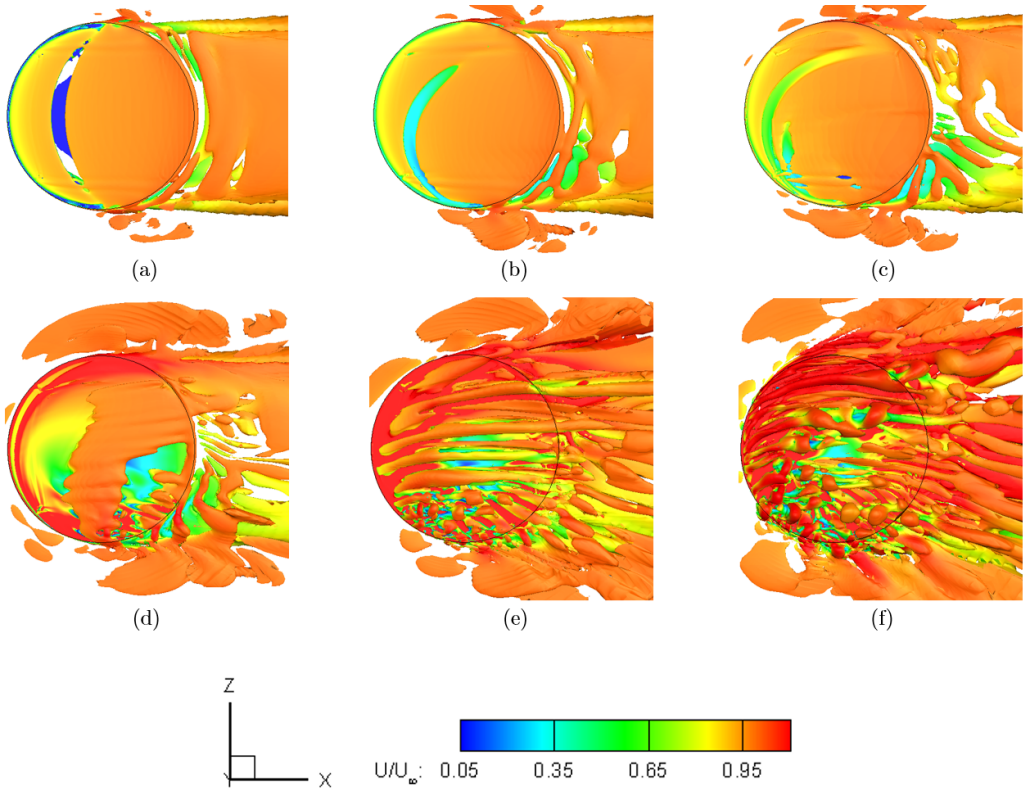

Figure 6.4: Bottom view of Q isosurfaces for $AdvR$ = (a) 0, (b) 0.5, (c) 1, (d) 2, (e) 4 and (f) 8.

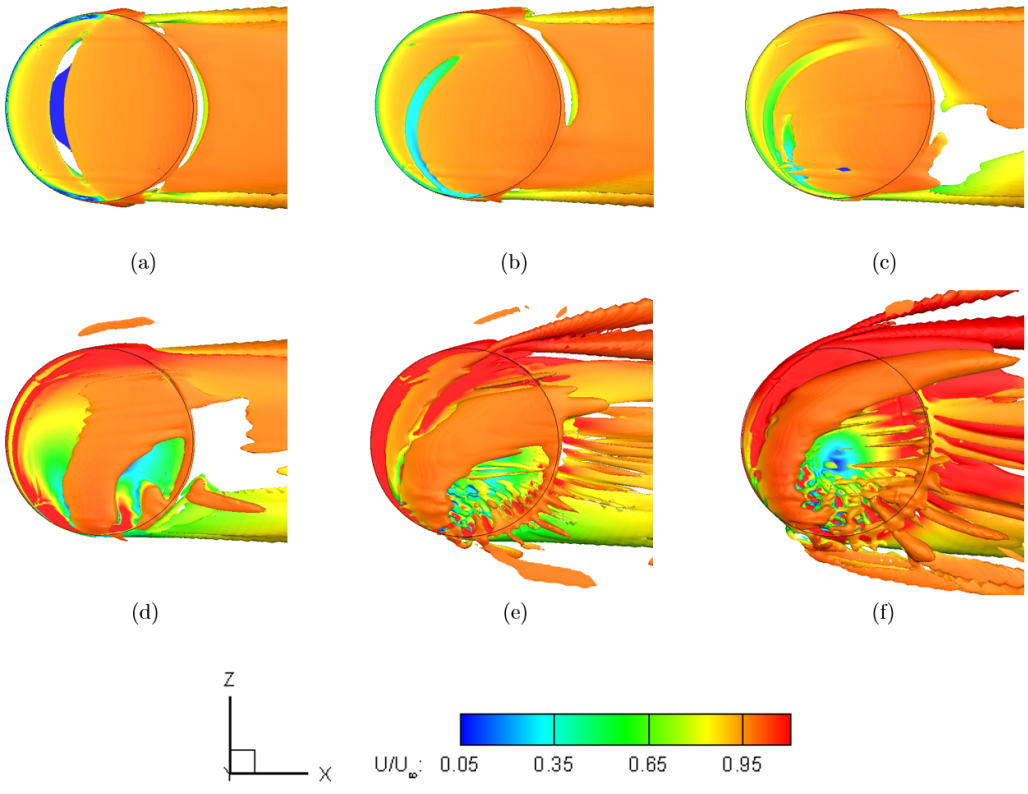

Figure 6.5: Bottom view of mean Q isosurfaces for $AdvR$ = (a) 0, (b) 0.5, (c) 1, (d) 2, (e) 4 and (f) 8.

6.3 Aerodynamic Coefficients

Now the problem ceases to be symmetric. Therefore, only the aerodynamic data regarding the full disc is of interest. Tables 6.1, 6.2 and 6.3 summarize the results.

$AdvR$	C_L	C_D	$C_M\ roll$	$C_M\ pitch$	$C_M\ yaw$
0	0.181	2.56 e^{-2}	0	-4.70 e^{-2}	0
0.5	0.181	2.60 e^{-2}	0	-4.71 e^{-2}	-2.14 e^{-3}
1	0.182	2.68 e^{-2}	-2.65 e^{-4}	-4.75 e^{-2}	-4.37 e^{-3}
2	0.183	2.81 e^{-2}	-1.48 e^{-3}	-4.75 e^{-2}	-1.01 e^{-2}
4	0.197	3.63 e^{-2}	-2.67 e^{-3}	-4.75 e^{-2}	-3.08 e^{-2}
8	0.241	4.54 e^{-2}	-2.56 e^{-3}	-5.20 e^{-2}	-0.104

Table 6.1: Mean aerodynamic coefficients for α = 5°.

$AdvR$	C_L	C_D	$C_M\ roll$	$C_M\ pitch$	$C_M\ yaw$
0	3.41 e^{-4}	7.36 e^{-6}	1.02 e^{-4}	4.83 e^{-5}	4.13 e^{-6}
0.5	5.92 e^{-4}	1.88 e^{-5}	1.99 e^{-4}	6.38 e^{-5}	7.26 e^{-6}
1	6.47 e^{-4}	3.71 e^{-5}	1.90 e^{-4}	9.79 e^{-5}	1.77 e^{-5}
2	8.15 e^{-4}	1.49 e^{-4}	2.52 e^{-4}	2.16 e^{-4}	5.01 e^{-5}
4	1.80 e^{-3}	2.71 e^{-4}	4.92 e^{-4}	5.68 e^{-4}	9.19 e^{-5}
8	6.11 e^{-3}	8.33 e^{-4}	1.72 e^{-3}	1.89 e^{-3}	2.61 e^{-4}

Table 6.2: RMSD of the measurements of Table 6.1.

$AdvR$	L/D
0	7.07
0.5	6.96
1	6.79
2	6.51
4	5.43
8	5.31

Table 6.3: Lift to drag ratio for α = 5°.

At $\alpha \neq 0°$, a certain degree of unsteadiness was observed for every $AdvR$ case.

Since the top and bottom surfaces now experience different pressure conditions, lift force will no longer be zero, as well as rolling and pitching moments. Lift stays approximately constant until $AdvR$ = 2. This trend was confirmed by the findings of Potts and Crowther [21] up to $AdvR$ = 1.04. However, when $AdvR$ = 4 is reached, C_L increases roughly 8% and after $AdvR$ = 8, a substantial increase of 22% is observed. Drag follows a similar trend than that of zero incidence, as it increases with rotation.

Interesting to note is that the case α = 0°, $AdvR$ = 8 generates less drag than the disc without rotation at α = 5°, showing just how punishing increasing incidence is. Figure 6.6 highlights the evolution of C_D for both α, with the biggest increase in drag occurring from $AdvR$ = 2 to 4 for either angle of incidence. The error bars represent again the calculated RMSD.

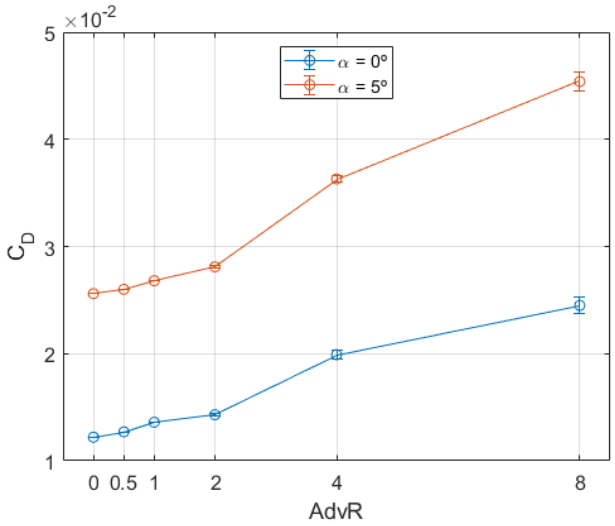

Figure 6.6: Evolution of C_D for α = 0° and α = 5°.

Additionally, Figure 6.7 shows the trends of C_L, C_D and L/D. The latter is severely worsened at $AdvR$ = 4, but at $AdvR$ = 8, the massive increase in lift almost balances the increase in drag, only leading to a small decrease of lift to drag ratio.

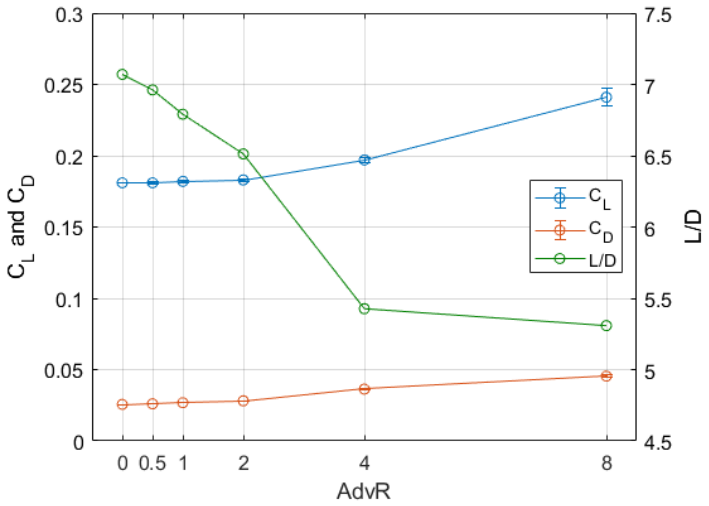

Figure 6.7: Evolution of C_D, C_L and L/D for α = 5°.

The rolling moment is always negative and increases with rotation, reaching its maximum value at $AdvR$ = 4. It plateaus thereafter. On the other hand, C_M $pitch$ stays roughly the same except a slight increase at $AdvR$ = 8. Besides, it constantly indicates a nose-up motion, predictable for non-zero incidence. Finally, the yawing moments are practically equal to those produced at zero incidence.

6.4 Limiting Streamlines

6.4.1 Top Surface

Figure 6.8 showcases the mean limiting streamlines on the top surface of the disc along with C_p contours. Starting from $AdvR$ = 0, a separation and reattachment line are immediately noticeable on the front, signaling the presence of a laminar separation bubble. Here, flow reversal towards the leading edge occurs and the fluid is convected to the sides, where it eventually joins other separation lines, representing here the tip vortices and leave the surface. Near these lines the topology of the streamlines is highly convoluted, indicating that time-average may not be the best option to determine the mean flow.

Adding rotation of $AdvR$ = 0.5 and 1 causes a shift of the LSB, much like the flow observations from Potts and Crowther [22] in Figure 2.8. The separation line on the retreating side decreases in size and is sequentially pushed downstream. On the advancing side however, it migrates upstream, to the leading edge. The regions of ill-defined streamlines near the tip vortices in Figure 6.8 (a) are much clearer now, hinting that rotation pushes the flow to the vortices more efficiently.

For $AdvR$ = 2, the separation lines on the side cease to appear, meaning that the tip vortices are not created directly on the surface, as if prevented to do so by the rotation. Also, like in Figure 5.9 (d), a reattachment focus is present. Here, rotation is strong enough to generate suction and expelling fluid particles in a centrifugal motion. The separation and reattachment line are still present, the latter emerging from the focus. This represents a complex separation pattern, similar to a tornado-like vortex, where fluid from the LSB is drawn to the disc due to rotation.

Finally, for high rotation values $AdvR$ = 4 and 8, a pure rotation topology is obtained, as in zero incidence (Figures 5.9 (f)) and thus the LSB is fully suppressed.

Focusing exclusively on the contours of pressure, the distribution barely changes up until $AdvR$ = 2. Pressure stays approximately constant on the center region of the LSB (consistent with Figure 2.5) and increases in the vicinity of the separation lines on the sides. Pressure is at its maximum near the reattachment line, as the flow reaches the surface, and minimum on the leading edge, at the beginning of the LSB. Only after $AdvR$ = 4, when the LSB is suppressed, that strong, low pressure regions start to appear. Indeed, at $AdvR$ = 8, intense negative pressure regions cover the entirety of the leading edge, strongest near the retreating side. This distribution is strikingly similar to its counterpart for $\alpha = 0°$, in Figure 5.9 (f). Also noteworthy is how the reattachment line becomes less and less coincident for $AdvR$ up to 2 with the high pressure region that outlines the end of the LSB.

6.4.2 Bottom Surface

The same distributions for the bottom surface are represented in Figure 6.9. The patterns drawn by the limiting streamlines are the same as for zero incidence, in Figure 5.9. However, C_p contours are radically different. As expected, a high pressure region occupies the front, where the flow directly contacts the surface. As rotation takes hold, this region decreases in size and migrates to the leading edge and, for $AdvR$ = 8, it shares the front with equally intense low pressure regions.

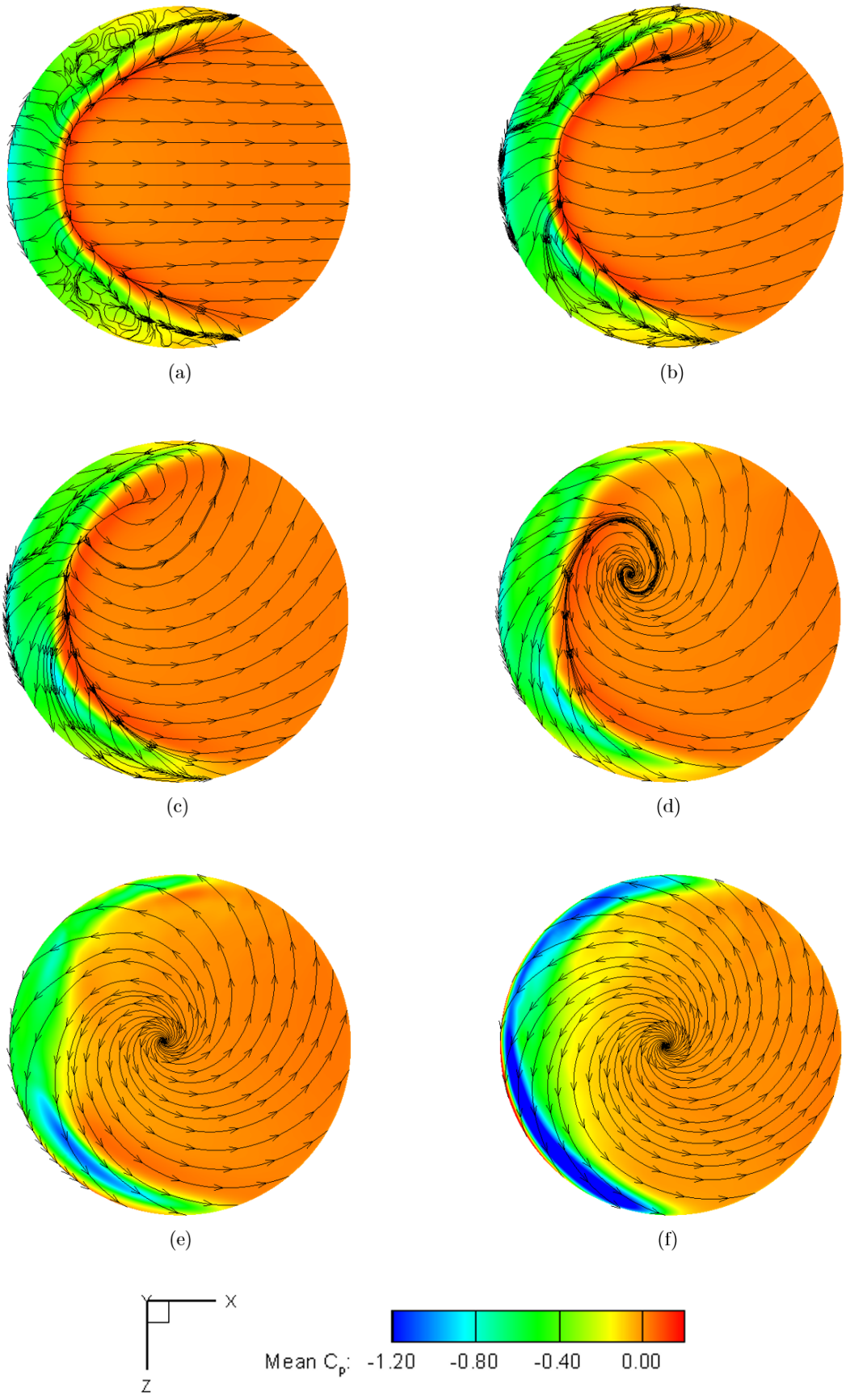

Figure 6.8: Mean limiting streamlines with contours of C_p for $AdvR$ = (a) 0, (b) 0.5, (c) 1, (d) 2, (e) 4 and (f) 8 for the top surface.

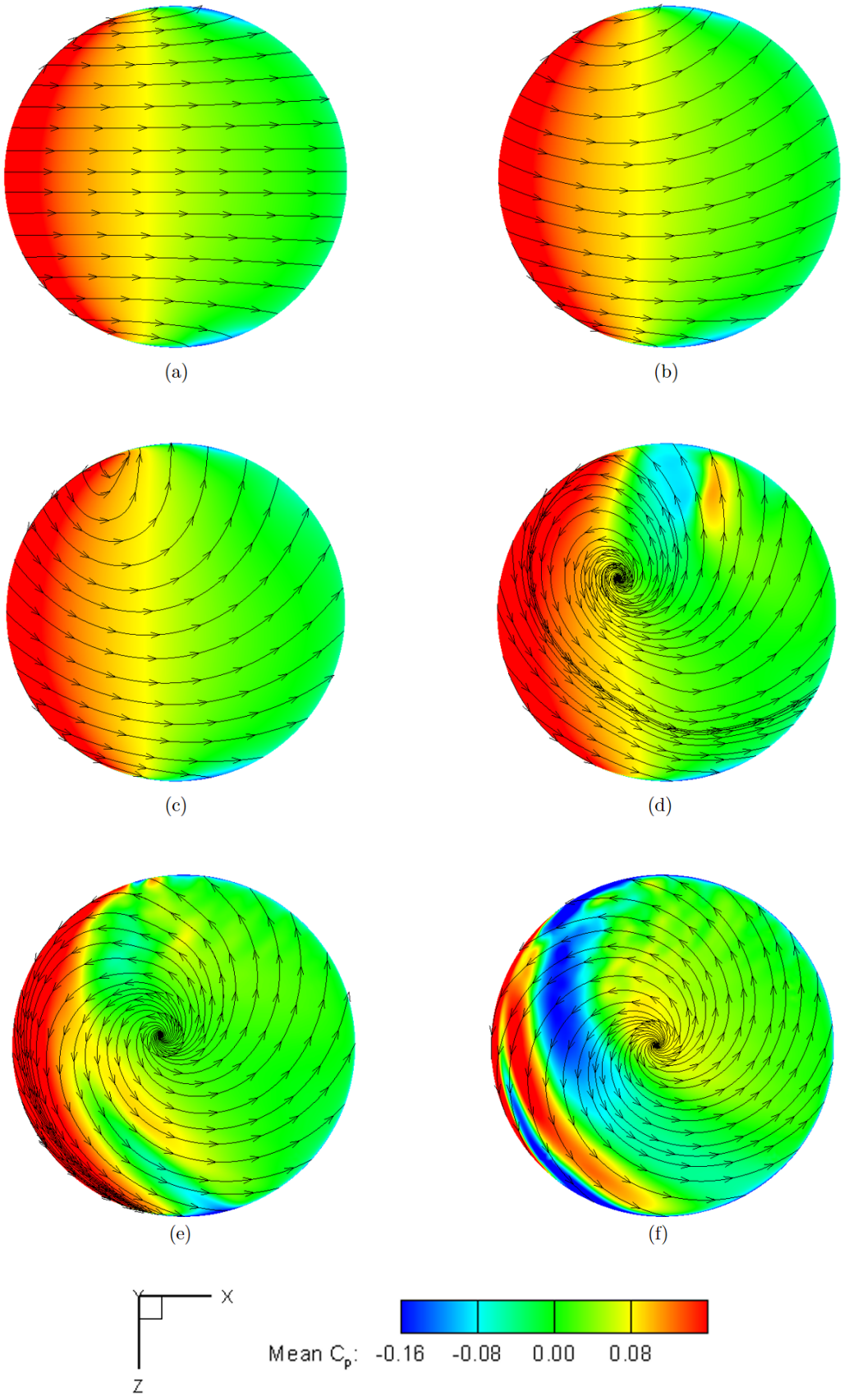

Figure 6.9: Mean limiting streamlines with contours of C_p for $AdvR$ = (a) 0, (b) 0.5, (c) 1, (d) 2, (e) 4 and (f) 8 for the bottom surface.

6.4.3 Discussion

From section 6.3 it was seen that C_L increases for $AdvR$ = 4 but the biggest improvement was from $AdvR$ = 4 to 8. A reasoning behind this evolution can be accomplished by considering the results from section 6.4.1. The pressure contours are almost equal until $AdvR$ = 4 and a LSB is evident. This is why C_L is practically constant between these cases. From Equation 3.4, low enough pressure is only created with high values of Ω. Low rotation magnitudes, coupled with the presence of the LSB, which forces a plateau of pressure, leads to virtually constant C_L values for low $AdvR$, up to 2. With increased rotation, the separation bubble is fully suppressed at $AdvR$ = 4 and a low pressure region is seen on the retreating side. Both factors cause a mild increase in lift. However, the biggest jump comes as a consequence of the intense low pressure regions, covering most of the leading edge for $AdvR$ = 8. It can be deduced that the elimination of the LSB is fundamental to achieve increase in lift for fixed incidence. This suppression not only increases lift by itself, but also allows the creation of low pressure regions on the top surface more efficiently due to rotation, further boosting C_L.

Moreover, it can be argued that the bottom surface does not play a pivotal rule in the lift evolution. At $AdvR$ = 4 and 8, low pressure regions, consequence of the high degree of rotation, are created on this surface as well, albeit with much lower dominance, which undoubtedly worsen C_L. However, at these values of $AdvR$, lift is seen to increase. As such, the biggest contribution of this lower surface is the increase in drag it brings, since its effect on lift is not determinant.

Rolling moment suffers a massive increase between $AdvR$ = 1 and 2 due to the asymmetry in pressure distribution created on the lower surface (Figure 6.9 (d)). At $AdvR$ = 4, the negative pressure on the retreating side on the top surface (Figure 6.8 (e)) leads to an increase in magnitude of $C_M\ roll$ and after that, it remains roughly constant. At $AdvR$ = 8, the contribution that the low pressure region on the retreating side for the top surface brings is opposed by a similar one on the bottom surface (Figures 6.8 (f) and 6.9 (f)). Nonetheless, a moderate high pressure region on the bottom surface near the retreating side aids the negative rolling moment. The high concentration of negative pressure on the leading edge for $AdvR$ = 8 is also responsible for the increase in pitching moment. This region and high pressure areas in the bottom surface lead to the most adverse $C_M\ pitch$ of all cases, even though negative pressure is also evident on the lower surface (Figure 6.9 (f)), which would help counteract the one on top.

Overall, high values of rotation ($AdvR$ = 4 and 8) allow for an increase in C_L, but also in C_D and $C_M\ pitch$, which undoubtedly worsen aerodynamic performance. However, for a real life disc with mass, the unstable pitching moment would be translated into a rolling moment by gyroscopic precession, as explained in section 2.1.3.

6.5 Skin Friction Lines

Figure 6.10 shows the mean skin friction lines with contours of C_f for the top surface. Until $AdvR$ = 1, a crescent-like region of high magnitude of C_f is observed between the reattachment line and tip vortices, as well as low C_f regions near the tip vortices.

After that, the focus is developed and the distributions of C_f are fairly similar to those of zero incidence (Figure 5.11). The skin friction lines and C_f maps for the bottom surface were not represented here as to avoid redundancies, since they were indistinguishable from those of Figure 5.11.

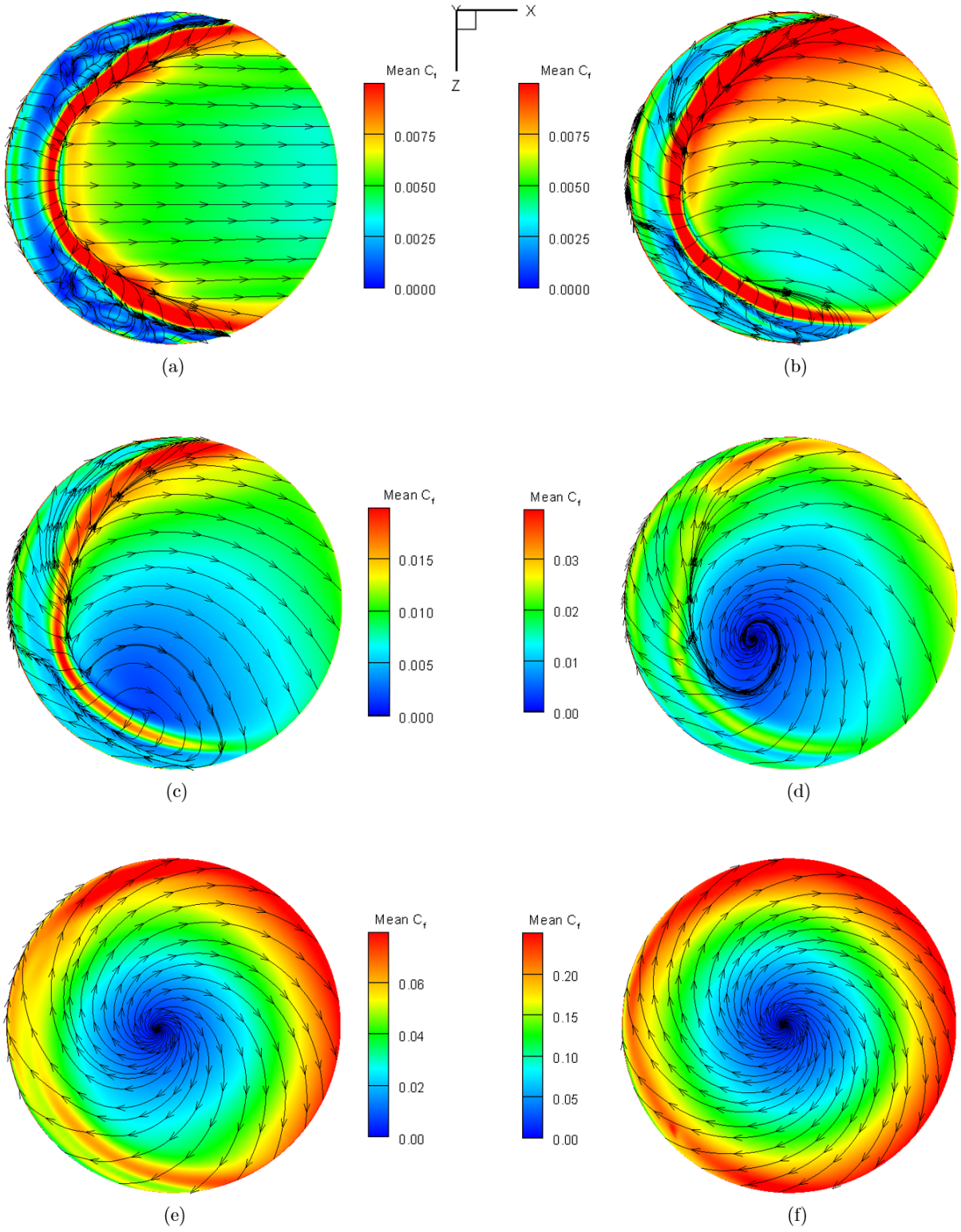

Figure 6.10: Mean skin friction lines with contours of C_f for $AdvR$ = (a) 0, (b) 0.5, (c) 1, (d) 2, (e) 4 and (f) 8 for the top surface.

6.6 Differential Rotation

Better aerodynamic performance can undoubtedly be accomplished by imposing different degrees of rotation on the top and bottom surfaces of the disc. The two simulated cases with differential rotation are listed in Table 6.4. Here, negative $AdvR$ implies clockwise rotation. This selection of $AdvR$ was carried out with the purpose of trying to maximize L/D and reduce the unstabilizing moments. Since $AdvR$ = 8 on top produced the best C_L results, only the rotation of the bottom surface was altered.

Case	Top $AdvR$	Bottom $AdvR$
1	8	0
2	8	-8

Table 6.4: The choice of $AdvR$ for differential rotation.

The aerodynamic data is summarized in Tables 6.5, 6.6 and 6.7.

Case	C_L	C_D	$C_M\ roll$	$C_M\ pitch$	$C_M\ yaw$
1	0.253	3.87 e^{-2}	-3.27 e^{-3}	-5.87 e^{-2}	-5.17 e^{-2}
2	0.239	4.76 e^{-2}	-5.32 e^{-4}	-5.74 e^{-2}	-7.21 e^{-4}

Table 6.5: Mean aerodynamic coefficients for differential rotation.

Case	C_L	C_D	$C_M\ roll$	$C_M\ pitch$	$C_M\ yaw$
1	3.21 e^{-3}	5.16 e^{-4}	9.27 e^{-4}	1.11 e^{-3}	1.94 e^{-4}
2	3.39 e^{-3}	6.48 e^{-4}	1.02 e^{-3}	1.37 e^{-3}	2.43 e^{-4}

Table 6.6: RMSD of measurements of Table 6.5.

Case	L/D
1	6.54
2	5.02

Table 6.7: Lift to drag ratio for differential rotation.

The resulting limiting streamlines and pressure contours on the top surface are the same as Figure 6.8 (f) for both cases. The bottom surface however, resulted in the same configuration as Figure 6.9 (a) for case 1, and a shifted Figure 6.9 (f) for case 2.

Lift increases for case 1, when compared to equal rotation of $AdvR$ = 8 on both surfaces (Table 6.1). Now, the bottom surface is free of any rotation and thus of induced negative pressure regions. Therefore, the negative impact that these had on C_L is gone, leading to an increase in lift production. Case 2 results in approximately equal C_L to $AdvR$ = 8 on both sides, as pressure distributions mainly shifted sides on the bottom surface.

Drag follows the opposite trend. It decreases in value for case 1, since now there is no high rotation to oppose the flow on the bottom surface. Additionally, a slight growth is noticeable for case 2. These changes bring an appreciable increase in L/D for case 1 and a modest decrease for case 2. Interesting to note is that L/D for case 1 is only slightly smaller than the one produced by $AdvR$ = 0, which shows that applying differential rotation from case 1 to achieve better C_L is well worth the consequent increase in drag. The full comparison of C_L, C_D and L/D is visualized in Figures 6.11 and 6.12. Here, the notation $AdvR$ = (a, b) translates to $AdvR$ = a on the top surface and b on the bottom one.

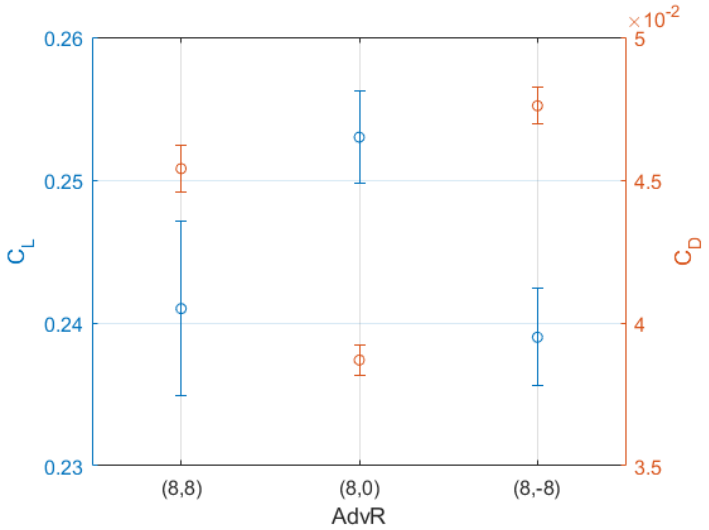

Figure 6.11: Evolution of C_L and C_D for differential rotation.

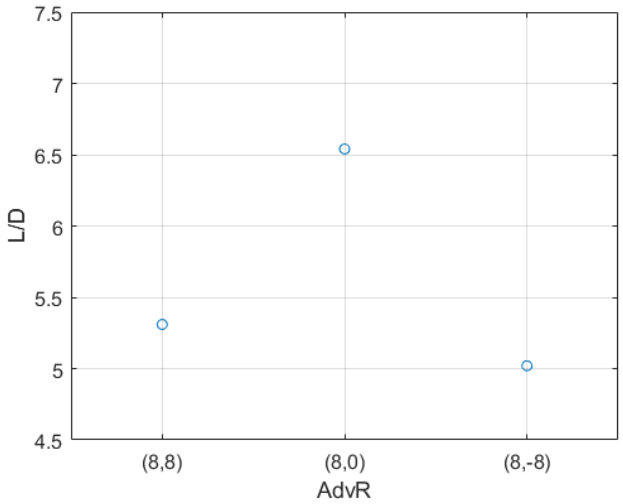

Figure 6.12: Evolution of L/D for differential rotation.

Rolling moment suffers an increase in magnitude in case 1 but is then drastically reduced for case 2. Regarding the former case, the low pressure region on the bottom surface's retreating side vanished. As such, the one on the top surface is now unopposed, resulting in a more unstabilizing C_M $roll$. For the latter case, the high pressure area on the bottom surface changes sides due to the shift in rotation direction and now counteracts the negative pressure on top (Figure 6.13), stabilizing the disc.

Pitch always seems to slightly deteriorate. Due to the lack of low pressure regions on the leading edge for the bottom surface, pitching moment increases in magnitude for case 1. Similarly, $C_M\ pitch$ grows more unstable for case 2. This can be visualized in Figure 6.13. A slight superiority of the high pressure region on the front of the disc for the differential rotation is observed, creating an increase in pitching moment.

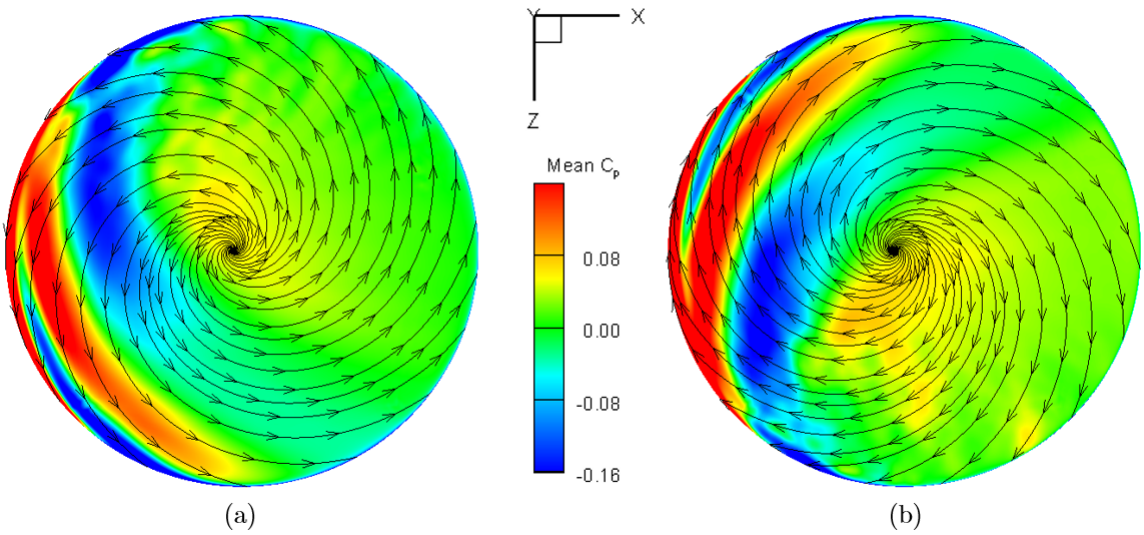

Figure 6.13: Mean limiting streamlines with contours of C_p of (a) Figure 6.9 (f) and (b) differential rotation case 2 for the bottom surface.

Figure 6.14 highlights the changes in rolling and pitching moments.

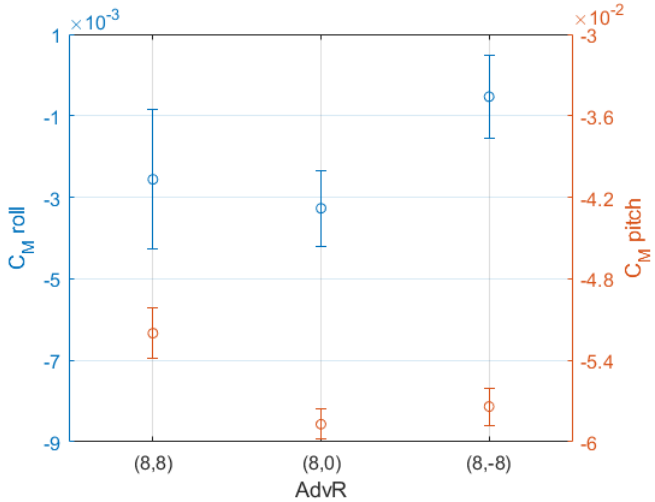

Figure 6.14: Evolution of $C_M\ roll$ and $C_M\ pitch$ for differential rotation.

Finally, yawing moments showcase predictable results. Case 1 produces half of $C_M\ yaw$ for equal rotation and case 2 roughly null moment.

Each differential rotation case is best suited for separate goals. Case 1 is apt at increasing L/D and case 2 at minimizing the rolling moment. The latter becomes particularly useful when remembering that in a real life scenario, gyroscopic precession will occur, and added rolling moment will be induced.

Chapter 7

Results for α = 10°

7.1 Turbulence Kinetic Energy

Figure 7.1 shows the k distribution on the plane Y = 0.

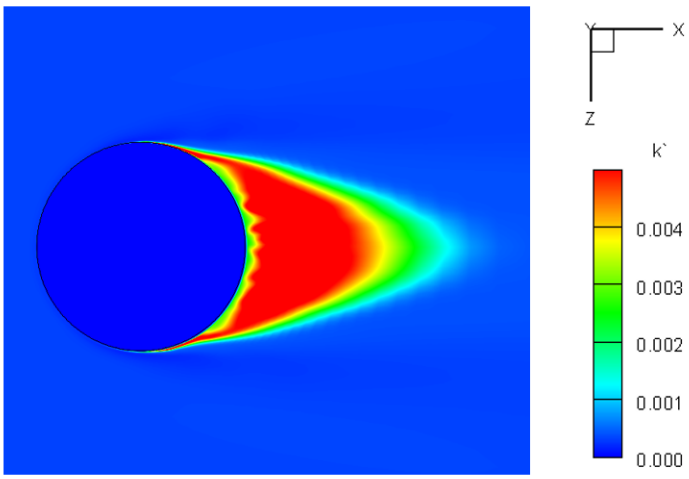

Figure 7.1: Turbulence kinetic energy distribution for $AdvR$ = 0.

The magnitude of k is now more pronounced than Figures 5.1 (a) and 6.1 (a), particularly so near the tips and trailing edge. The wake is much narrower in width due to higher convection happening on the direction of the flow.

7.2 Vortical Structures

As Figures 7.2 (a) and (c) show, much more vortical structures are identified by the Q criterion around and especially on the disc. Here, the return of hairpin-like vortices is noticeable. With added inclination, stronger pressure gradients will be created on the surface of the disc, thus resulting in more intricate turbulent structures.

The tip vortices are now much thicker and form slightly more upstream. Moreover, the region of vorticity identified right on the leading edge is larger than the one found on Figure 6.3 (a). Figure 7.2 (b) now displays longitudinal and stretched vortices on the disc, which only appeared when high degree of rotation was applied for α of 0° and 5°.

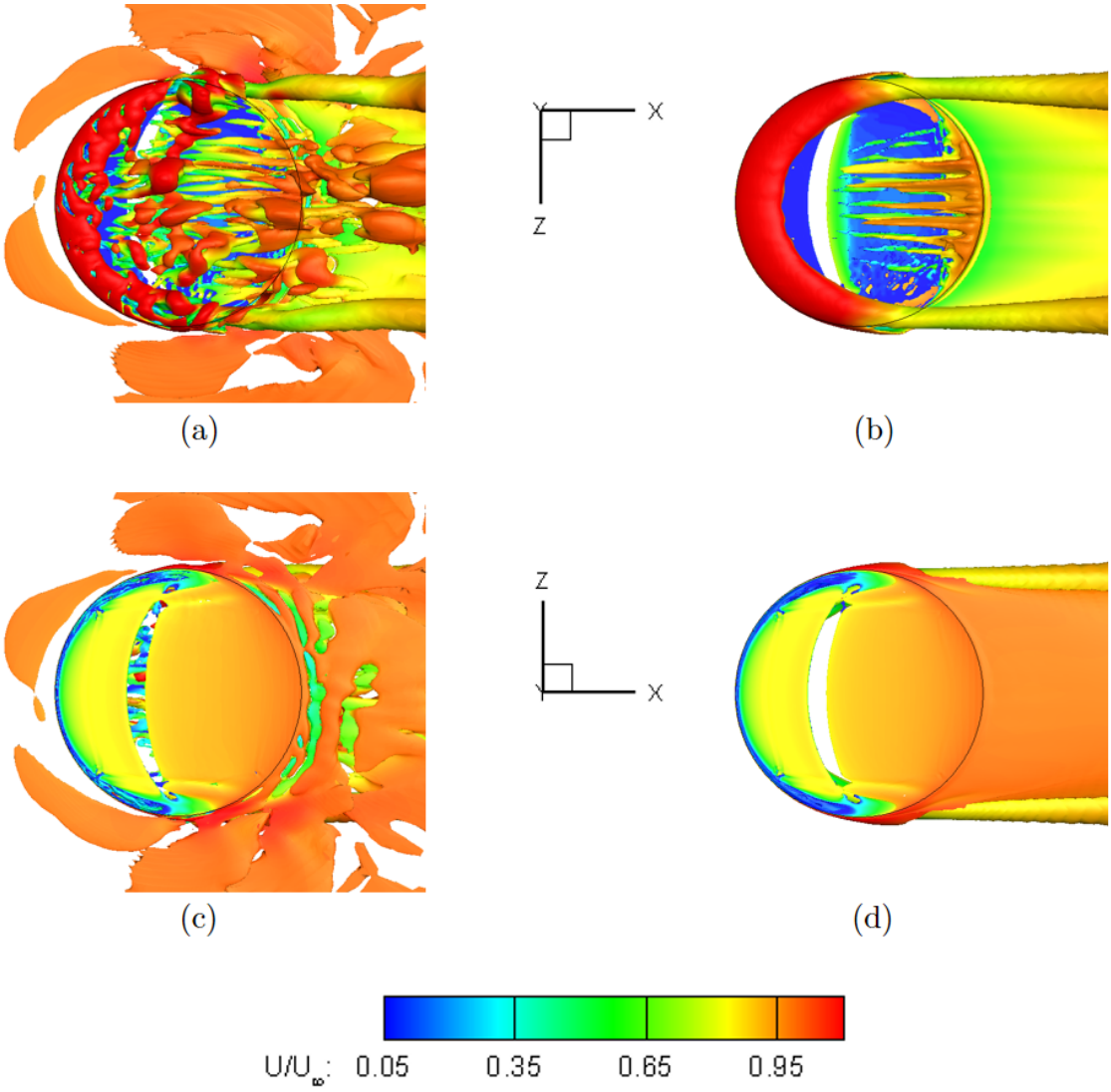

Figure 7.2: Top surface's (a) instantaneous and (b) mean Q isosurfaces. Bottom surface's (c) instant and (d) mean Q isosurfaces.

7.3 Aerodynamic Coefficients

Tables 7.1, 7.2 and 7.3 show the results regarding aerodynamic figures. The lift coefficient increases massively, as well as C_D when compared to values from Table 6.1, a typical trend for higher incidence. However, the overall balance results in a decidedly worse lift over drag ratio. Pitching moment also increases, due to the higher and lower pressure present at the bottom and top surface, respectively.

$AdvR$	C_L	C_D	$C_M\ roll$	$C_M\ pitch$	$C_M\ yaw$
0	0.397	7.83 e^{-2}	0	-9.66 e^{-2}	0

Table 7.1: Mean aerodynamic coefficients for α = 10°.

$AdvR$	C_L	C_D	$C_M\ roll$	$C_M\ pitch$	$C_M\ yaw$
0	2.93 e^{-3}	1.53 e^{-4}	9.20 e^{-4}	6.41 e^{-4}	3.28 e^{-5}

Table 7.2: RMSD of measurements of Table 7.1.

$AdvR$	L/D
0	5.07

Table 7.3: Lift to drag ratio for α = 10°.

Validation with previous studies

The full range of aerodynamic coefficients for a non-rotating disc ($AdvR$ = 0) is summarized in Table 7.4.

α [°]	C_L	C_D	L/D	$C_M\ roll$	$C_M\ pitch$	$C_M\ yaw$
0	0	1.22 e^{-2}	0	0	0	0
5	0.181	2.56 e^{-2}	7.07	0	-4.70 e^{-2}	0
10	0.397	7.83 e^{-2}	5.07	0	-9.66 e^{-2}	0

Table 7.4: Mean aerodynamic coefficients for $AdvR$ = 0.

These can be compared to corresponding data from Torres and Mueller [18] and Kamaruddin [19]. For the former, results from an elliptic wing model with AR = 1.25 are used for comparison. This aspect ratio is sufficiently close to the one characteristic of the disc geometry, focus of this study (1.273). Regarding the latter, validation can be carried out by considering aerodynamic results from the thinnest disc geometry. The sign conventions from this study and Kamaruddin [19]'s are opposite for the pitching axis. To perform validation, the obtained $C_M\ pitch$ values from this study were made positive. Additionally, the Re of these experimental studies are not the same as the one utilized in the present study. However, Torres and Mueller [18] remarked that at such low Re, the effect of varying this variable on aerodynamic data at low α can be considered negligible.

This comparison can be seen in Figures 7.3, 7.4, 7.5 and 7.6. All compared values from Table 7.4 agree exceptionally well with the previous studies. Obtained magnitudes of drag were slightly smaller for the present study since the disc had no thickness.

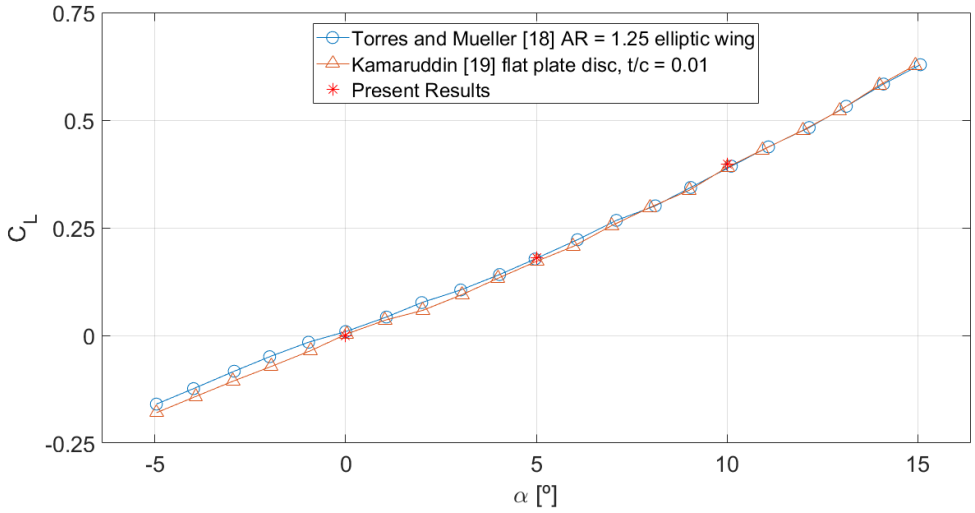

Figure 7.3: Comparison of obtained C_L values with previous experimental studies.

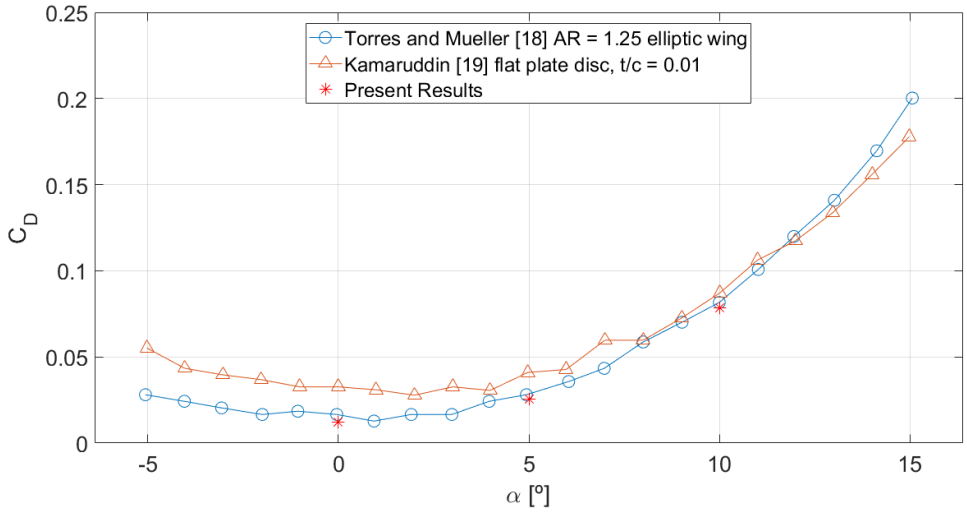

Figure 7.4: Comparison of obtained C_D values with previous experimental studies.

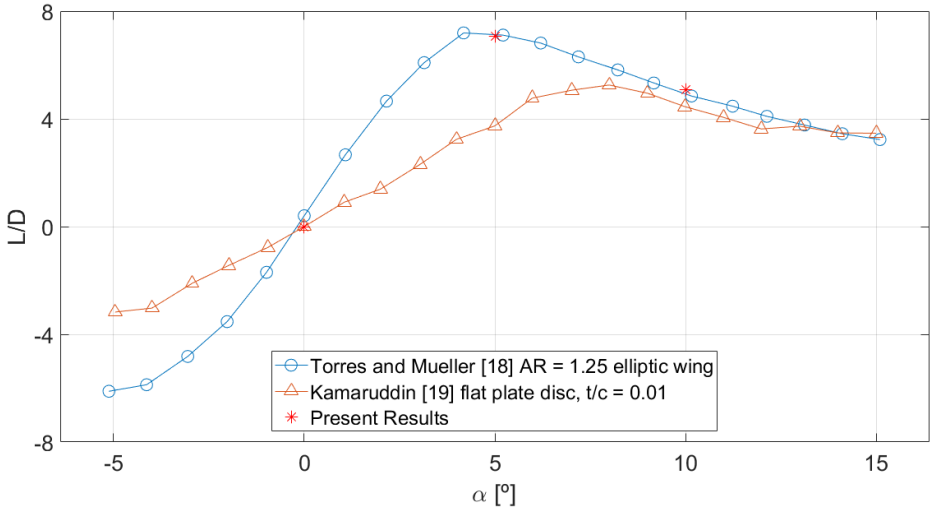

Figure 7.5: Comparison of obtained L/D values with previous experimental studies.

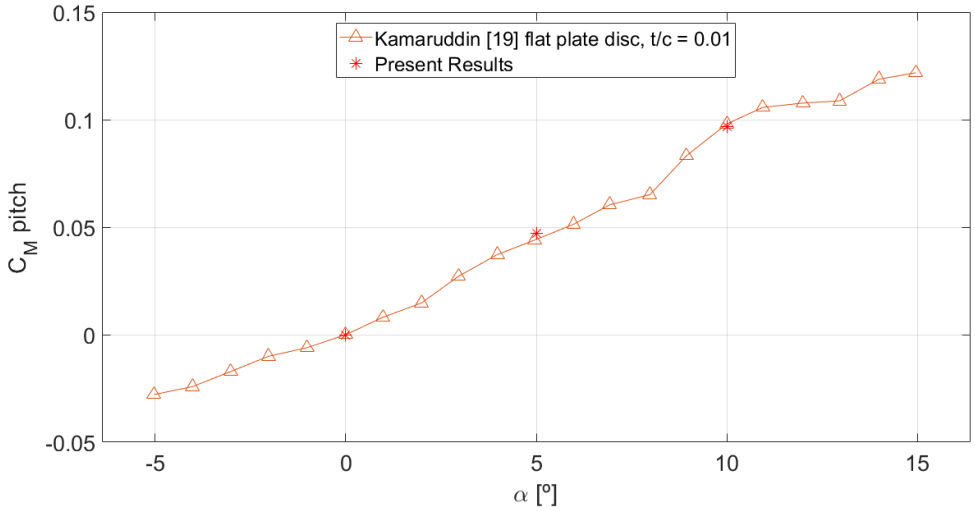

Figure 7.6: Comparison of obtained C_M $pitch$ values with previous experimental studies.

7.4 Limiting Streamlines

Figure 7.7 showcases mean limiting streamlines with contours of C_p for both surfaces of the disc.

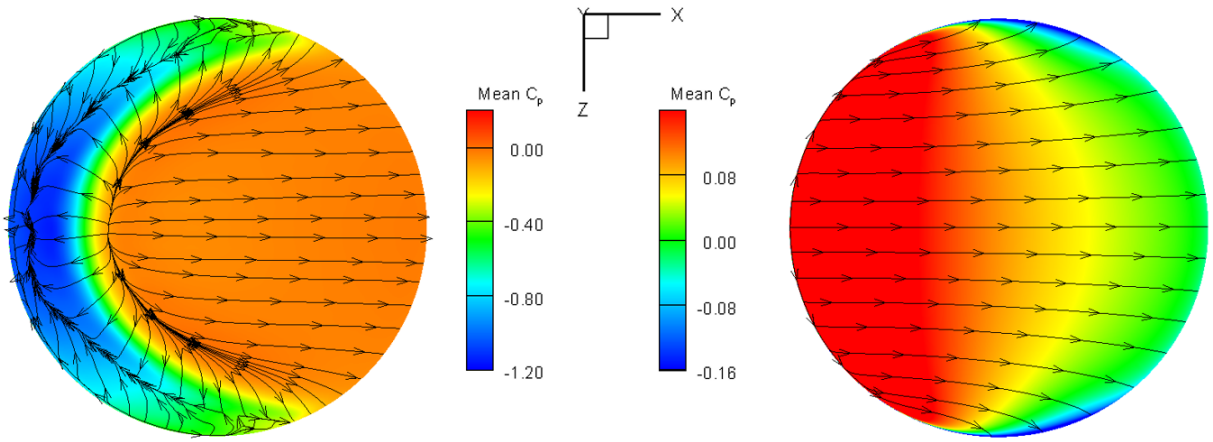

Figure 7.7: Mean limiting streamlines with contours of C_p for the (a) top and (b) bottom surface.

When compared to Figure 6.8 (a), two main differences are immediately noticeable. Firstly, the convoluted streamlines near the tip vortices are now well-defined and represent a clearer pattern. Secondly, the two separation lines representing the tip vortices now unite in one long separation, that is present near the leading edge, and an additional reattachment line is observed. By projecting the velocity vectors onto a XY plane, as in Figure 7.8, a second, smaller separation bubble is seen. It is encapsulated by the bigger one and is responsible for the appearance of the new lines. Apparently, this new phenomenon existed in its primordial form at α = 5° and is now fully developed.

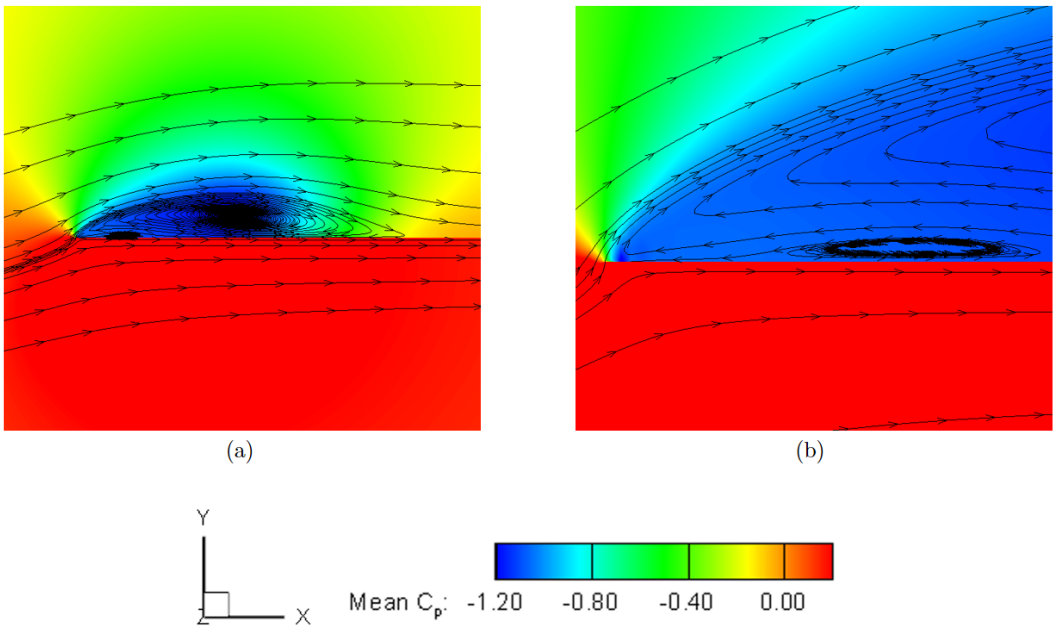

Figure 7.8: (a) Projected streamlines onto a Z=0 plane with contours of C_p and (b) zoomed in.

Also, the original LSB increases in size, as the reattachment line signaling that the end of the bubble moves downstream. This expansion with α was noted by Higuchi et al. [23] for the disc's upper surface, and the resulting topology of streamlines on Figure 7.7 (a) is strikingly similar to the one reported on the same study, for the same angle of attack. Pressure magnitude exhibits more intense values near the leading edge, a clear consequence of increased incidence.

7.5 Skin Friction Lines

The resulting C_f distribution from Figure 7.9 follows the same trend as expected. The same crescent region of high magnitude is still visible, although slightly larger.

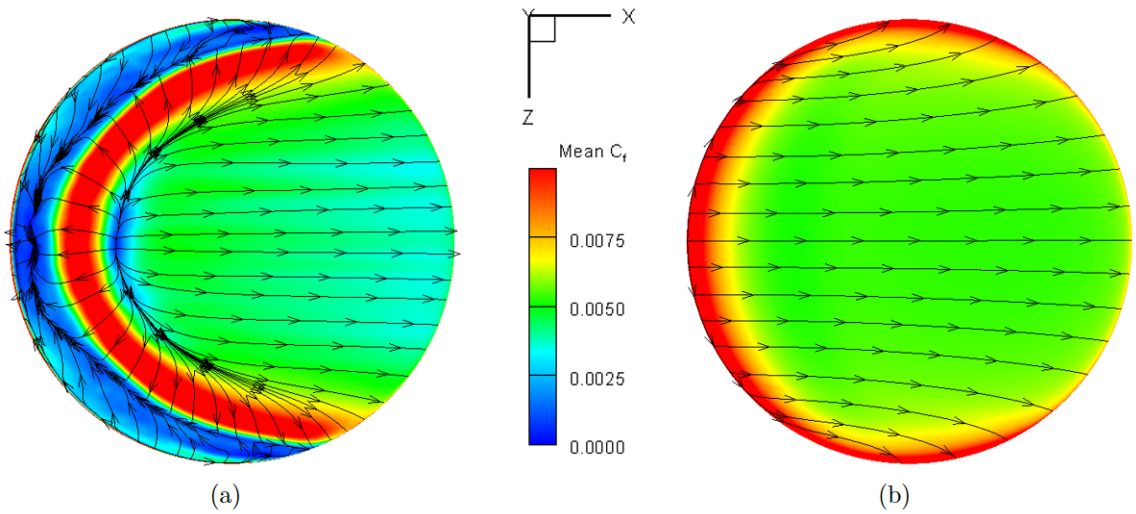

Figure 7.9: Mean skin friction lines with contours of C_f for the (a) top and (b) bottom surface.

7.6 Differential Rotation

Previously, case 1 from Table 6.4 yielded the best C_L results and also a vast improvement in terms of L/D over the standard $AdvR$ = 8, with a faint decrease over the $AdvR$ = 0 case. Now, this differential rotation is applied to α = 10° to observe the evolution in aerodynamic results (Tables 7.5, 7.6 and 7.7).

Case	C_L	C_D	C_M $roll$	C_M $pitch$	C_M yaw
1	0.479	9.89 e^{-2}	-3.37 e^{-3}	-0.108	-5.24 e^{-2}

Table 7.5: Mean aerodynamic coefficients for differential rotation.

Case	C_L	C_D	C_M $roll$	C_M $pitch$	C_M yaw
1	5.08 e^{-3}	9.75 e^{-4}	1.29 e^{-3}	1.73 e^{-3}	2.00 e^{-4}

Table 7.6: RMSD of the measurements of Table 7.5.

Case	L/D
1	4.84

Table 7.7: Lift to drag ratio for differential rotation.

Values of C_L, C_D and C_M $pitch$ all increase in magnitude, when compared to the results from Table 7.1. Again, L/D suffered only a slight decrease from $AdvR$ = 0. Interesting to note is that C_M $roll$ is roughly the same as for α = 5°, case 1, leading to the conclusion that the larger pressure gradients produced here on both surfaces balance each other similarly. At α = 5°, case 1 resulted in a lift increase of approximately 40%, when compared to the case without rotation. Here, this growth is smaller: 21%. However the separation bubble was also fully suppressed here, as Figure 7.10 shows. One can conclude that $AdvR$ = 8 rotation is still dominant enough to eliminate the now larger separation bubble and to generate a vast improvement in C_L over the disc without rotation, like for α = 5°.

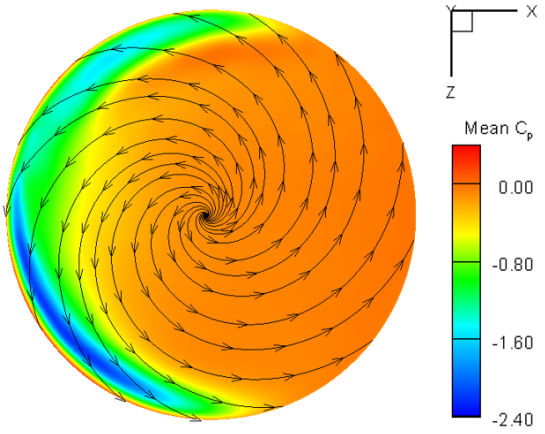

Figure 7.10: Mean limiting streamlines with contours of C_p of differential rotation case 1 for the top surface.

Chapter 8

Conclusions

8.1 Achievements

In this thesis, flow around an inclined, rotating disc at Re = 150,000 was studied by means of CFD simulations, with IDDES as the selected mathematical model to model turbulence. The disc geometry had no thickness and different magnitudes of rotation were applied, from $AdvR$ = 0 to 8. Here, $AdvR$ is defined as the ratio between tip and flow speed. Additionally, the disc was immersed in free stream flow at three distinct angles of attack (0°, 5° and 10°). Aerodynamic coefficients, limiting streamlines and vortical structures were calculated and further validated by comparison to previous studies.

The main findings of the present study are as follows:

- **From chapter 5**, delayed and accelerated transition on the retreating and advancing side, respectively, were observed. Hairpin-like vortices on the surface of the disc appeared for $AdvR$ = 4 and 8. Furthermore, the rolling moment measured on one surface of the disc was shown to shift signals, converting from negative to positive values between $AdvR$ = 1 and 2. Similarly, the pitching moment changes from positive to negative between $AdvR$ = 2 and 4. These swaps were explained by pressure contours on the disc. A periodic behaviour was noted at $AdvR$ = 2. The measured oscillations showed a distinct peak in power spectra graphics at S_t = 0.1. From the topology of mean limiting streamlines, a small separation line was first seen for $AdvR$ = 1 on the advancing side, which travels further upstream until it is no longer present on the disc at $AdvR$ = 8. At this degree of rotation, the resulting mean limiting streamlines and C_f distribution are almost identical to those of a rotation-only problem. The same streamlines displayed the formation of a reattachment focus past $AdvR$ = 2, signaling the threshold beyond which rotation is strong enough to draw fluid onto the surface;
- **From chapter 6**, tip vortices for $AdvR$ = 0 were observed as was their growth and deformation with added rotation. Vortical structures on the top and bottom surface were compared. Lift was shown to be roughly constant up until $AdvR$ = 2. The presence of a laminar separation bubble on the top surface and low Ω magnitudes cause this plateau. At $AdvR$ = 4 and 8, the LSB is suppressed by rotation and intense regions of low pressure are visible on the top surface, generating added lift.

Drag was shown to increase at a similar rate as for zero incidence. Pitching moment only suffers a significant growth at $AdvR$ = 8. The L/D ratio was shown to decrease with rotation. The topology of mean limiting streamlines on the top surface shows both the tip vortices and the separation bubble until $AdvR$ = 1. The former disappear at $AdvR$ = 2 and the latter at $AdvR$ = 4. On the bottom surface, the streamlines and C_f contours were seen to be equal to that of zero incidence, despite the change in C_p contours. Differential rotation $AdvR$ = (8,0) increased aerodynamic performance over $AdvR$ = (8,8), namely C_L and L/D, the latter being only slightly smaller than for $AdvR$ = 0. Case $AdvR$ = (8,-8) resulted in a considerable decrease of rolling moment, thus potentially stabilizing the disc's flight;

- **From chapter 7**, aerodynamic coefficients from $AdvR$ = 0 for the entire range of tested α were validated by results from Torres and Mueller [18] and Kamaruddin [19], showing excellent agreement. The separation bubble increased in size and envelops a second, smaller bubble. Differential rotation case $AdvR$ = (8,0) was shown to suppress both these LSBs and again generate high amounts of lift. Once again the L/D ratio was only slightly worsened due to the inclusion of rotation.

In conclusion, a deeper understanding of the physics governing the flight of a rotating disc at low α and at Re for typical fixed-wing MAV operation was gained. Aerodynamic data and topologies of limiting streamlines for high values of $AdvR$, otherwise missing from previous studies, were obtained. These results will undoubtedly prove valuable for possible applications of rotating discs in MAVs, either to control flow separations, improve lift capabilities, reduce drag forces and moments as to stabilize the disc's flight, develop optimal rotation configurations for specific mission and objectives and overall contribute to the amounted knowledge of this field.

8.2 Future Work

The present study should pave the way for future endeavours regarding flying, rotating discs. Some suggestions for subsequent investigations are:

- Observe the impact of changing Re on tested cases;
- Extend the range of applied $AdvR$ to even higher values;
- Include more intermediate $AdvR$ within the selected range;
- Extend the range of applied α;
- Include disc thickness to study gyroscopic phenomenons;
- Conduct a parametric study of the disc's cross-section geometry;
- Further investigate the separation line on the disc and its evolution;
- Analyze additional combinations of differential rotation;
- Experimentally recreate the simulations of this study, as to ascertain their results.

Bibliography

[1] AS-6V-1. Digital Image. *WINGS PALETTE*. http://wp.scn.ru/en/forum/in_focus/1693-2-1. Online; accessed 27 October 2020.

[2] National Air and Space Museum, Smithsonian Institution. Vought V-173 "Flying Pancake". https://airandspace.si.edu/collection-objects/vought-v-173-flying-pancake/nasm_A19610120000, 1998. Online; accessed 17 October 2020.

[3] Avro Canada VZ-9 Avrocar. Digital Image. *The Avro Arrow*. http://digital.scaa.sk.ca/gallery/arrow/view_image.php?image=76. Online; accessed 26 October 2020.

[4] National Museum of the United States Air Force. Avro Canada VZ-9AV Avrocar. https://www.nationalmuseum.af.mil/Visit/Museum-Exhibits/Fact-Sheets/Display/Article/195801/avro-canada-vz-9av-avrocar/, 2015. Online; accessed 18 October 2020.

[5] Sikorsky Cypher. Digital Image. *Robot News*. https://robotnews.wordpress.com/2006/04/03/the-unmanned-aerial-vehicle-the-cypher/. Online; accessed 28 October 2020.

[6] ADIFO. Digital Image. *FLYER*. https://www.flyer.co.uk/romanias-real-flying-saucer/?cmpredirect. Online; accessed 26 October 2020.

[7] Igor I Sikorsky Historical Archives. Cypher Umanned Aerial Vehicle (UAV). https://www.sikorskyarchives.com/CYPHER.php, 2016. Online; accessed 25 October 2020.

[8] ADIFO. ADIFO All Directions Flying Object. http://www.adifoaircraft.com/, 2019. Online; accessed 25 October 2020.

[9] T. J. Mueller. "Aerodynamic Measurements at Low Reynolds Numbers for Fixed Wing Micro-Air Vehicles". In *Proceedings of the Development and Operation of UAVs for Military and Civial Applications [CD-ROM], NATO RTO-EN-9*, Neuilly-sur-Seine, France, 2000.

[10] M. D. Goel and U. Rawat. "Design and Analysis of Wing Structures of Micro Air Vehicles". *Procedia Engineering*, 173:1602–1610, 2017.

[11] I. M. Al-Qadi and A. M. Al-Bahi. "Micro Aerial Vehicles Design Challenges: State of The Art review". In *SSAS UAV Scientific Meeting and Exhibition*, Jeddah, Saudi Arabia, 2006. Paper SSAS-2006-054.

[12] D. Lee, S. Kawai, T. Nonomura, M. Anyoji, H. Aono, A. Oyama, K. Asai, and K. Fujii. “Mechanisms of surface pressure distribution within a laminar separation bubble at different Reynolds numbers”. *Physics of Fluids*, 27:023602, 2015.

[13] W. B. Roberts. “Calculation of Laminar Separation Bubbles and Their Effect on Airfoil Performance”. *AIAA Journal*, 18, No. 1:79–0285R, 1980.

[14] V. de Brederode. *“Aerodinâmica Incompressível: Fundamentos”*. IST Press, 1^{st} edition, 2014.

[15] E. C. Maskell. “Flow Separation in Three Dimensions”. *Roy. Aircr. Establ. Rep. Aero. 2565*, 1955.

[16] M. Tobak and D. J. Peake. “Topology of Three-Dimensional Separated Flows”. *Annual Review of Fluid Mechanics*, 14:61–85, 1982.

[17] G. Torres and T. Mueller. “Aerodynamic Characteristics of Low Aspect Ratio Wings at Low Reynolds Numbers”. In *Fixed and Flapping Wing Aerodynamics for Micro Air Vehicle Applications*, pages 115–141, 2001.

[18] G. Torres and T. Mueller. *“Aerodynamics of Low Aspect Ratio Wings at Low Reynolds Numbers With Applications to Micro Air Vehicle Design and Optimization”*. PhD thesis, University of Notre Dame, 2002.

[19] N. Kamaruddin. *“Dynamics and Performance of Flying Discs”*. PhD thesis, University of Manchester, 2011.

[20] Y. Nakamura and N. Fukamachi. “Visualization of the flow past a Frisbee”. *Fluid Dynamics Research*, 7 (1):31–35, 1991.

[21] J. R. Potts and W. J. Crowther. “The Flow over a Rotating Disc-Wing”. In *RAeS Aerodynamics Research Conference Proc.*, London, UK, Apr 2000.

[22] J. R. Potts and W. J. Crowther. “Frisbee^{TM} Aerodynamics”. In *AIAA 2002-3150, 20th AIAA Applied Aero. Conf.*, St. Louis, MO, June 2002.

[23] H. Higuchi, Y. Goto, R. Hiramoto, and I. Meisel. “Rotating Flying Disks and Formation of Trailing Vortices”. In *AIAA 2000-4001, 18th AIAA Applied Aero. Conf.*, Denver, CO, Aug 2000.

[24] K. Seo, K. Shimoyama, K. Ohta, Y. Ohgi, and Y. Kimura. “Aerodynamic behavior of a discus”. *Procedia Engineering*, 34:92–97, 2012.

[25] K. Seo, K. Shimoyama, K. Ohta, Y. Ohgi, and Y. Kimura. “Optimization of the size and launch conditions of a discus”. *Procedia Engineering*, 72:756–761, 2014.

[26] R. A. Lukes, J. H. Hart, J. Potts, and S. J. Haake. “A CFD analysis of flow around a disc”. *Procedia Engineering*, 72:685–690, 2014.

[27] J. R. Potts and D. Masters. “Validation of the Aerodynamic Loading on Basic Flying Disc Geometries derived from CFD Simulations”. *Procedia Engineering*, 112:400–405, 2015.

[28] X. Tian, Z. Hu, H. Lu, and J. Yang. “Direct numerical simulations on the flow past an inclined circular disk”. *Journal of Fluids and Structures*, 72:152–168, 2017.

[29] S. Gao, L. Tao, X. Tian, and J. Yang. “Flow around an inclined circular disk”. *Journal of Fluid Mechanics*, 851:687–714, 2018.

[30] A. Rohde. *“A Computational Study of Flow Around a Rotating Disc in Flight”*. PhD thesis, Florida Institute of Technology, 2000.

[31] S. a. d. Wiesche. “LES study of heat transfer augmentation and wake instabilities of a rotating disk in a planar stream of air”. *Heat and Mass Transfer*, 40:271–284, 2004.

[32] S. a. d. Wiesche. “Heat transfer from a rotating disk in a parallel air crossflow”. *International Journal of Thermal Sciences*, 46:745–754, 2007.

[33] H. Khalid Moukhtar. *“Study of the aerodynamics of translating spinning discs in laminar and turbulent flow”*. PhD thesis, University of Khartoum, 2012.

[34] A. I. Rouboa, V. M. Reis, V. R. Mantha, D. A. Marinho, and A. J. Silva. “Analysis of wind velocity and release angle effects on discus throw using computational fluid dynamics”. *Computer Methods in Biomechanics and Biomedical Engineering*, 16 (1):73–80, 2013.

[35] A. Dumitrache, F. Frunzulica, and S. Grigorescu. “Aerodynamic Investigations of a Disc-wing”. *AIP Conference Proceedings*, 1798, 2017.

[36] M. Özkan, P. J. Thomas, A. J. Cooper, and S. J. Garrett. “Comparison of the effects of surface roughness and confinement on rotor-stator cavity flow”. *Engineering applications of computational fluid mechanics*, 11, 1:142–158, 2017.

[37] R. J. Lingwood. “Absolute instability of the boundary layer on a rotating disk”. *Journal of Fluid Mechanics*, 299:17–33, 1995.

[38] J. J. Healy. “Model for unstable global modes in the rotating-disk boundary layer”. *Journal of Fluid Mechanics*, 663:148–159, 2010.

[39] S. Imayama. *“Experimental study of the rotating-disk boundary-layer flow”*. Licentiate’s thesis, KTH Royal Institute of Technology, 2012.

[40] N. Gregory, J. T. Stuart, and W. S. Walker. “On the Stability of Three-Dimensional Boundary Layers with Application to the Flow Due to a Rotating Disk”. *Philosophical Transactions of the Royal Society of London. Series A, Mathematical and Physical Sciences*, 248 (943):155–199, 1955.

[41] L. Manni, T. Nishino, and P. L. Delafin. “Numerical Study of Airfoil Stall Cells Using a Very Wide Computational Domain”. *Computers & Fluids*, 140:260–269, 2016.

[42] Q. Chen, Q. Zhong, M. Qi, and X. Wang. “Comparison of vortex identification criteria for planar velocity fields in wall turbulence”. *Physics of Fluids*, 27:085101, 2015.

[43] H. K. Versteeg and W. Malalasekera. *"An Introduction to Computational Fluid Dynamics"*. Pearson Education, 2^{nd} edition, 2007.

[44] D. C. Wilcox. *"Turbulence Modeling for CFD"*. DCW Industries, 3^{nd} edition, 2006.

[45] F. R. Menter. "Zonal Two Equation k-w Turbulence Models for Aerodynamics Flows". *AIAA*, 2906, 1993.

[46] P. R. Spalart. "Detached-Eddy Simulation". *Annual Review of Fluid Mechanics*, 41:181–202, 2009.

[47] M. L. Shur, P. R. Spalart, M. K. Strelets, and A. K. Travin. "A hybrid RANS-LES approach with delayed-DES and wall-modelled LES capabilities". *International Journal of Heat and Fluid Flow*, 29:1638–1649, 2008.

[48] M. S. Gritskevich, A. V. Garbaruk, J. Schütze, and F. R. Menter. "Development of DDES and IDDES Formulations for the k-w Shear Stress Transport Model". *Flow Turbulence Combust*, 88:431–449, 2012.

[49] S. Kida and H. Miura. "Identification and analysis of vortical structures". *European Journal of Mechanics*, 17:471–488, 1998.

[50] J. C. R. Hunt, A. A. Wray, and P. Moin. "Eddies, Streams, and Convergence Zones in Turbulent Flows". *Center for Turbulence Research CTR-S88*, pages 193–208, 1988.

[51] J. Zhou, R. J. Adrian, S. Balachandar, and T. M. Kendall. "Mechanisms for generating coherent packets of hairpin vortices in a channel flow". *Journal of Fluid Mechanics*, 387:353–396, 1999.

[52] J. Jeong and F. Hussain. "On the identification of a vortex". *Journal of Fluid Mechanics*, 285:69–94, 1995.

Appendix A

Alternative Meshes

It could be argued that the used mesh is unnecessarily fine in regions that predictably won't be that crucial to the overall flow. For instance, incredibly fine cells extend needlessly from the Y = 0 plane all over the domain, granting a high quality resolution at the edges of the outer cylinder. This is futile, since the borders of the domain were purposefully placed far enough from the disc as to achieve still and undisturbed flow there. Another similar situation is the one present at the periphery of the disc. Sadly, this refinement must be reproduced to the upper and lower boundaries of the domain as to keep the mesh structured.

Due to this excessive and redundant computational effort, several alternative meshes were devised.

The most promising one was a typical C-mesh. This configuration would allow better refinement at the wake of the disc, which is undoubtedly one of the most interesting and vital parts of the domain to study, and more intuitive boundary condition placement. Figure A.1 showcases this new mesh.

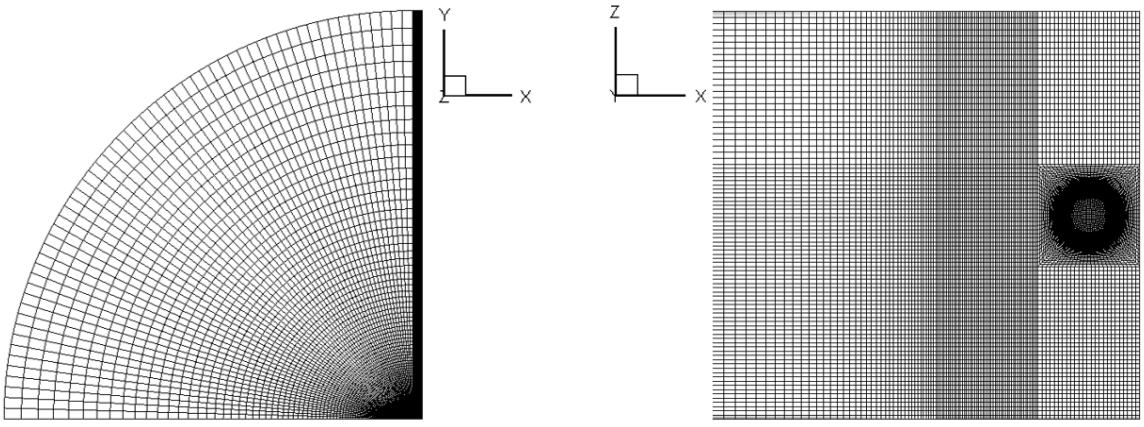

Figure A.1: (a) Side view and (b) bottom view of the C mesh.

Sadly, the disc geometry proved much too hard to place in an ordinary C-mesh and excessive skewed cells surrounded the main regions of interest. Also, unnecessarily fine cells in regions near the edge of the domain also plagued this mesh.

This idea was thus scraped.

The second idea was similar to the original structured mesh. However, an unstructured mesh was incorporated to serve as the region far away from the disc. The surrounding area was kept as structured to offer better refinement but instead of the usual outer cylinder encompassing the disc, a cube was utilized. This was so as to offer better connectivity and control between both types of meshes. The main motivation for this configuration was ending the protruding fine cells at the edges of the domain and having a easier mesh generation far from the disc, where mesh quality is not paramount. A rough representation of this mesh can be seen in Figure A.2.

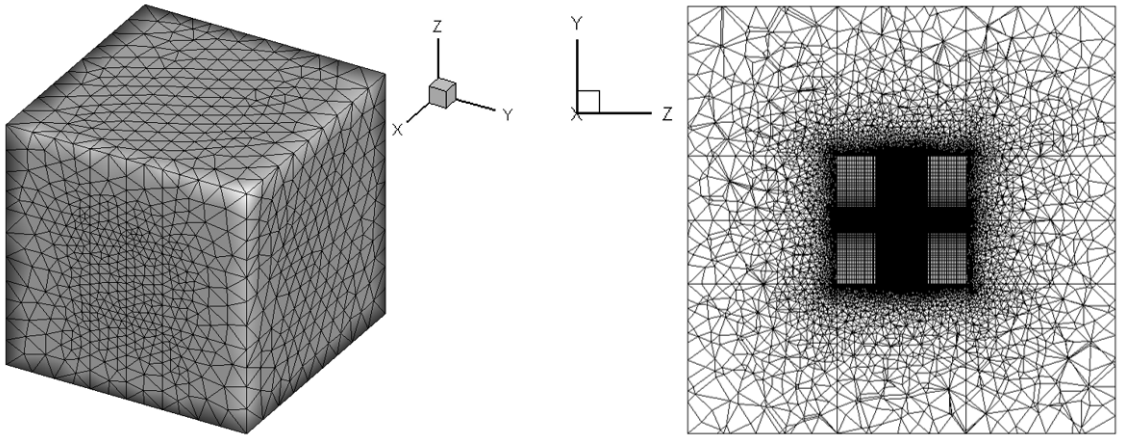

Figure A.2: View of the (a) unstructured mesh and (b) slice by a X = 0 plane.

The interface between structured and unstructured mesh produced incredibly skewed and poor quality cells, which later proved fatal in a basic benchmark problem. Due to these vital regions being poorly resolved, this idea was abandoned.

Appendix B

Turbulence Modelling

After reaching a high enough Reynolds number, all flows become unstable and enter the so-called turbulent regime, which is characterized by a chaotic and random state of motion. It is well established that in this regime, rotational flow structures appear with a wide range of length and time scales known as turbulent eddies [43]. They are responsible for the rapid and effective exchange of mass and momentum and for regions of intense vorticity.

To perfectly capture and reproduce turbulent flow in a simulation, the full range of these eddies has to be solved. The Direct Numerical Simulation (DNS) does exactly that. It requires a sufficiently fine mesh with equally adequate time steps to resolve all the turbulent eddies. As perfect as it may seem, the computational cost associated with this method is utterly excessive for high Reynolds flows, as the number of points in the grid N required for the application of DNS is given by $N \sim Re^{9/4}$ [44].

The two main methods for modeling turbulent flow are RANS and LES. Both introduce models designed to mimic the behaviour of turbulence, thus avoiding the need of solving down to the smallest scale. This grants the user turbulent results (less accurate results, but results nonetheless) without the absurd computational requirements of DNS. A compromise between accuracy and computational effort, omnipresent in CFD, is required for the choice of turbulence model.

Each approach is briefly explained bellow.

B.1 RANS

Today, most turbulent flow computations are obtained through models based on the Reynolds-averaged Navier-Stokes (RANS). Here, these equations are time-averaged and the resulting turbulent fluctuations are described by a closure model. This method is rather attractive due to its low computational cost and because time-averaged properties of the flow are sufficient for most engineering applications.

B.1.1 Shear Stress Transport (SST) $k - w$

This two-equation model developed by Menter [45] is a hybrid model, as in the near wall region the usual $k - w$ model is employed and in the fully turbulent region far from the wall, the $k - \epsilon$ model is used.

This transformation is gradual, made possible by blending functions. As both its constituents, the SST $k-w$ solves two transport equations of turbulence quantities. One is for k, the turbulence kinetic energy, and the other for w, the specific dissipation ratio. The added equations are:

$$\frac{\partial}{\partial t}(\rho k) + \frac{\partial}{\partial x_i}(\rho k u_i) = \frac{\partial}{\partial x_i}\left(\Gamma_k \frac{\partial k}{\partial x_i}\right) + \tilde{G_k} - Y_k + S_k, \tag{B.1}$$

$$\frac{\partial}{\partial t}(\rho w) + \frac{\partial}{\partial x_i}(\rho w u_i) = \frac{\partial}{\partial x_i}\left(\Gamma_w \frac{\partial w}{\partial x_i}\right) + \tilde{G_w} - Y_w + S_w + D_w, \tag{B.2}$$

where the terms Γ_k and Γ_w represent the effective diffusivities given by:

$$\Gamma_k = \mu + \frac{\mu_t}{\sigma_t}, \tag{B.3}$$

$$\Gamma_w = \mu + \frac{\mu_t}{\sigma_w}. \tag{B.4}$$

The turbulence viscosity μ_t is calculated by:

$$\mu_t = \frac{\rho k}{w} \frac{1}{max\left[\frac{1}{\alpha^*}, \frac{SF_2}{\alpha_1 w}\right]}. \tag{B.5}$$

The variable S present in Formula B.5 is the strain rate magnitude. The main purpose of α^* is to limit the eddy viscosity.

$$\alpha^* = \alpha^*_\infty \left(\frac{\alpha^*_0 + Re_t/R_k}{1 + Re_t/R_k}\right). \tag{B.6}$$

Also, σ_t and σ_w are the turbulent Prandtl numbers for k and w, respectively. They can be computed through:

$$\sigma_k = \frac{1}{F_1/\sigma_{k,1} + (1-F_1)/\sigma_{k,2}}, \tag{B.7}$$

$$\sigma_w = \frac{1}{F_1/\sigma_{w,1} + (1-F_1)/\sigma_{w,2}}. \tag{B.8}$$

Alas, F_1 and F_2 are the aforementioned blending functions. Their formulas and subsequent parameters are:

$$F_1 = tanh(\Phi_1^4), \tag{B.9}$$

$$\Phi_1 = min\left[max\left(\frac{\sqrt{k}}{0.09wy}, \frac{500\mu}{\rho y^2 w}\right), \frac{4\rho k}{\sigma_{w,2} D_w^+ y^2}\right], \tag{B.10}$$

$$D_w^+ = max\left[2\rho \frac{1}{\sigma_{w,2}} \frac{1}{w} \frac{\partial k}{\partial x_j} \frac{\partial w}{\partial x_j}, 10^{-10},\right] \tag{B.11}$$

$$F_2 = tanh(\Phi_2^2), \tag{B.12}$$

$$\Phi_2 = max\left[2\frac{\sqrt{k}}{0.09wy}, \frac{500\mu}{\rho y^2 w}\right], \tag{B.13}$$

where y is the distance to the closest surface and D_w^+ is the positive portion of the cross-difusion term.

Some terms of Equations B.1 and B.2 still need to be defined. The variable $\tilde{G_k}$ represents the generation of turbulence kinetic energy due to the mean velocity gradients and is given by:

$$\tilde{G_k} = min(G_k, 10\rho\beta^* kw), \tag{B.14}$$

where:

$$G_k = \mu_t S^2. \tag{B.15}$$

Additionally, G_w is the generation of w obtained by:

$$G_w = \frac{\alpha}{\nu_t}\tilde{G_k}, \tag{B.16}$$

for α:

$$\alpha = \frac{\alpha_\infty}{\alpha^*}\left(\frac{\alpha_0 + Re_t/R_w}{1 + Re_t/R_w}\right). \tag{B.17}$$

The term R_w is a constant, Re_t is obtained through:

$$Re_t = \frac{\rho k}{\mu w}, \tag{B.18}$$

and α^* through the Formula B.6. The term α_∞ present in the Formula B.17 is given by:

$$\alpha_\infty = F_1\alpha_{\infty,1} + (1 - F_1)\alpha_{\infty,2}, \tag{B.19}$$

$$\alpha_{\infty,1} = \frac{\beta_{i,1}}{\beta_\infty^*} - \frac{\kappa^2}{\sigma_{w,1}\sqrt{\beta_\infty^*}}, \tag{B.20}$$

$$\alpha_{\infty,2} = \frac{\beta_{i,2}}{\beta_\infty^*} - \frac{\kappa^2}{\sigma_{w,2}\sqrt{\beta_\infty^*}}. \tag{B.21}$$

Also present in B.1 and B.2 are the dissipation terms:

$$Y_k = \rho\beta^* kw, \tag{B.22}$$

$$Y_w = \rho\beta w^2, \tag{B.23}$$

where:

$$\beta^* = \beta^*_\infty \left(\frac{4/15 + (Re_t/R_\beta)^4}{1 + (Re_t/R_\beta)^4} \right). \tag{B.24}$$

Finally the cross diffusion term D_w is:

$$D_w = 2(1 - F_1)\rho\sigma_{w,2} \frac{1}{w} \frac{\partial k}{\partial x_k} \frac{\partial w}{\partial x_j}. \tag{B.25}$$

With special regards to the software used, $FLUENT$, the value of w at the wall is given by:

$$w_w = \frac{\rho(u^*)^2}{\mu} w^+. \tag{B.26}$$

In the viscous sub-layer:

$$w^+ = min \left(w^+_w, \frac{60}{\beta_i (y^+)^2} \right), \tag{B.27}$$

and:

$$w^+_w = \begin{cases} \left(\frac{50}{k^+_s} \right)^2, & k^2_s < 25 \\ \frac{100}{k^+_s}, & k^2_s \geq 25 \end{cases}, \tag{B.28}$$

$$k^+_s = max \left(1, \frac{\rho k_s u^*}{\mu} \right), \tag{B.29}$$

where k_s is the roughness height. For the logarithmic region:

$$w_+ = \frac{1}{\sqrt{\beta^*_\infty}} \frac{du^+_{turb}}{dy^+}, \tag{B.30}$$

which leads to the value of w as:

$$w = \frac{u^*}{\sqrt{\beta^*_\infty} \kappa y}. \tag{B.31}$$

B.2 LES

The Large Eddy Simulation (LES) method operates differently than RANS. Instead of time averaging the Navier-Stokes equations, spatial filtering is carried out as to distinguish the large from the small scale eddies. The former are fully computed while information regarding the latter is filtered. The smaller eddies are then modeled through what is called a sub-grid scale model. This division stemmed from the premise that the larger eddies have a higher impact on the overall flow and therefore must be resolved. Contrarily, the smaller eddies are weaker and more universal, and can thus be modeled [44].

Results obtained from LES increase in accuracy, when compared to those obtained from RANS. However, the price to pay for this improvement is a much higher computational cost.

B.2.1 Spatial Filtering

The spatial filtering operation is defined by means of a filter function G as:

$$\bar{\phi}(x,t) = \int_{-\infty}^{\infty}\int_{-\infty}^{\infty}\int_{-\infty}^{\infty} G(x,x',\Delta)\phi(x',t)\,dx'_1 dx'_2 dx'_3, \tag{B.32}$$

where $\bar{\phi}(x,t)$ is the filtered function, $\phi(x,t)$ is the unfiltered function and Δ is the cutoff width. This last variable determines what is kept and what is filtered.

There are several different formulations of the filtering function used to separate the scale of the eddies into resolved and modeled. The most common are the Gaussian filter:

$$G(x,x',\Delta) = \left(\frac{6}{\pi\Delta^2}\right)^{3/2} exp\left(-6\frac{|x-x'|^2}{\Delta^2}\right), \tag{B.33}$$

the spectral cutoff:

$$G(x,x',\Delta) = \prod_{i=1}^{3}\frac{sin[(x_i - x'_i)/\Delta]}{(x_i - x'_i)}, \tag{B.34}$$

and the top-hat or box filter:

$$G(x,x',\Delta) = \begin{cases} 1/\Delta^3, & |x-x'| \leq \Delta/2 \\ 0, & |x-x'| > \Delta/2 \end{cases}. \tag{B.35}$$

Filters B.33 and B.34 are mostly used in research literature but for finite volume implementation of LES, B.35 is utilized [43]. For $FLUENT$ and most commercial CFD codes, Δ is chosen as to be the grid size.

$$\Delta = \sqrt[3]{\Delta x \Delta y \Delta z}. \tag{B.36}$$

B.2.2 Filtered Unsteady Navier-Stokes Equations

By applying the filtered operation to the Navier-Stokes equations results:

$$\frac{\partial \rho}{\partial t} + \frac{\partial}{\partial x_i}(\rho \bar{u_i}) = 0, \tag{B.37}$$

$$\frac{\partial}{\partial t}(\rho \bar{u_i}) + \frac{\partial}{\partial x_j}(\rho \bar{u_i}\bar{u_j}) = \frac{\partial}{\partial x_j}\left(\mu\frac{\partial \sigma_{ij}}{\partial x_j}\right) - \frac{\partial \bar{p}}{\partial x_i} - \frac{\partial \tau_{ij}}{\partial x_{ij}}, \tag{B.38}$$

with:

$$\sigma_{ij} \equiv \left[\mu\left(\frac{\partial \bar{u_i}}{\partial x_j} + \frac{\bar{u_j}}{\partial x_i}\right)\right] - \frac{2}{3}\mu\frac{\partial \bar{u_l}}{\partial x_l}\delta_{ij}, \tag{B.39}$$

and τ_{ij} represents the sub-grid-scale stresses (SGS).

$$\tau_{ij} \equiv \overline{\rho u_i u_j} - \rho \bar{u}_i \bar{u}_j. \tag{B.40}$$

This last term can be further developed by decomposing a flow variable ($\phi(x,t)$) into the filtered function ($\phi(\bar{x},t)$), which is fully computed by LES, and the unresolved spatial variations ($\phi(x,t)'$), which were cut off by the filter, as such:

$$\phi(x,t) = \phi(\bar{x},t) + \phi(x,t)'. \tag{B.41}$$

After introducing modification B.41 into Equation B.40 and developing its terms, results as follows:

$$\tau_{ij} = (\overline{\rho \bar{u}_i \bar{u}_j} - \rho \bar{u}_i \bar{u}_j) + \overline{\rho \bar{u}_i u_j'} + \overline{\rho u_i' \bar{u}_j} + \overline{\rho u_i' u_j'}. \tag{B.42}$$

Three different groups can readily be seen. Firstly, the Leonard stress L_{ij} given by:

$$L_{ij} = \overline{\rho \bar{u}_i \bar{u}_j} - \rho \bar{u}_i \bar{u}_j, \tag{B.43}$$

which merely account for effects of the resolved scale, as only filtered components are present. Then the Cross-stresses C_{ij}:

$$C_{ij} = \overline{\rho \bar{u}_i u_j'} + \overline{\rho u_i' \bar{u}_j}. \tag{B.44}$$

As the name implies, they are due to the interaction between resolved and unresolved scales. The final term of B.42 is called LES Reynolds stresses R_{ij}, given by:

$$R_{ij} = \overline{\rho u_i' u_j'}. \tag{B.45}$$

They are the result of the interactions of the SGS eddies.

B.2.3 Smagorinksy-Lilly SGS Model

For finite volume applications, all the contributions of the SGS stresses listed above are modelled as a single entity τ_{ij}, despite the clearly different natures of each component.

Smagorinksy developed the first model for the SGS stresses. It simply postulated that the SGS stresses are proportional to the local rate of strain of the resolved flow $\bar{S_{ij}}$ as in:

$$\tau_{ij} - \frac{1}{3}\tau_{kk}\delta_{ij} = -2\mu_t \bar{S_{ij}}, \tag{B.46}$$

with:

$$\bar{S_{ij}} \equiv \frac{1}{2}\left(\frac{\partial \bar{u}_i}{\partial x_j} + \frac{\partial \bar{u}_j}{\partial x_i}\right), \tag{B.47}$$

The term τ_{kk} in Equation B.46 can be neglected or added to the filtered pressure term for incompressible flows. The variable μ_t is the eddy viscosity and is obtained by:

$$\mu_t = \rho L_s^2 \sqrt{2\bar{S_{ij}}\bar{S_{ij}}}, \tag{B.48}$$

$$L_s = min(\kappa d, C_s \Delta), \tag{B.49}$$

where κ is the von Kármán constant, d is the distance to the closest wall and C_s is the Smagorinksy constant.

B.3 DES

The Detached Eddy Simulation model (DES) aims at combining both LES and unsteady RANS. The core turbulent region is solely computed by the former, while boundary layers and shear layers are treated through the latter, leading to a more intermediate computational cost. It seeks to combine the best of the two models, as RANS fails to predict large separation regions and LES would be prohibitively expensive, in terms of computational effort, to apply everywhere in the domain [46].

Whether LES or RANS is applied depends entirely on the length scale given:

$$l_{DES} = min(l_{RANS}, l_{les}) = min(l_{RANS}, C_{des}\Delta), \tag{B.50}$$

where C_{des}, is a constant and Δ is obtained through:

$$\Delta = max(\Delta_x, \Delta_y, \Delta_z). \tag{B.51}$$

B.3.1 SST $k-w$ Based DES

The term Y_k given by Formula B.22 undergoes a slight change:

$$Y_k = \rho \beta^* k w F_{DES}, \tag{B.52}$$

$$F_{DES} = max\left(\frac{L_t}{C_{des}\Delta}, 1\right), \tag{B.53}$$

$$L_t = \frac{\sqrt{k}}{\beta^* w}. \tag{B.54}$$

B.3.2 IDDES

This coupling between RANS and LES leads to mismatches, namely on the logarithmic layer, which lead to a under-prediction of the skin friction of 15-20% [47]. This, and the desire to create a more robust

DES formulation, brought forth the Improved Delayed Detached Eddy Simulation (IDDES). This method combines a RANS model (SST $k-w$) and LES. The length scale of IDDES is as follows from [48]:

$$l_{IDDES} = \tilde{f}_d(1+f_e)l_{RANS} + (1-\tilde{f}_d)l_{LES}. \tag{B.55}$$

The LES length scale is defined as:

$$\Delta = min(C_w max(d_w, h_{max}), h_{max}). \tag{B.56}$$

Also, the empiric blending function $\tilde{f}_d$ present in Formula B.55 is given by:

$$\tilde{f}_d = max((1-f_{dt}), f_b), \tag{B.57}$$

$$f_{dt} = 1 - tanh\left[(C_{dt1}r_{dt})^{C_{dt}}\right], \tag{B.58}$$

$$r_{dt} = \frac{\nu_t}{\kappa^2 d_w^2 \sqrt{0.5(S^2+\Omega^2)}}, \tag{B.59}$$

$$\tilde{f}_b = min(2exp(-9\alpha^2), 1). \tag{B.60}$$

The other blending coefficient f_e is obtained by:

$$f_e = f_{e2} max((f_{e1}-1), 0), \tag{B.61}$$

$$f_{e1} = \begin{cases} 2exp(-11.09\alpha^2), & \alpha \geq 0 \\ 2exp(-9.0\alpha^2), & \alpha < 0 \end{cases}, \tag{B.62}$$

$$f_{e2} = 1 - max(f_t, f_l), \tag{B.63}$$

$$f_t = tanh\left((C_t^2 r_{dt})^3\right), \tag{B.64}$$

$$f_l = tanh\left((C_l^2 r_{dl})^{10}\right), \tag{B.65}$$

$$r_{dl} = \frac{\nu}{\kappa^2 d_w^2 \sqrt{0.5(S^2+\Omega^2)}}. \tag{B.66}$$

Appendix C

Methods for Vortex Identification

The appearance of vortical structures is undoubtedly expected, either from an increase in angle of attack or from the interaction between the incoming flow and the rotation of the disc. An adequate analysis of these structures grants a deeper understanding of the problem at hand and serves as an excellent comparison between cases with changing parameters. As such, reliable methods to properly visualize these occurrences have to be considered.

C.1 Vorticity

The most common way to observe vortical structures is through surfaces of constant vorticity $\overrightarrow{\omega}$, given by:

$$\overrightarrow{\omega} = \nabla \times \overrightarrow{U}. \tag{C.1}$$

As appealing as this simple method may seem, vorticity alone can not distinguish between swirling and shearing motions [49]. Thus, regions of high vorticity, as in shear and boundary layers, which theoretically are uncorrelated to the presence of the vortices, appear alongside and may even obscure them.

Another issue is the apparent random threshold for the isosurfaces of vorticity. With no clear guidance for the choice of this value, different geometrical characteristics of the isosurfaces are obtained through different thresholds. So, a clear and concise representation of vortical structures is not achieved.

As such, more robust methods, which cover these weaknesses, were created.

C.2 The Q Criterion

This next method starts from the velocity gradient tensor (W_{ij}) given by:

$$W_{ij} = \frac{\partial U_i}{\partial x_j}. \tag{C.2}$$

The characteristic equation of the velocity gradient tensor, which allows the calculation of its eigenvalues λ is:

$$\lambda^3 + P\lambda^2 + Q\lambda + R = 0, \tag{C.3}$$

where P, Q and R are known as the invariants of W_{ij}.

According to Hunt et al. [50], vortices can be defined by regions with positive second invariant Q and pressure lower that ambient pressure. This last condition is to ensure that the streamlines of this region are curved.

Mathematically, this results in:

$$Q > 0 \Rightarrow Q \equiv \frac{1}{2}\left(||\omega||^2 - ||S||^2\right) > 0, \tag{C.4}$$

which translates to regions where the vorticity is stronger than the strain-rate, in terms of magnitude.

This is a vast improvement over the pure vorticity method, as a guideline for a threshold is introduced and the pressure is now a decisive factor.

C.3 Swirl Strength

The swirl strength criterion analyses the eigenvalues for the velocity gradient tensor and was first proposed by Zhou et al. [51]. Usually in 3D flow, the velocity gradient tensor exhibits 3 eigenvalues, real and complex.

$$\lambda_1 = \lambda_R \in \mathbb{R},$$

$$\lambda_{2,3} = \lambda_{cr} \pm \lambda_{ci} \in \mathbb{C}.$$

The variable λ_{ci} quantifies the strength of the swirling motion, thus providing a method for visualizing vortex structures. As opposed to the Q criterion method however, a standard threshold is not present here. A positive value, usually a small percentage of its maximum value was shown to provide smooth results.

C.4 The λ_2 Criterion

This criterion proposed by Jeong and Hussain [52] aimed at improving the previous methods by focusing on finding a pressure minimum across the suspected vortex. One takes the gradient of the Navier-Stokes equations and decomposes them into symmetric and assymetric parts. The former becomes the vorticity transport equation:

$$\frac{DS_{ij}}{Dt} - \nu S_{ij,kk} + \omega_{ik}\omega_{kj} + S_{ik}S_{kj} = -\frac{1}{\rho}p_{ij}, \tag{C.5}$$

where p_{ij} is the Hessian of pressure, which contains information about local pressure extrema.

The first two terms in Equation C.5 are dropped to avoid known mismatches between pressure minimums and vortex cores. The first term represents unsteady irrotational straining, which may lead to the existence of a pressure minimum in the absence of any vortical motion, and the second term translates viscous effects, which can eliminate a pressure minimum amidst a vortical motion [52]. By neglecting these two terms, this model hopefully becomes more reliable and accurate at identifying vortical structures.

As is known, for the pressure to have a local minimum, p_{ij} must have two positive eigenvalues. Only $S^2+\omega^2$ are now taken into account to determine the existence of a local pressure minimum due to vortical motion and by definition, a vortex core is present when two eigenvalues of $S^2 + \omega^2$ are negative. Since $S^2 + \omega^2$ is symmetric, it has real eigenvalues. So, for eigenvalues $\lambda_1, \lambda_2, \lambda_3$ ordered by $\lambda_1 \geq \lambda_2 \geq \lambda_3$, the criterion for the presence of a vortex core is $\lambda_2 < 0$.